Experimental Investigation of a Coaxial Gyrotron Oscillator

by

Rahul N. Advani

BS, Electrical Engineering (1993)
Cornell University

Submitted to the Department of Nuclear Engineering
in Partial Fulfillment of the Requirements for the degree of
Doctor of Philosophy in Nuclear Engineering
at the
Massachusetts Institute of Technology
July 1999
[September 1999]

Science

Signature of Author ....
Department of Nuclear Engineering
July 9, 1999

Certified by ....
Richard Temkin
Senior Research Scientist, Department of Physics
Thesis Supervisor

Accepted by ....
Ian Hutchinson
Professor, Department of Nuclear Engineering
Thesis Reader

Accepted by ....
Sow-Hsin Chen
Chairman, Department Committee on Graduate Students

Experimental Investigation of a Coaxial Gyrotron Oscillator

By

Rahul N. Advani

Submitted to the Department of Nuclear Engineering
On July 9, 1999, in partial fulfillment of the
Requirements for the degree of
Doctor of Philosophy

Abstract

This thesis presents experimental results of a megawatt power level, 140 GHz coaxial gyrotron oscillator. The coaxial gyrotron has the potential to transport very high power electron beams and thus achieve higher microwave output power levels than conventional gyrotrons. A $TE_{21,13}$ coaxial gyrotron was designed to operate at 95 kV, 76 A. This tube was tested to high power with the first high power Inverted Magnetron Injection Gun (IMIG). The IMIG electron gun was tested to 10 MW (105 kV, 93 A), which is the highest power level for a non-relativistic gyrotron gun. Operation of the coaxial gyrotron oscillator yielded power levels of greater than 1 MW in two different configurations: with the coaxial conductor (at 92kV, 70 A, and 16% efficiency) and without the coaxial conductor (85 kV,65 A, and 18% efficiency). We also successfully operated this tube in three configurations (empty cavity, radial output, and axial output) with no beam interception. We observed regimes of dominant single mode and multi-mode operation. We also identified electron beam asymmetries and tube alignment as two major issues, which can limit the performance of a coaxial gyrotron. An unexpected source of magnetic field error was found in the magnetization of the stainless steel parts. All these results have led to techniques for improving not only coaxial gyrotrons but also other gyrotron tubes.

We also investigated a ferroelectric cathode, which has the potential to achieve higher currents than thermionic cathodes in a simpler, low cost gun. We report the first results on a ferroelectric cathode gun in a magnetron injection gun configuration suitable for use in a gyrotron. It had an annular emitter shape with a diameter of 11.4 cm and a width of 0.25 cm and operated at currents of up to 10 A (1.1 A/cm^2) at 8 kV, in 5 μs flat-top pulses. This result (along with the kiloampere beam obtained at Integrated Applied Physics) demonstrate the scalability of ferroelectric cathodes to large diameter electron beams. Also, the first ever microwaves from a ferroelectric cathode were generated in a collaboration experiment at Tel Aviv University. Finally, we developed a theory to explain the emission process from ferroelectric cathodes. The experiments reported have shown the suitability of ferroelectric cathodes for future microwave generation experiments.

Acknowledgments

Six years of work (and play) at MIT led to this point of the writing of this thesis. This entire period was one of the most critical in my life and could not have been completed without the help of several people.

First of all, I thank Richard Temkin without whose help, support, and patience it would have been impossible for me to have this wonderful and productive career at MIT. Ivan Mastovsky, George Yarworth, and Bill Mulligan whose day-to-day support was really critical in completing the experiments on schedule. Ken Kreischer, especially for his help during the design phases of the experiments. I would also like to thank Prof. Ian Hutchinson for his kind guidance and moral support. In addition, I thank Marco Pedrozzi, Jagadishwar Rao Sirigiri (my friend) and J.P. Hogge. I would also like to thank Kip Bishofberger, Doug Denison, and Michael Shapiro for their help. My sincere gratitude goes to Prof. Ed Roberts at the Sloan School of Management for his guidance and help in shaping my career in the management arena.

For their collaboration and help with the ferroelectric theory and experiments, I would like to thank G. Rosenman and D. Shur at Tel-Aviv University. Their valuable collaboration and many comments helped improve my understanding of the emission process of ferroelectrics. The help of M. Einat and Eli Jerby is greatly appreciated in the ferroelectric microwave generation experiments.

Finally, I would like to thank my family and friends for all the support and encouragement through the entire period of my Ph.D. I would like to thank my father, my mother, my brother, my bhabhi, Aditi, J. Yap, K. Joshi and all the other people whose love and support will never be forgotten. I dedicate this thesis to my grandfather, J.S. Advani.

Contents

1. Introduction **15**

1.1 Overview 15

1.2 Electron beams in Gyrotrons 17

1.2.1 Coaxial Gyrotrons 18

1.2.2 Ferroelectric Cathodes 20

1.3 Thesis Layout 22

2. Electron guns for Gyrotrons **23**

2.1 Introduction 23

2.2 Magnetron Injection Guns 25

2.2.1 General electron motion equations 25

2.2.2 Adiabatic theory 29

2.2.3 Self consistent theory 32

2.3 Cavity and Beam tunnel 34

2.3.1 Voltage depression and limiting current 34

2.3.2 Velocity spread 36

2.3.3 Energy spread 38

2.3.4 Velocity ratio measurement 39

2.3.5 Rotating probe measurement of current 41

2.3.6 Witness plate measurement 43

2.3.7 Temperature measurement 44

3. Ferroelectric Cathodes **47**

3.1 Introduction 47

3.2 Large area Ferroelectric cathode experiments 49

3.2.1 Planar beam experiment 49

3.2.2 Annular beam experiment 54

3.3 Microwave generation from ferroelectrics 60

3.4 Ferroelectric cathode emission characteristics 63

3.4.1 Initial energy effect 64

3.4.2 Surface plasma effect 68

3.4.3 Discussion of ferroelectric emission process 70

3.4.4 Effects explained by proposed emission process 77

4. Coaxial Gyrotron Design **79**

4.1 Introduction 79

4.2 Gyrotron cavity 82

4.2.1 Cavity mode 83

4.2.2 Mode competition 87

4.2.3 Multimode code simulations 92

4.3 Electron gun design 96

4.3.1 Detailed EGUN simulations 101

4.4 Mode Converter 107

4.5 Experimental runs 110

5. Coaxial Gyrotron Experiments **113**

5.1 Introduction 113

5.2 Coaxial conductor and mode converter mode 114

5.3 Empty cavity mode (without coaxial conductor) 118

5.4 Electron beam – azimuthal symmetry analysis 127

5.4.1 First cathode: Electron beam azimuthal symmetry analysis 127

5.4.2 Second cathode: Electron beam azimuthal symmetry analysis 135

5.5 Coaxial conductor with axial output mode 138
    5.5.1 Effects of beam asymmetry on tube performance 144

6. Conclusions and suggestions for future work **149**
6.1 Introduction 149
6.2 Ferroelectric cathode 149
6.3 Coaxial Gyrotron 153
6.4 Conclusions 156

7. Bibliography **157**

List of Figures

1.1 Frequency and power of various sources **17**

1.2 Schematic of (a) regular gyrotron oscillator in a *whispering gallery mode*, and (b) coaxial gyrotron in a *body mode* **19**

2.1 Schematic of a (a) Magnetron injection gun – MIG with the cathode on the inside of the anode; and a (b) Inverted Magnetron injection gun – IMIG. Both the guns shown are diode guns **24**

2.2 Schematic of IMIG gun with (a) the field profile, (b) general parameters and major components of a coaxial gyrotron oscillator, and (c) expanded view of cathode region **26**

2.3 Schematic of rotating probe used to investigate the azimuthal symmetry of electron beam **42**

2.4 Schematic of temperature measuring apparatus used to investigate the azimuthal symmetry of the cathode emitter temperature **44**

3.1 Schematic of the planar ferroelectric cathode gun at IAP with a diameter of 10.2 cm and a anode-cathode gap of 4 cm **50**

3.2 Pulse applied across the IAP planar ferroelectric cathode to excite emission- V_{fe}(solid line), I_{fe}(dashed line) **52**

3.3 Accelerating potential (~30 kV) and emitted current (~1000 A) for the planar ferroelectric gun. This pulse follows that in Fig 3.2 by 6 μs **52**

3.4 Beam current versus delay between the pulse applied across the ferroelectric and the accelerating pulse across the anode-cathode (V_{ak} = 50 kV) **53**

3.5 V-I characteristics of the planar ferroelectric gun. Impedance ~200 • **54**

3.6 EGUN design of the annular ferroelectric gun at MIT. Velocity spread (at the cavity injection point) is 6.9 %, and the alpha is 1.6 **56**

3.7 Mechanical setup used to test the annular ferroelectric gun **56**

3.8 (a) Pulse applied across the MIT annular ferroelectric cathode to excite emission - V_{fe}, I_{fe} ; (b) Emitted current reaching the anode and acceleration voltage - I_{ak}, V_{ak} (bottom) **57**

3.9 V-I characteristics of the annular ferroelectric gun at MIT. The diode impedance can be estimated as 600-800 • **59**

3.10 Schematic of experimental setup for ferroelectric microwave experiment **60**

3.11 Collector current (generated from the ferroelectric cathode) **61**

3.12 Typical RF output trace measured **62**

3.13 RF output power vs. frequency **62**

3.14 Schematic of the experimental setup used to measure the ferroelectric electron beam initial energy distribution **66**

3.15 Measured electron energy spectrum from the ferroelectric cathode. Maximum trigger voltage applied was ~ 1800 V **66**

3.16 Emission process with surface plasma and energetic electrons **68**

3.17 Experimental, Child-Langmuir, and theoretical V-I curves for IAP results (Theory curve are fitted to the modified initial energy equations, with an average energy of 2.25 keV) **72**

3.18 Minimum delay of emitted current vs. (i) risetime of pulse applied across the ferroelectric cathode, and (ii) radius of various cathodes **74**

4.1 Schematic of the 3MW, 140 GHz gyrotron operated at MIT **81**
1. Cathode, 2. Anodes, 3. Coaxial Conductor, 4.Cavity, 5. Collector
6. Window, 7. Superconducting Magnet, 8. Gun coils, 9. Valve

4.2 Schematic of the cavity section of the coaxial gyrotron **82**

4.3 Output power vs. waveguide indices at fixed average ohmic wall loading **84**

4.4 Cavity and the RF field profile in the $TE_{21,13}$ mode **84**

4.5 Coupling for the $TE_{21,13}$ mode as a function of beam radius **86**

4.6 Competing modes near the $TE_{21,13}$ mode **86**

4.7 Electronic efficiency versus beam current for the $TE_{21,13}$ mode **87**

4.8 Mode roots vs. the inner conductor radius for competing modes in a $TE_{21,13}$ cavity. Roots are normalized to $TE_{21,13}$ mode without an inner conductor **88**

4.9 Ohmic heating of the inner and outer conductor versus the inner conductor radius – calculated with 1.5 times the conductivity of OFHC copper at 300°C **89**

4.10 Diffractive Q's as a function of radial mode index and azimuthal mode for the case of a 1° taper of the inner coaxial conductor **90**

4.11 Starting current as a function of beam voltage for the case with no inner conductor. The beam load line is also shown **91**

4.12 Starting current as a function of beam voltage for the case of a 6.02 mm uniform inner conductor (the line is an approx. of the non-linear excitation region) **91**

4.13 Multimode simulations for the case without the inner conductor. The $TE_{21,13}$ mode could not be obtained **93**

4.14 (a) Multimode simulations for the case with an inner conductor - uniform 6.02 mm radius inner conductor, (b) Multimode simulations for the case with an inner conductor - 1° tapered inner conductor **94**

4.15 Beam trajectories and magnetic field for design EGUN simulation **98**

4.16 Alpha and perp. velocity spread versus beam current (V = 95 kV = const.) **99**

4.17 Alpha and perp. velocity spread versus beam voltage (I = 88 A = const.) **99**

4.18 Mechanical drawing of the inverted MIG electron gun used for the coaxial gyrotron experiment **100**

4.19 Beam trajectories and magnetic field for a design EGUN simulation **101**

4.20 Velocity ratio (alpha), parallel and perpendicular velocity spread versus beam voltage **102**

4.21 Velocity ratio (alpha), parallel and perpendicular velocity spread versus beam current **103**

4.22 Velocity ratio (alpha), parallel and perpendicular velocity spread versus displacement of inner conductor in the axial direction **104**

4.23 Velocity ratio (alpha), parallel and perpendicular velocity spread versus misalignment of inner conductor in the radial direction **105**

4.24 Velocity ratio (alpha), parallel and perpendicular velocity spread versus current in the absolute coil (the center one of the gun coils) **106**

4.25 Mode composition versus axis in the pre-buncher. The input mode and the four most significant satellite modes shown (15 smaller modes are not shown) **108**

4.26 Mechanical (AutoCAD) drawing of the gyrotron with the mode converter and radial power output. Note the plunger arrangement on the collector (right) end, which helped us introduce the coaxial conductor without breaking vacuum **109**

4.27 Schematic of initial runs with a mode converter and one mirror. Power was extracted radially from the quartz window. **110**

4.28 Schematic of runs with axial power extraction from the quartz window **111**

4.29 Schematic of the empty cavity runs with axial power extraction from the quartz window **112**

5.1 Schematic of initial runs with a mode converter and one mirror. Power was extracted radially from the quartz window (cathode 1) **114**

5.2 Output power and frequency (modes) versus the main magnetic field. The operating parameters were 92 kV, 70 Amps, giving an efficiency of operation of ~14 % for a maximum power output of ~ 1 MW (cathode 1) **115**

5.3 Output power and efficiency vs. beam current, V ~ 95 kV (cathode 1) **116**

5.4 Output power and efficiency versus main field (cathode 1) **117**

5.5 Schematic of the empty cavity mode of operation. The coax conductor has been removed, and power is extracted radially **118**

5.6 Power and frequency versus main magnetic field in empty cavity mode. The design mode shown above is the $TE_{21,13}$ mode at 139.95 GHz (cathode 1) **119**

5.7 (a) Experimentally obtained modes and theoretically expected modes in the empty cavity mode of operation; (b) Experimentally obtained modes and theoretically expected modes in the empty cavity mode of operation (cathode 1) **120**

5.8 Power and frequency with respect to the main magnetic field with the new cathode in the empty cavity mode. Shaded dots are the dominant modes and the hollow dots are weak modes. V=85 kV, I = 65 A, $\alpha = 1.43$ for entire scan (cathode 2) **122**

5.9 Current and power versus voltage during empty cavity operation. The starting current curve for the $TE_{21,13}$ mode is shown in bold (U-shaped curve) while the dots are actually the experimentally measured modes (cathode 2) **123**

5.10 Power and frequency observed from the tube as a function of alpha. The alpha was raised using the absolute gun coil. The design mode $TE_{21,13}$ is dominant over a large range, which is the reason that this set of data was chosen (cathode 2) **124**

5.11 Theoretical (EGUN simulations) and experimental values of velocity ratio (alpha) versus changes in the cathode magnetic field. The cathode magnetic field was varied using the absolute gun coils (cathode 1) **125**

5.12 Theoretical (EGUN simulations) and experimental values of velocity ratio (alpha) versus beam voltage (cathode 1) **126**

5.13 Beam width measured versus azimuthal angle. 0° in all our measurements is where the heater lead enters the cathode housing (cathode 1) **128**

5.14 Scan of an electronic microscope image of the witness plate used for the electron beam asymmetry measurement (cathode 1) **129**

5.15 Normalized beam current vs. azimuthal angle. Beam current at any angle is normalized to the average total current - sector + collector (cathode 1) **131**

5.16 Temperature versus azimuthal angle for four different power levels. The temperature was measured with an optical pyrometer whose range was 750 - 1300°C (cathode 1) **132**

5.17 Calculated emission density versus azimuthal angle. The emission density was gleaned from the manufacturer's published data on emission density vs. temperature for this cathode (cathode 1) **133**

5.18 Comparison of emission density versus azimuthal angle for two different techniques. The temperature measurements are shown by the solid squares while the hollow dots show the rotating probe measurements (cathode 1) **134**

5.19 Normalized current on rotating probe versus azimuthal angle for the second cathode. Data for 3 different accelerating voltages shown (cathode 1) **135**

5.20 Normalized current on rotating probe versus azimuthal angle for the second cathode. Data for four different heater levels (cathode 2) **136**

5.21 Variation of the current for the second cathode versus voltage for four different heater levels (cathode 2) **137**

5.22 Schematic of runs with the coaxial conductor inserted and axial power extraction from the quartz window **139**

5.23 Output power (curve) and frequency/modes (points) versus the main magnetic field in the axial output mode with coaxial conductor (cathode 1) **140**

5.24 Output power and modes versus beam voltage in the axial mode of operation with the coaxial conductor (cathode 1) **141**

5.25 Dominant modes, their theoretical starting currents, and beam current vs. voltage (cathode 1) **142**

5.26 Scan of power and frequencies/modes vs. alpha -axial output with coax conductor (cathode 1) **142**

5.27 Mode map of the various modes obtained during operation in the axial output configuration with the coaxial conductor inserted (cathode 1) **143**

5.28 Simulated values (EGUN) of perpendicular and parallel velocity spread versus beam current **145**

5.29 Simulated values (EGUN) maximum reflection alpha vs. beam current **146**

5.30 Simulated values of efficiency (in $TE_{21,13}$ mode) of microwave generation vs. perp. velocity spread for two value of alpha – 1.1, 1.44 (design $\alpha = 1.44$) **148**

List of Tables

3.1 Minimum delays, risetime of pulse across the ferroelectric, and radii of ferroelectric cathodes from MIT experiments and sources in literature **75**

4.1 TE cavity parameters from single mode code **85**

4.2 Gun parameters from analytical calculations **97**

4.3 Design parameters of the mode converter **108**

Chapter 1

Introduction

1.1 Overview

If one examines the frequency-power domain of wave generators one finds that there is only one device that is able to provide 0.1-3 MW [1-10] of microwave power in the frequency range of 35-500 GHz with high efficiency [9-10]: that is the gyrotron. Figure 1.1 shows the various sources available and their capabilities.

Conventional tubes (magnetrons, klystrons, traveling wave tubes, etc.) require structures comparable to or smaller than the wavelengths they generate. In contrast, gyrotrons have an advantage at millimeter wavelengths of relying on the interaction between the electron beam and the RF fields in the fast wave. Thus, the cavity sizes are significantly larger in gyrotrons making them able to handle more power and more total wall loading due to the additional wall area.

Since the 1960's considerable effort has been expended in trying to improve the performance of gyrotron tubes. This has meant effort to generate microwaves efficiently at higher power levels and higher frequencies per tube. The factor that limits the power generated from a gyrotron tube is the ohmic power dissipated on the walls of the tube. Thus, as more power is extracted from a tube the ohmic power on the cavity walls of the tube increases and a limit is reached, depending on the cooling, where the cavity walls would start melting if the power were increased further. This is especially true for *whispering gallery modes* which have the electron beam located closer to the walls of the tube. *Body modes* in a coaxial gyrotron are better in this respect due to the electron beam in these modes being relatively further away from the walls of the tube and due to the reduced voltage depression [11-13]. The synchronism condition between the electron and the wave is given in Eq. 1.1 below:

$$\omega = n\omega_c/\gamma \pm k_z v_z \tag{1.1}$$

where ω is the frequency, k_z is the axial wavenumber, v_z is the axial electron velocity, the cyclotron frequency is $\omega_c = eB_o/m$, n=1,2, ... is the harmonic number, and the relativistic factor is $\gamma = (1\text{-}v^2/c^2)^{-1/2}$.

For higher frequencies, the limitation has primarily been the maximum field available from superconducting magnets. There are methods to overcome the maximum field limitation of superconductors by exciting higher harmonics of the wave-beam resonance, but the price to be paid is in terms of the lower efficiencies at the higher harmonics [14].

Some of the best results that have been obtained so far are the 110 GHz gyrotron at the Communication and Power Industry (CPI) which has achieved output powers of 680 kW, 530 kW, and 350 kW for pulse lengths of 0.5, 2, and 10 seconds [1] respectively. General Atomics successfully operated a gyrotron at 1090 kW at 110 GHz for 0.6 seconds [15]. Other notable efforts were at 84 GHz in Japan [2], 110 GHz in Russia [3], 118 GHz in Switzerland [4], and 140 GHz in Germany [5], and the 2 MW at 100GHz result from Russian [12], which have all produced power in the range of 0.5-2.0 MW for 0.2-5 seconds. Another notable effort with a different device is the 730 kW at 200 GHz generated by the FEM experiment conducted Verhoeven *et al* [16].

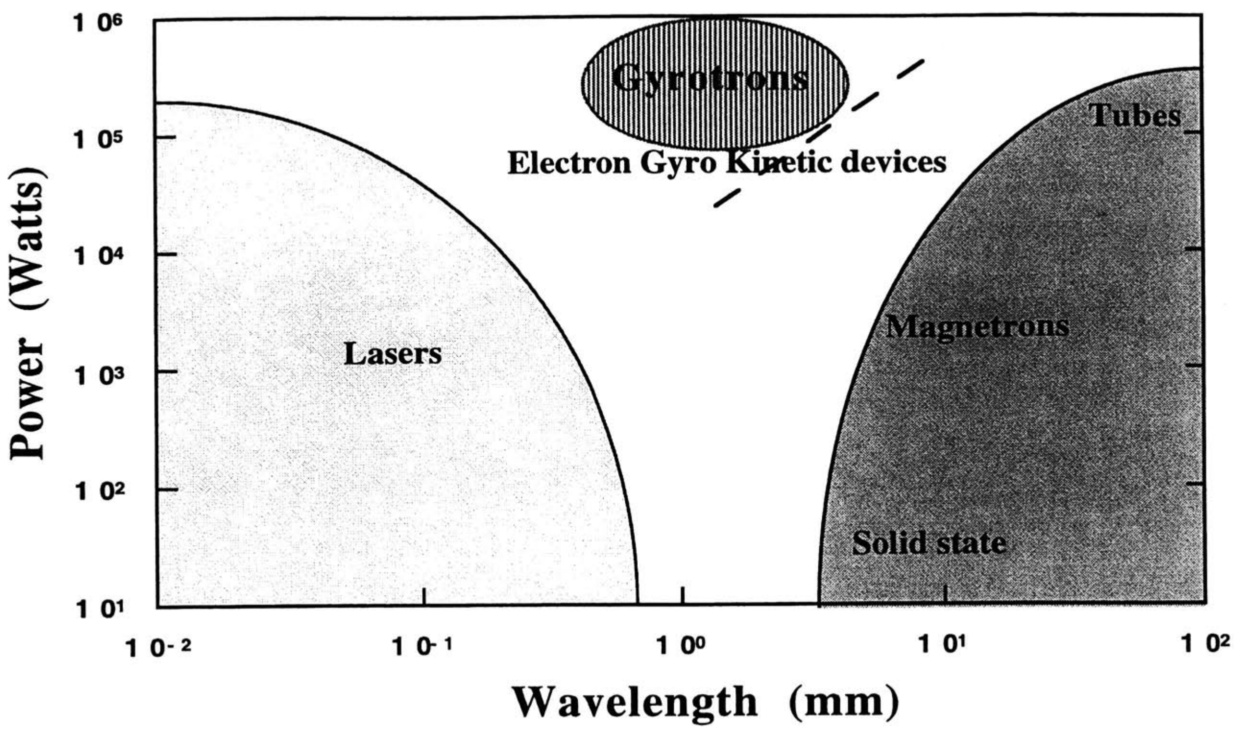

Figure 1.1: Frequency and power diagram of various sources.

The application that these gyrotrons have been developed for is Electron Cyclotron Heating (ECH) in fusion experiments. Yet, there are several other applications of megawatt level microwave power at high frequencies. These include high-frequency radar systems, communications systems, materials processing of ceramics, improved Nuclear Magnetic Resonance (NMR) imaging, high frequency broadband spectroscopy, plasma diagnostics, and several others.

1.2 Electron Beams in Gyrotrons

High beam quality electron injection guns are an integrally important part of any gyrotron. Electron guns for gyrotron tubes have to be carefully precision manufactured and have several rigid design constraints to satisfy. These include high accuracy of spacing between anode and cathode, exact concentricity of emitting area with respect to anode, and low velocity spread with reasonable $\alpha = (v_{perp}/v_{parallel})$ of ≈ 1.5. Gyrotron tubes have usually used guns called Magnetron Injection Guns (MIG) with thermionic cathodes, which require careful handling and high vacuum operation. All these conditions placed upon the gun make it difficult and expensive to manufacture. Also, these MIG guns are carefully machined to low tolerances and once welded or brazed together are difficult to take apart and modify. Thus, in order to conduct a study of efficacy of various anode shapes, these guns would be unsuitable. To this end we developed a ferroelectric cathode based electron gun which would be cheaper, not require high vacuum, and would be easier to manufacture as well as modify. The other electron beam investigation was the careful in-situ characterization of three thermionic cathodes in a coaxial gyrotron. The coaxial gyrotron experiment also proved to be a suitable test bed to draw broader conclusions between electron beam quality and the efficiency of microwave generation from a gyrotron.

Both the experiments were designed and investigated with the aid of an electron gun code called EGUN [17]. EGUN simulations also helped in the investigation of the sensitivity of the electron beam with respect to small variations in the mechanical alignment of various structures in the electron gun, and the alignment of the gun with the magnetic field of the gyrotron.

1.2.1 Coaxial Gyrotrons

Continious wave (CW) gyrotrons operating at 140-170 GHz are typically designed to produce 1 MW per tube. The primary technological limitations have been the cavity heat load, mode competition, and the maximum power that the output window can transmit.

Recent improvements in window design with double-disk, diamond, and dome-shaped windows mean that future tubes will be mostly limited by the maximum average cavity heat loading (about 3 kW/cm^2 peak loading can be handled in present designs). The coaxial gyrotron attempts to increase the microwave power generated to 3 MW per tube, thus reducing the number of tubes required and the total system costs for multi-megawatt installations e.g. for future fusion experiments.

The main advantages of a coaxial conductor in a gyrotron are:

- Causes rarefied mode spectrum around the design mode
- Reduces the quality factor of competing modes
- Body modes (higher radial index) can be chosen, decreasing the ohmic losses
- Reduces voltage depression

Due to the ability to choose a body mode in coaxial gyrotrons, greater output can be expected at the same level of cavity ohmic power. Figure 1.3 is a schematic of the differences between a *whispering gallery mode* gyrotron and a *body mode* coaxial gyrotron.

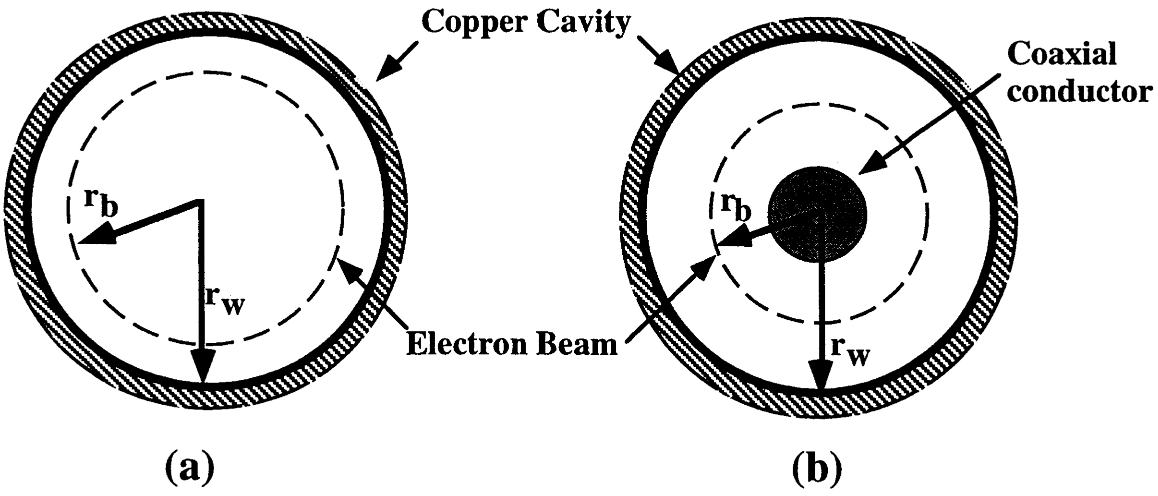

Figure 1.2: Schematic of (a) regular gyrotron oscillator in a *whispering gallery mode*, and (b) coaxial gyrotron in a *body mode*.

To quantify the differences, some typical value for r_b/r_w (r_b is the beam radius and r_w is the cavity radius) for a regular gyrotron in the *whispering gallery mode* is 0.73 [18], while the same for the coaxial gyrotron in a *volume mode* is 0.35 [11]. The cathode used in the coaxial gyrotron was a annular thermionic cathode with a emitter strip of diameter 9.8 cm and width 0.468 cm. The emitter was slanted at an angle of 25° to the axis of the tube (magnetic field axis).

Recent results from Thumm et. al. for coaxial gyrotrons have been 1.6 MW [8] at 165 GHz in the $TE_{31,17}$ mode with a efficiency of 25%, which improves to 41% with a depressed collector. They also report 1.2 MW [14] at 140 GHz with an efficiency of 27.2% in the $TE_{28,16}$ mode. The best Russian result is 2 MW at 100 GHz [12]. The best results obtained from MIT [11] have been 1 MW at 140 GHz in the $TE_{21,13}$ mode. General speculation regarding the lower performance of the coaxial gyrotrons has been that alignment of the coaxial conductor, the cavity, and the magnetic field is quite difficult. MIT's experiments have also investigated the electron beam in the gyrotron [19,20].

1.2.2 Ferroelectric cathodes

Novel ferroelectric cathodes have gained the attention of the community due to lower cost, ease in manufacture and absence of high vacuum requirement for handling and operation. These cathodes can be operated in poor vacuum, have low emittance, and high brightness characteristics. They are superior to thermionic cathodes not only in their ruggedness but also due to their instant turn-on capabilities (thermionic cathodes require heating time). With the demonstration of scalability of ferroelectric cathodes to large sizes of over 10 cm diameter and high total currents of over a kiloampere, these cathodes are potentially attractive for a multitude of high current density (5-50 A/cm^2), long lifetime (as compared to velvet cathodes), pulsed applications i.e. accelerators, microwave sources, flat panel displays, etc. [21-29]. In addition, one of the major advantages of ferroelectric guns is the ease with which several anode-cathode geometries and segmented beam shapes can be investigated. Hence the ferroelectric cathodes were used in our experiments to generate microwaves. In fact, to the best of our knowledge, we were the first group to demonstrate microwave generation with a ferroelectric cathode. We also investigated several emission characteristics of ferroelectrics cathodes in order to better understand the emission process from ferroelectrics.

Copious electron emission from ferroelectrics was first reported by Bugaev et. al. in 1968 [28]. After this result the field was relatively dormant because the ferroelectric emission was considered to be plasma based and thus unsuitable for various tube applications until some work at CERN [27] in 1989. Since then there have been several notable efforts at Tel-Aviv University [21], Integrated Applied Physics [22], Cornell University [24], and at MIT [30]. Although experimental results from all these experiments have been in the range of 10-100 A/cm^2 there is considerable variance between the groups about the emission process from ferroelectric cathodes. Explanations of the emission process have varied from bandgap switching, surface plasma on the cathode, initial energy of emitted electrons, circuit models, etc. We at MIT put forward a theory of electron emission from ferroelectrics which is based on energetic electrons being emitted from the ferroelectric surface which has a thin plasma layer on the ferroelectric cathode surface. Both these effects have been recently experimentally verified [21,31].

1.3 Thesis layout

The thesis is organized in the following manner. Chapter 2 provides a broad overview of electron guns in gyrotrons. Chapter 3 describes the experiments that were conducted with ferroelectric cathode guns. Chapter 4 describes the design of the coaxial gyrotron. Experimental results from the coaxial gyrotron are described in chapter 5. A summary is provided in chapter 6 along with suggestions for the future.

Chapter 2

Electron guns for gyrotrons

2.1 Introduction

One of the critical elements of any gyrotron oscillator is its electron beam source. The electron beam has to be of a high quality in terms of having mono-energetic electrons with a low velocity spread. One can argue that gyrotrons are a preferred over Cyclotron Resonance Maser (CRM) devices because they operate close to cutoff ($k_z v_z$ is small) allowing greater tolerance for velocity spreads, but the fact remains that the velocity spread has to be as low as possible for both transverse and parallel directions. For coaxial gyrotrons the requirements for a central coaxial conductor necessitates that the MIG gun be inverted and that the cathode be on the outside of the anode; this geometry is called an Inverted MIG (or IMIG). Both the geometries are illustrated in Figure 2.1.

This chapter covers the general principles of electron guns in gyrotron oscillator. Adiabatic theory is used to determine the qualitative scaling parameters and beam parameters. Numerical simulations are discussed and experimental arrangement to measure beam parameters is described.

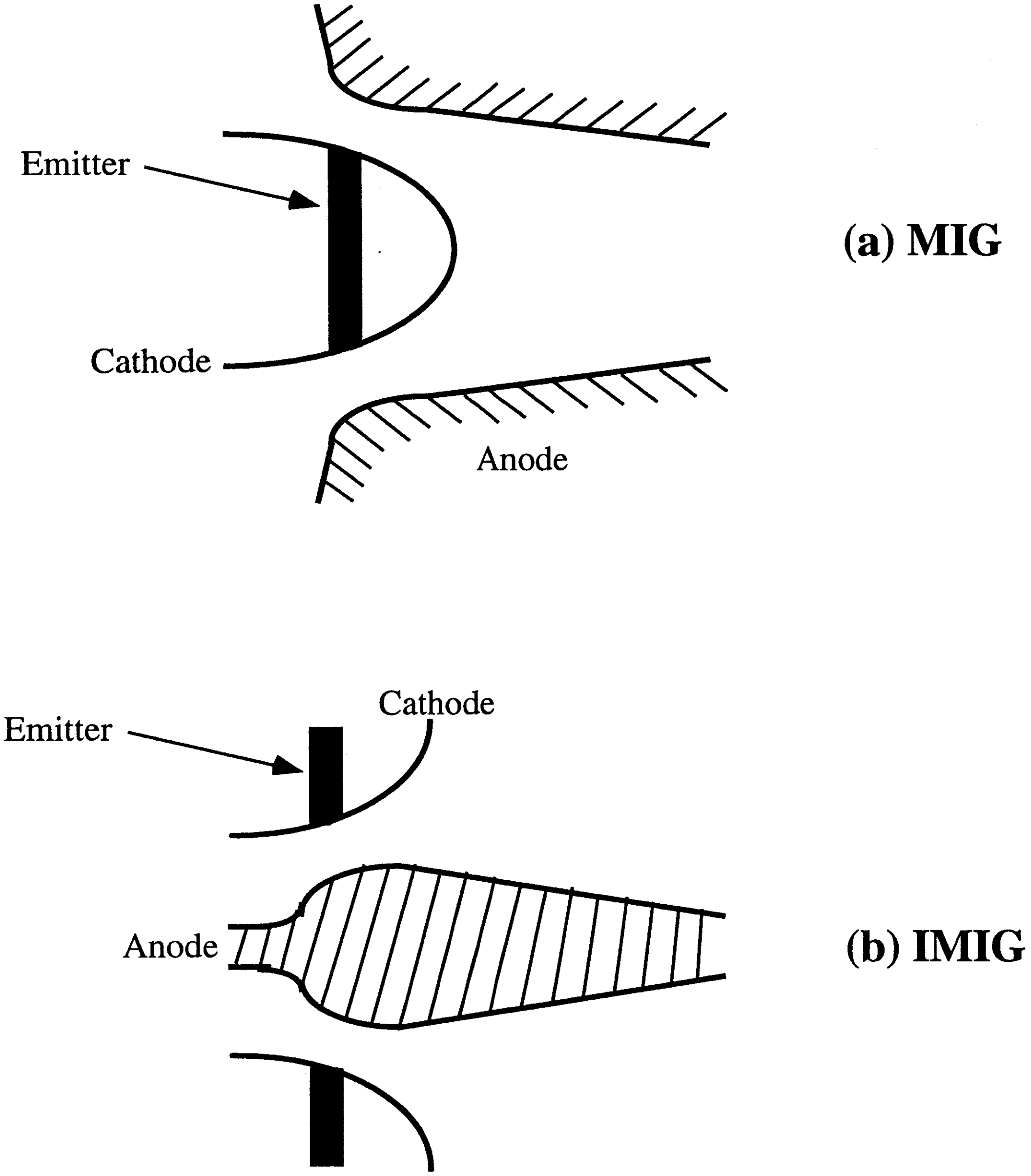

Figure 2.1: Schematic of a (a) Magnetron injection gun (MIG) with the cathode on the inside of the anode; and a (b) Inverted Magnetron injection gun (IMIG). Both the guns shown are diode guns.

2.2 Magnetron injection guns

In this section we discuss the general equations governing electron motion emitted from a cathode and accelerated toward an anode by an electric field, all immersed in a magnetic field. After that, we discuss the adiabatic approximation and some of the design parameters for gyrotron guns. Finally, we discuss the self-consistent simulations that are conducted in order to finalize the design for most gyrotron guns.

2.2.1 General electron motion equations

In order to motivate this discussion let us first introduce some of the terms and parameters related to the gyrotron oscillator. Figure 2.2 shows the schematic of a IMIG in a coaxial gyrotron oscillator. We choose the coaxial gyrotron electron gun to exemplify the design process.

The electrons are born at the cathode and are accelerated towards the anode. As one can see from Figure 2.2, this creates an initial velocity for the electrons at the cathode with a component in the perpendicular and the parallel directions (Note: the perpendicular and parallel directions are defined with respect to the magnetic field). The magnetic field grows from a value of B_k at the cathode to B_o in the cavity. Once emitted the electrons follow the magnetic field lines to the cavity where the microwaves are generated. The IMIG gun has a central shaped conductor, which serves as the anode. The cathode is an external cylindrically mounted structure with the emitting strip, which has an angle of 25° with respect to the magnetic field axis. The 25 angle has been found to be the appropriate one for this gun, in terms of giving the electrons a velocity ratio of 1.5 at the operating voltages and currents. The anode is grounded and the cathode is raised to a negative high voltage of 0-100 kV.

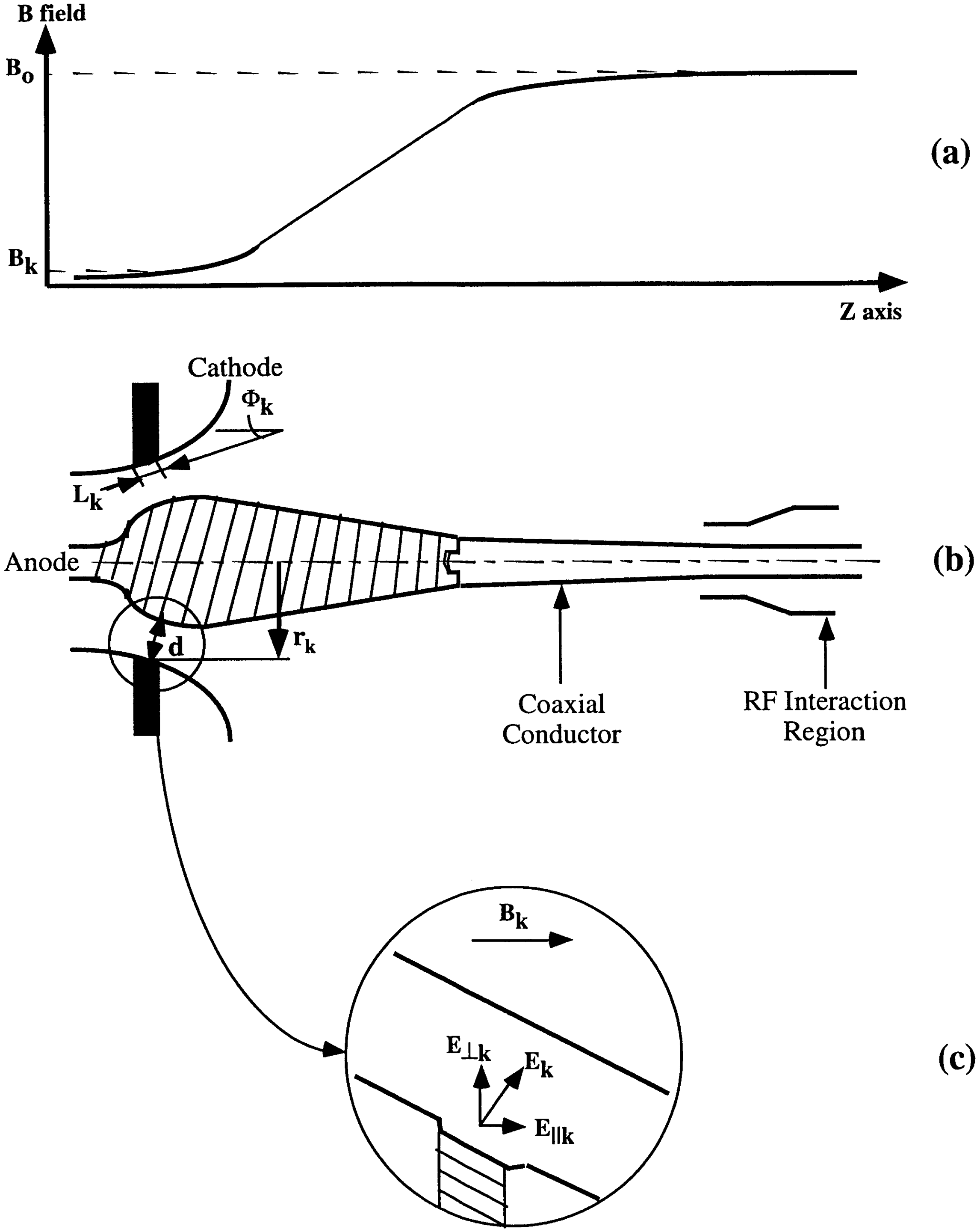

Figure 2.2: Schematic of IMIG gun with (a) the field profile, (b) general parameters and major components of a coaxial gyrotron oscillator, and (c) expanded view of cathode region.

The cathode itself is the 532M M-type dispenser cathode manufactured by Spectramat Inc [32]. This emitter is housed in a molybdenum holder, with the heater apparatus built in behind the emitter strip. The operating temperature of the strip was kept at 990°C with a emission density of 5.5 A/cm^2 [manufacturer specs. in Ref. 32].

An intuitive explanation of the IMIG gun follows. The region between the cathode emitter and the nearest anode surface has roughly constant electric and magnetic fields [33,34],

$$\overline{v}_{\perp k} = \frac{\overline{E} \times \overline{B}}{B^2} \qquad\qquad v_{\perp k} = \frac{E_{\perp k}}{B_k} \tag{2.1}$$

Thus, the electrons basically have a $\underline{E}\times\underline{B}$ drift in this gun region and are born with zero emission velocity at the cathode. Single particle electrons are also accelerated along the magnetic field with a constant acceleration of $a = F/m_e = eE_{\parallel k}/m_e$, and are given a cycloidal motion composed of cyclotron motion with a drift velocity perpendicular to the magnetic field. When the electrons get past this initial acceleration region they undergo a transition from seeing an electric field mostly perpendicular to the magnetic field lines to mostly parallel to the field lines. At the cathode, the fast change of $E_\perp$ over a single gyro period implies a non-adiabatic change and makes it possible for $v_\perp$ to be conserved as electrons go to a region where perpendicular electric field is essentially zero.

Once past this region, the electrons travel toward the cavity where the magnetic field is at its maximum. In this region the change in magnetic field is small over a gyro period. Hence the magnetic moment μ_a is conserved,

$$\mu_a = \frac{\frac{1}{2}mv^2}{B} = cons\tan t \tag{2.2}$$

Since μ_a is conserved, $v_{\perp o}$ can be written as,

$$v_{\perp o} = v_{\perp k}\sqrt{\frac{B_o}{B_k}} \tag{2.3}$$

where B_o/B_k is called the magnetic compression of the beam.

Using Eq. 2.1 and Eq. 2.3, we get,

$$v_{\perp o} = \frac{E_{\perp k}}{B_k}\sqrt{\frac{B_o}{B_k}} \tag{2.4}$$

As long as $v_{\perp o} < v$ then the electrons reach the cavity with the $v_{\perp o}$ shown above, but if the $v_{\perp o} > v$ then the electrons are reflected back toward the cathode. This can cause the electrons to be trapped and charge buildup with arcing, where v is total velocity given by the energy conservation equation below,

$$\frac{1}{2}\gamma m_e v^2 = \frac{1}{2}\gamma m_e (v_{\parallel o}^2 + v_{\perp o}^2) = e(V_c - V_{dep}) \tag{2.5}$$

where V_c and V_{dep} are the cathode voltage and space charge voltage depression.

The beam radius itself is governed by the conservation of magnetic flux given by $\Phi = B\pi r^2 =$ constant. If radius of the beam at the cathode is r_k and the magnetic field B_k, the equation above dictates that the radius in the cavity with a magnetic field of B_o is,

$$r_{bo} = r_k\sqrt{\frac{B_k}{B_o}} \tag{2.6}$$

Hence, all the magnetron injection guns have the characteristic feature of electrons being born in a region with a crossed electric and magnetic field to form a beam with cyclotron motion. To maintain the scaling between the components of velocity there has to be adiabatic compression in the ensuing region. These guns are typically operated in the temperature limited region, where the beam current is a weak function of the applied voltage, and is controlled by varying the temperature of the emitter. The advantage of operating in this regime is that the beam can be described by analytical equations since the space charge effect is weak and can be neglected.

2.2.2 Adiabatic theory

The adiabatic approximation describes the basic equations of the electron beam in the magnetron injection gun. This approximation is valid if the scale length of the variations of the electric and magnetic fields are small compared to the electron gyro motion (Larmor radius and z_L). z_L is the axial distance the electron propagates during one cyclotron period. These conditions can be expressed as :

$$\begin{array}{ll} z_L^2\left|\frac{\partial^2 B}{\partial z^2}\right| << B, & z_L^2\left|\frac{\partial^2 E}{\partial z^2}\right| << E \\ z_L\left|\frac{\partial B}{\partial z}\right| << B, & z_L\left|\frac{\partial E}{\partial z}\right| << E \end{array} \tag{2.7}$$

A constant of motion is (modified version of Eq. 2.6),

$$\frac{p_\perp^2}{2B} = constant \tag{2.8}$$

Where $p_{\perp}$ is the transverse momentum of the electron, and B is the amplitude of the magnetic field. The gun designs are usually optimized using a modified version of the electron optics code EGUN [17]. The code needs some starting parameters and the geometry of the gyrotron surfaces to calculate the alpha, the velocity spread, the beam radius and width, and the trajectories of the electrons. Typically, one simulates several geometries in the process of optimization of anode and cathode shapes for the gyrotron, taking into account the space charge effects. The EGUN code and the adiabatic design equations can then be used to design the best electrode shapes. Adiabatic MIG gun design tradeoff equations [35] are shown in Eq. 2.9 to 2.15 (where the k subscript refers to values at the cathode).

Eq. 2.9 is a modified version of Eq. 2.6, which describes the beam radius in the cavity in terms of the beam radius at the cathode and the beam compression from the cathode to the cavity. Eq. 2.9 shows the guiding center of the trajectory (after the first Larmor radius) by introducing $\mu = r_{lk}/ r_k$, where r_l is the Larmor radius. Eq. 2.10 shows the cathode slant angle (ϕ_k) and is a modification of Eq. 2.4 for $v_{\perp}$ taking into account the angle of the cathode with respect to the magnetic axis. Eq. 2.11 shows the current density (J_k) in terms of the cavity parameters or beam radius (r_b) and beam guiding center thickness (Δ_b) assuming the electrons follow field lines. The emitter thickness (L_k) is then calculated in Eq. 2.12 using the current density and simple area calculations. Eq. 2.13 relates the gap distance (d) to the equivalent Larmor radii, $D_f = d/r_{lk}$. Eq. 2.14 is the parallel plate equation relating the electric field near the cathode to the voltage and the distance, which is valid provided $r_k >> d$. Finally, Eq. 2.15 compares the current density (J_k) to the space charge limited current (J_l) from the Child-Langmuir limit to provide a feeling for the space charge limitation of the beam.

$$\frac{B_k}{B_o}=\frac{\mu^2 r_k^2}{r_{lo}^2} \tag{2.9}$$

$$\phi_k=\cos^{-1}\left(\frac{v_{\perp o}B_o\gamma_o}{(B_o/B_k)^{3/2}E_k}\right) \tag{2.10}$$

$$J_k=\frac{r_b}{\Delta_b}\frac{\sin\phi_k}{1+\mu^2}\frac{I}{2\pi r_k^2} \tag{2.11}$$

$$L_k=\frac{I}{2\pi r_k J_k} \tag{2.12}$$

$$d=\frac{D_f\mu r_k}{\cos\phi_k} \tag{2.13}$$

$$V_a=E_k d \tag{2.14}$$

$$\frac{J_k}{J_l}=\frac{9d^2}{4\varepsilon_o}\left(\frac{m_e}{2e}\right)^{1/2}\frac{J_k}{V_a^{3/2}} \tag{2.15}$$

If we examine all the variables and the equations we observe that we have 16 variables and 7 equations [34] :

Variables: Gun (10) ϕ_k, r_k, L_k, d, D_f, V_a, J_k, B_k, E_k, J_k/J_l

Cavity (6) α, r_b, Δ_b, B_o, V_o, I

Besides the 7 equations, we also have 6 variables, which are already specified from the cavity – requiring three more to be fixed. These three come from physical constraints of technology which have been observed and studied over the years. They are:

$$B_o/B_k < 40 \tag{2.16}$$

$$J_k < 10\ \text{A/cm}^2 \tag{2.17}$$

$$E < 100\ \text{kV/cm} \tag{2.18}$$

The compression ratio is limited based on previous experience that a larger compression ratio leads to the trapping of some of the electrons causing greater risk of arcing and poor beam quality. The cathode emission itself being limited to lower than 8-10 A/cm^2 is due to lifetime considerations for standard thermionic dispenser cathodes of operation for longer that 90,000 hours [36]. Finally, the electric field being limited to 100 kV/cm is due to the Kilpatrick criterion for CW tubes [37]. Besides these, there is the requirement to keep current density low is a recognition of the fact that as space charge effects start to begin affecting the beam (shown in Eq. 2.19) – we see a greater velocity spread in the electrons leading to poor beam quality and lower efficiency of gyrotron interaction.

$$J_k/J_l \quad < \; 15\% \tag{2.19}$$

The adiabatic design equations demonstrate the tradeoff's that are required between parameters. To maintain a constant α and beam radius in the cavity for larger electric fields at the cathode, one has to decrease J_k / J_l and r_k. The criterion that electric field needs to be kept below 50 kV/cm is usually enforced on the design since electric field would be below the 100 kV/cm at any corners in the design. The $D_f = d/r_{lk} = 4\text{-}8$ criterion is in order for the electron beam to be sufficiently far away from the anode, giving room to play experimentally in lowering the magnetic field.

2.2.3 Self Consistent EGUN Simulations

After the first cut parameters were developed from the adiabatic tradeoff equations and the required cavity parameters, further optimization of electrode shapes was done using a widely used electron optics code called EGUN [17]. The code computes electron trajectories in electrostatic and magnetostatic fields. The code also takes into account the space charge, self magnetic field, and relativistic effects. Problems can be solved in rectangular or cylindrical geometries (assuming axis symmetry). The code itself solves the Poisson's equation by finite difference method using the boundary conditions defined by the user i.e. position and type of boundary (Dirichlet or Neumann). Electric field is determined by differentiating the potential distribution. The beam itself is divided into a number of distinct beamlets with defined starting points along the user defined emitter strip. The trajectories are then calculated including all fields (electric and magnetic) as well as any relativistic effects. Space charge is calculated by appropriate charge density assignment to various grid points. A self-consistent solution is derived iteratively.

From a users perspective, the parameters that need to be entered are :

- A first cut geometry of the electrode shapes, a guide for which is previous design files which have been used over the years and some tweaking with respect to needs of the new gun being designed.
- Magnetic field profile, which can quite simply be input if the magnet already exists or a previous magnet's profile can be used as a guide.
- Voltages on the electrodes and current density of the emitter strip
- Simulation parameters – mesh size, number of iterations, etc.

Using this and knowing the values in the cavity of α, beam radius, and velocity spread one can experiment with electrode shapes till a optimum has been reached.

The most recent version of the modified EGUN code provides up to 3×10^6 mesh points for the iteration, and utilizes a four-point weighting scheme to figure out the space charge [33]. The large number of mesh points means that we are now able to simulate the electron beam from the gun to the cavity in one section with a small enough mesh size, to provide meaningful results.

2.3 Cavity and Beam Tunnel

In this section we discuss some of the critical beam parameters and their measurements. These include voltage depression, limiting current, velocity spread, velocity ratio, and energy spread. We also describe two techniques that we used to investigate the azimuthal symmetry of the electron beam.

2.3.1 Voltage depression and limiting current

The electron beam emanates at the cathode, is transported to the cavity and finally collected at the collector. During this transport, the space charge in the beam causes the potential within the beam to be reduced with respect to the ground potential nearby. In a cylindrical tube of radius r_w, the potential depression V_{dep} between the tube and the axis of symmetry due to a concentric electron beam with uniform current density is given by:

$$V_{dep} = \frac{1}{4\pi\varepsilon_o c}\frac{I_b}{\beta_{\parallel}}G(r_i,r_b,r_w) \tag{2.20}$$

where $G(r_i, r_b, r_w)$ is a geometrical factor which is defined as,

$$G(r_i,r_b,r_w) = 2\ln\left(\frac{r_w}{r_b}\right) \tag{2.21}$$

and with a coaxial insert of radius r_i, the geometrical factor simply changes to,

$$G(r_i,r_b,r_w) = 2\ln\left(\frac{r_b}{r_i}\right)\frac{\ln\left(\frac{r_w}{r_b}\right)}{\ln\left(\frac{r_w}{r_i}\right)} \tag{2.22}$$

In both the equations r_w is the cavity radius, r_b is the beam radius, and r_i is the inner radius of the coaxial conductor (if any). This equation is true with the approximation that the radius of the electron beam far exceeds the thickness of the beam.

Once we know the voltage depression, the limiting current can be determined for a given transverse momentum and cathode voltage. If the current is increased to the point that it exceeds the limiting current, then the axial velocity reduces to zero and the beam starts to get reflected back towards the cathode. The relativistic mass factor is this case can now be written as (where V_c is the cathode voltage),

$$\gamma = 1 + \frac{e(V_c - V_{dep})}{m_e c^2} \tag{2.23}$$

And a combination of Eq. 2.20, 2.22, and 2.23 gives us:

$$I_b = 4\pi\varepsilon_o c \frac{\beta_\parallel}{G}\left(1 + \frac{eV_c}{m_e c^2} - (1 - \beta_\perp^2 - \beta_\parallel^2)^{-1/2}\right) \tag{2.24}$$

The limiting current by definition can then be defined as the maximum one with respect to the parallel velocity (keeping the transverse momentum constant):

$$\left.\frac{\partial I_b}{\partial \beta_\parallel}\right|_{\gamma\beta_\perp = const} = 0 \tag{2.25}$$

Hence we get the limiting current as:

$$I_L = 1.707 \times 10^4 \gamma_o \left[1 - (1 - \beta_{\parallel o})^{1/3}\right]^{3/2} \frac{1}{G(r_i, r_b, r_w)} (Amps) \tag{2.26}$$

where γ_o and $\beta_{\parallel o}$ are values in the absence of voltage depression. In this case too the appropriate G factor should be used from Eq. 2.21-2.22 depending on whether the calculation is being made for a regular gyrotron or a coaxial gyrotron. Velocity spread is a contributor in reducing the limiting current [38], beam reflections should not occur if $I_L/I_b \geq 2$.

2.3.2 Velocity Spread

Although most of the electrons produced by the IMIG gun have about the same total energy, there are differences in the distribution between the perpendicular and the parallel components. This leads to electrons having slightly different parallel and perpendicular velocities i.e. a velocity spread between different electrons. The relation between the perpendicular and parallel components of the velocity spreads can be obtained from the conservation of energy and can be approximated as:

$$\frac{\Delta v_{\parallel}}{v_{\parallel}} = \alpha^2 \frac{\Delta v_{\perp}}{v_{\perp}} \tag{2.27}$$

The effect of the velocity spread is the reduction of the interaction efficiency which produces RF power in gyrotrons. The reason for this is that when there is a velocity spread only a part of the electrons can maintain the synchronism condition of Eq. 1.1: experimentally one can try and maximize that fraction, but some reduction in efficiency is inevitable with increasing velocity spread. The second reason is that the maximum velocity ratio that one can reach experimentally is one where reflections of some of the electrons starts. Thus, greater velocity spread limits this average velocity and thus the maximum velocity ratio. This limitation in velocity ratio further limits the ability to reach high efficiency regions of interaction.

The primary cause of this velocity spread is the finite length of the emitter. Electrons are emitted from different parts along the emitter and therefore experience slightly different electric and magnetic fields. The electron beam space charge also adds to the velocity spread. If the electron flow is not optimized in the gun region this effect is enhanced in the vicinity of the emitter region due to entangled electron paths. This is one of the primary reasons that the cathode slant angle is usually kept below 25°, above which non-laminar flow results [33]. The EGUN code numerically simulates the beam optics and the space charge effects. Therefore, a careful set of design simulations with EGUN can greatly improve the design and reduce the spread due to these effects. Besides optics and space charge effects the factors affecting velocity spread are [33]:

- Lack of axis-symmetry in cathode magnetic field
- Lack of axis-symmetry in cathode electric field
- Thermal spread and temperature variations around the cathode emitter
- Random roughness of the cathode surface
- Non-uniform emission density
- Space charge instabilities
- Space charge variations due to reflected electrons

All the above spreads (except the last two ones) add to the spread at the initial velocity of the electrons at the cathode. All these spreads are also adiabatic constants of motion along the beam path all the way to the interaction region. Hence, assuming that they are uncorrelated, they can be added up according to a statistical sum as,

$$\left(\frac{\Delta v_\perp}{v_\perp}\right)_{total} = \left[\sum_{i=1}\left(\frac{\Delta v_\perp}{v_\perp}\right)_i^2\right]^{1/2} \tag{2.28}$$

2.3.3 Energy Spread

The previous section assumed that there was no energy spread between the electrons of the beam. Yet, there are some sources of energy spread for the electrons. Energy spread in general reduces the efficiency of the gyrotron. This has been calculated [39] as a reduction of 10% in efficiency for a 8% energy spread $\Delta\gamma/(\gamma_0 - 1)$.

There are three main sources of this energy spread. The first is the finite beam thickness and the voltage depression across the beam. This energy spread can be calculated as [34],

$$\Delta E_{spread}(keV) = 0.015 \frac{I}{\beta_\parallel} \frac{\Delta_b}{r_b} \tag{2.29}$$

where r_b is the beam radius and Δ_b is the thickness of the beam. The energy spread in Eq. 2.27 is halfway across the beam. Thus, on the outermost edge of the beam the energy of the electrons is $E_{kinetic} + \Delta E_{spread}$, while the energy on the innermost edge is $E_{kinetic} - \Delta E_{spread}$. In most gyrotrons this spread turns out to be small and can be usually neglected. In the case of the coaxial gyrotron (to be described in chapter 4), this spread was calculated to be only 0.16 %.

Another factor that introduces energy spread is electrostatic instabilities. These have been studied by Tran. *et al* [40] using particle-in-cell codes. They found that energy spread due to Bernstein modes depends on normalized density $(\omega_p/\Omega_{c0})^2$, where the plasma frequency is $\omega_p = n_e e^2/\varepsilon_0 m_e$ and $\Omega_{c0} = eB_0/m_e$ is the non-relativistic electron cyclotron frequency in the cavity. The usual spread from this tends to be of order 3% reducing the interaction efficiency by ~2% [39].

The last component of energy spread is due to collisions. Since the electron-electron collision rates are typically small and the high-vacuum tubes of today virtually eliminate electron-neutral and electron-ion collisions, this effect can usually be neglected.

2.3.4 Velocity ratio measurement

The velocity ratio can be measured by the capacitive probe technique. Here, with the knowledge of the beam current and the indirect measurement of one of the parameters $v_{\parallel}$ (through a capacitive effect) one can ascertain the velocity ratio of the beam. The advantage of the capacitive probe is that it is a passive measurement technique that is able to measure the charge density of the beam passing through it fairly accurately. The capacitive measurement therefore measures the axial charge density from which the electron flux density can be determined. This is then used along with the Rogowskii measurement of the total current to give us the value of $v_{\parallel}$. Thereafter, with the use of energy conservation and potential used to accelerate the electron beam (V_c-V_{dep}) one can calculate $v_{\perp}$. The velocity ratio is then just the ratio of $v_{\perp}/v_{\parallel}$.

To quantify this technique, let us consider an electron beam of radius r_b going through a capacitive probe which has a radius r_{cap}. The radial electric field extends from the beam to the wall of the tunnel or capacitive probe. Now these two concentric cylinders of length l can be modeled as a capacitor. Then, the voltage measured by this probe would be of order $V_{cap} = Q/C_{cap} = \lambda_e l/C_{cap}$ where C_{cap} is the capacitance of the probe and λ_e is the charge per unit axial length of the beam.

If the current measured after the probe, at the collector, is I, then noting that I= $v_{\parallel}\lambda_e$, the parallel velocity can be calculated as,

$$v_{\parallel} = \frac{1}{C_{cap}} \frac{I}{V_{cap}} \qquad (2.30)$$

Using this calculated value of $v_{\parallel}$ and knowing the accelerating potential V_c as well as the voltage depression V_{dep}, one can calculate $v_{\perp}$ using the energy conservation equation. Eq. 2.31 and 2.32 are the equations required to finally calculate the velocity ratio α:

$$\gamma^2 = \left(1 + \frac{V_c(kV) - V_{dep}(kV)}{511}\right)^2 = \frac{1}{1-\beta^2} \qquad (2.31)$$

$$\alpha = \frac{v_{\perp}}{v_{\parallel}} = \left(\frac{v^2}{v_{\parallel}^2} - 1\right)^{1/2} \qquad (2.32)$$

The probe described above is usually placed adjacent to the cavity due to two reasons. The first is that around the cavity region the B field tends to have a negligible component in the perpendicular direction and most of the $v_{\parallel}$ measured is the true value as opposed to some reduction due to a angle effect. The other reason is that theoretically speaking, we would like to measure velocity ratio in the cavity, and the closer we get to the cavity the more accurate is the measurement.

Although one can analytically calculate the actual capacitance [34], during the experiment itself one almost never uses this method due to stray capacitances, and non-concentric cylinders. The equation that is used is,

$$v_{\parallel} = A\frac{I}{V_{cap}} \qquad (2.33)$$

Here the constant A can be determined in several ways. The method that can be used in-situ to provide a representative value of A is by using a low α mode. Here, the α is intentionally reduced by increasing the cathode magnetic field and reducing the accelerating voltage to a minimum with reasonable current. Then, an assumption is made that most of the velocity component of the electrons is in the parallel direction and hence the constant A is calculated using the measured values of I and V_{cap} and using Eq. 2.33.

2.3.5 Rotating probe measurement of current

One of the other diagnostics designed and implemented by us was the rotating probe for measuring the azimuthal symmetry of the electron beam. The electron beam has the highest density in the cavity region where the magnetic field is the strongest, making the compression of the beam the greatest. The density decreases on either side of the cavity as the beam expands according to the Eq. 2.6. High densities of the beam actually cause local melting of any probe that one puts in its way (this effect is further discussed in section 2.3.5). Hence the place to measure the beam symmetry is at the place where its density is the lowest i.e. either near the cathode (unrealistic due to mechanical reasons) or just before it strikes the collector (where we measured it).

Figure 2.3 shows a schematic of the rotating probe apparatus. The central elements of the system are a rotating feed-through which can be rotated from 0° to 360°, a 30° sector which actually collected the current, and a connecting rod. Additionally, the sector was built with a hood section in order to guarantee that all the current in the 30° sector was being collected. The sector, the rod, and the feed-through were connected rigidly, so that when the feed-through was rotated on the outside of the tube, the sector moved in lock step with it on the inside of the tube. The entire assembly was tested and verified before the tube was evacuated. During the experiment, the sector was rotated and measurements were taken in 30° steps. The measurements were taken for several different current levels, voltage levels, and cathode heater levels in order to get a complete picture of the performance of the cathode. Finally, the results were plotted and compared against other techniques which had been used to measure the azimuthal symmetry of the beam.

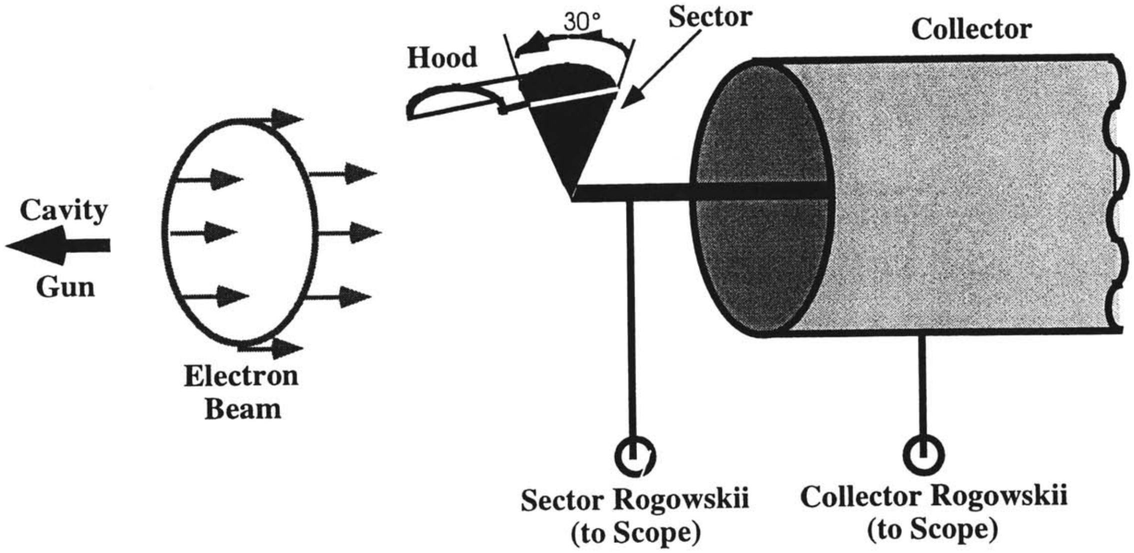

Figure 2.3: Schematic of rotating probe used to investigate azimuthal symmetry of electron beam.

2.3.6 Witness plate measurement

In order to verify that the beam was indeed azimuthally asymmetric a definitive test one can conduct is the witness plate test. Here, a copper plate is introduced in the path of the beam. When the electron beam strikes this plate it creates localized melting at the place where it strikes the copper. This causes an impression of the beam to be formed on the copper. From this impression one can see azimuthal variations, beam radius, and beam thickness. One has to be careful when garnering quantitative information from this test since the localized impression on copper is a non-linear function of beam current density. The strength of this test is its simplicity and that it can be used to either prove or verify large azimuthal variations in beam current density. The rotating probe test is better suited to careful quantitative variation analysis for the beam.

2.3.7 Temperature measurement

To investigate the source of the azimuthal symmetry in the current, a final test was done on the cathode. For this, we shipped the cathode to a large cathode manufacturer (Communication Power Industries - CPI) where the experiments were conducted by the author using CPI's equipment. Here, the temperature variation, which was though to be a major factor in the asymmetry, was measured with the help of an optical pyrometer. The test consisted of a simple bell jar made of clear glass which could be evacuated. The cathode was placed inside the bell jar and the pressure was maintained at 10^{-7} Torr or better. The bell jar had connectors inside it that could feed the heater power. The optical pyrometer was outside the bell jar and give digital readouts of temperature with an accuracy of 2°C. The pyrometer itself is capable of measurements in the range of 750°C to 1300°C. It worked on the principle of an internal rheostat wire (whose temperature could be controlled) being superimposed on the image of a particular spot on the cathode. The rheostat temperature could be varied with a knob until it was the same color as the image. At this point, the temperature reading was taken from the custom digital meter connected to the rheostat which gave a readout of the temperature in degrees celcius. A schematic of the apparatus is shown in figure 2.4.

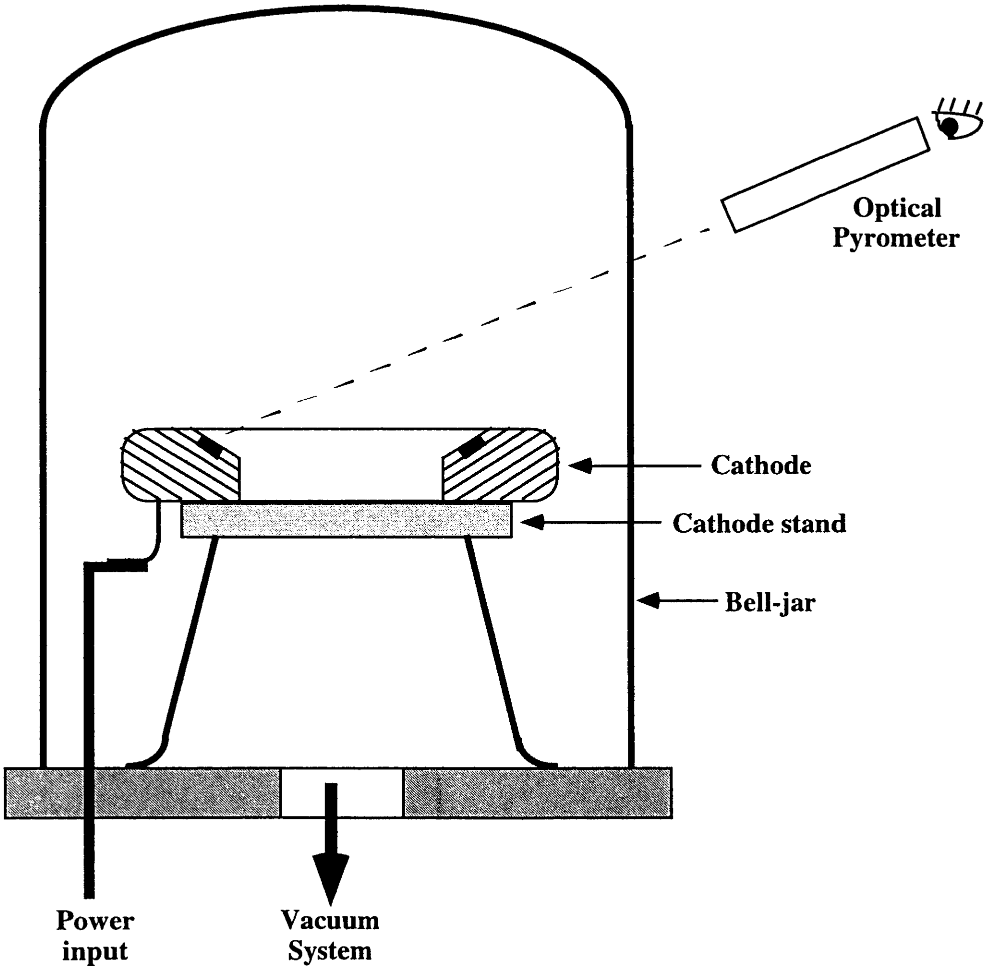

Figure 2.4: Schematic of temperature measuring apparatus used to investigate the azimuthal symmetry of the temperature of the cathode emitter.

The cathode was thus heated in the bell jar and temperature measurements were made for four different power levels – 256 W, 428 W, 500 W, and 562 W. We measured the temperature at four different locations 0°, 120°, 180°, and 240°. These angular positions were chosen because this is where we expected to see the largest temperature variations i.e. we expected the coldest spot to be at ~ 0° and the hottest spot at ~ 240°. Each of the readings was taken by two people (Mark Guaraglia of CPI and myself) in order to verify the reading.

This page intentionally left blank.

Chapter 3

Ferroelectric cathode experiments

3.1 Introduction

In this chapter, we describe the experimental results of the operation of two ferroelectric cathodes of relatively large size to prove the scalability of these cathodes. Then we describe an experiment conducted to demonstrate microwave generation from ferroelectrics, and the investigation of emission characteristics of ferroelectrics.

The first large cathode had a diameter of 10.2 cm and was built in the Pierce cathode geometry at Integrated Applied Physics (IAP). The author helped operate this experiment which was designed and fabricated at IAP. It achieved emission currents of up to 1.2 kA (15.3 A/cm^2) at voltages up to 100 kV, in 150 ns pulses. The second cathode had an annular shape with a diameter of 11.4 cm and a width of 0.25 cm. It was built at MIT to produce an annular electron beam for use in a Gyrotron microwave source. It operated at currents of up to 10 A (1.1 A/cm^2) at 8 kV, in 5 μs pulses. Detailed operating characteristics for each of these electron sources is reported. These results indicate that ferroelectric cathodes can be used to produce electron beams of large area and size, with high total operating current and pulse lengths of several microseconds. These sources should be suitable for use in future microwave generation experiments.

Most ferroelectric cathode experiments have been performed using cathodes with a diameter of 2-4 cm and a thickness of 1-2 mm [21-30]. The currents that have been obtained are of the order of tens of amperes [21-30] with current densities of order 10-100 A/cm^2, and pulse lengths of about 100 ns to 1 μs [see refs. 21-30 and references therein]. Thus, the experiment with a 10.2 cm planar cathode built in a Pierce geometry, and an annular beam experiment using a 12.2 cm ferroelectric disk demonstrate the scalability of ferroelectric cathodes to sizes and beam shapes required in many applications.

Experiments investigating the emission characteristics were conducted jointly at Tel-Aviv University [31]. Here we successfully achieved a perveance of over 65 μP and an energy spread of 100 eV (FWHM) from a ferroelectric gun. Successful experiments were also conducted demonstrating the first ever generation of microwaves using a ferroelectric cathode [41].

In spite of all the advantages and demonstrated scalability, the process of ferroelectric emission from cathodes is not well quantified. Attempts have been made over the last few years to explain the process of electron emission from ferroelectrics [21,29,42,43,44]. The traditional explanation is that the emission results from a polarization switching effect, which is initiated by a pulse across the ferroelectric cathode [44]. The polarization switching causes electrons, which are in the surface layer to be emitted. A second explanation is that the electron emission is caused by a plasma layer, which is formed on the surface of the ferroelectric when it is switched [29,45]. Recent experiments at Tel-Aviv Univ. [21,46] have confirmed the presence of a plasma with a density of 10^{10}-10^{12} cm^{-3} on the ferroelectric cathode surface. Experiments have also confirmed the presence of high energy electrons, of order a few keV, being emitted from the cathode surface [27,46]. The experiments described in this chapter demonstrate the scalability of ferroelectric cathodes to high total currents and long pulselengths. Some discussion is also provided regarding the emission process from ferroelectrics.

3.2 Large area Ferroelectric Cathode Experiments

For both the experiments described below, there is a pulse applied across the ferroelectric to initiate emission, and another pulse between the anode (stainless steel plate) and cathode (ferroelectric disk emitting side) to transport the electrons from the cathode to the anode. The usual value of the pulse across the ferroelectric is 1-2 kV, and the pulse applied across the anode-cathode gap is in the range of 0-100 kV. The delay between the ferroelectric pulse and the anode-cathode pulse can be arbitrarily varied from 0 to 12 μs in both experiments.

3.2.1 Planar beam experiment

The planar cathode experiment employed a 10.2 cm diameter, 1 mm thick LTZ-2 ferroelectric disk (made by Transducer Products [47]), that was designed and operated at Integrated Applied Physics (IAP). The pattern etched into the silver on the emitting side of the ferroelectric consisted of a honeycomb pattern with the distance between the parallel sides of the hexagon of 200 μm, and an overall transparency of 40 %. It was constructed to have an emitting diameter of 10.0 cm (part of the 10.2 cm disk was covered by the mechanical holding structure for the ferroelectric disk) and had a Pierce geometry which was designed using EGUN [17]. Thus the total emitting area was 78.5 cm^2. The ferroelectric was poled and had a relative dielectric constant of 2100 [47]. The schematic of the gun is shown in Figure 3.1. A cylindrical glass insulator whose diameter was 24.8 cm and length was 23.5 cm, separated the anode and cathode. The anode-cathode distance was 4 cm. The base pressure was maintained at 10^{-6} Torr.

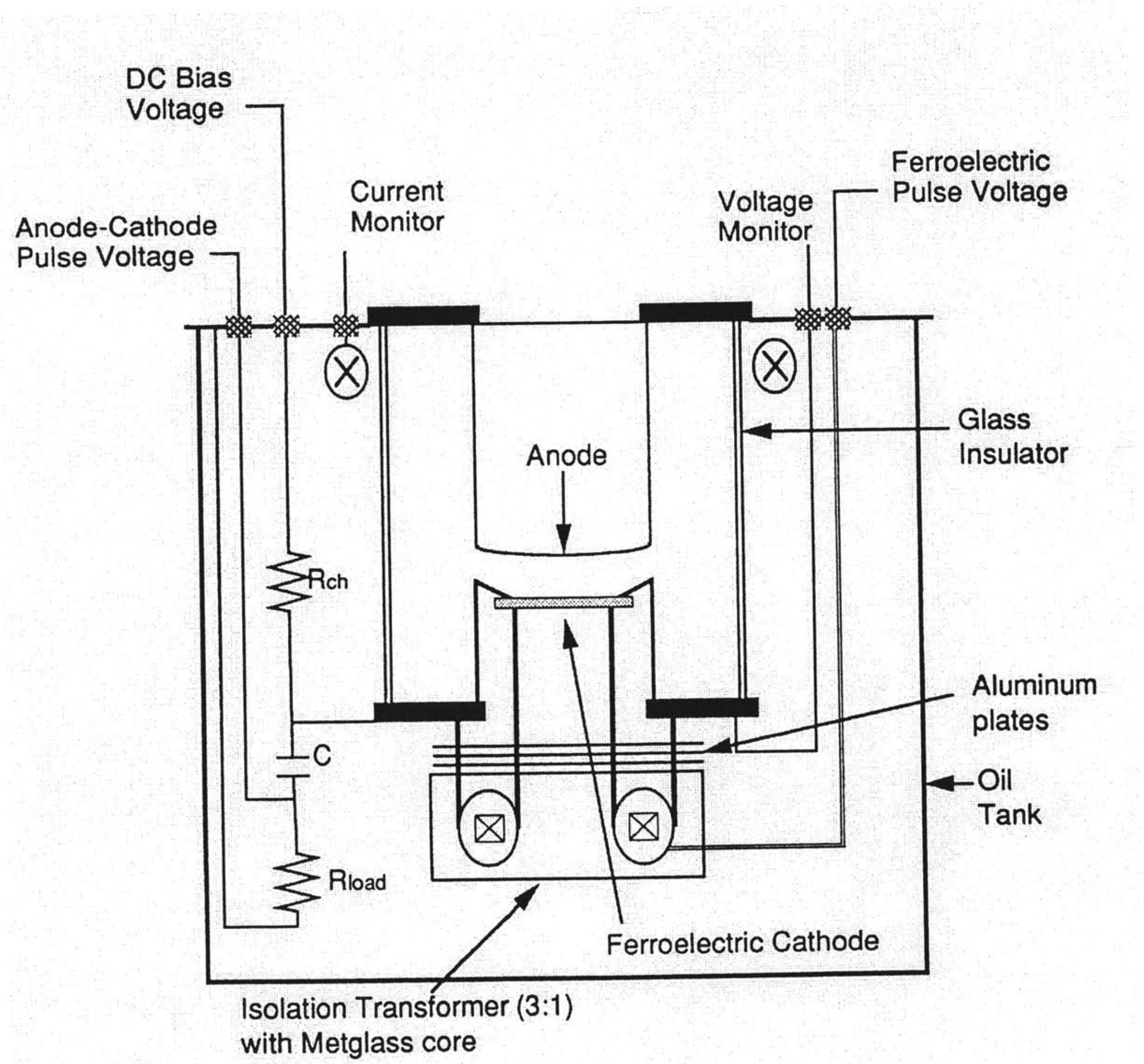

Figure 3.1: Schematic of the planar ferroelectric cathode gun at IAP with a diameter of 10.2 cm and a anode-cathode gap of 4 cm.

The electrical setup used to drive the ferroelectric had an isolation transformer and a stack of Aluminum plates to grade the high anode-cathode voltage down in steps. The ferroelectric pulse was thus applied to the 130 nF ferroelectric cathode through the metglass core isolation transformer. The ferroelectric driver pulse was 1 kV, 700 A, and had a risetime less than 300 ns. The isolation transformer itself was built by IAP for this experiment, and had a metglass core with a 3:1 step-down ratio. A 10 Ω transmission line with a Thyratron switch was used to provide the pulse at the primary of the metglass transformer.

The diode was rated at 200 kV with a design electric field strength of 50 kV/cm at the cathode. A glass insulator holding the ferroelectric cathode was suspended in an oil tank as shown in Figure 3.1. The pulse applied across the ferroelectric, V_{fe}, is shown in Figure 3.2, where a positive potential of 1 kV is applied to the back of the ferroelectric (with respect to the front emitting side of the ferroelectric). The accelerating potential, V_{ak}, and the observed beam current are shown in Figure 3.3. One observes that the total beam current, I_{ak}, obtained in this shot was ~1000 A. From the time axis one can see the shot shown in Figure 3.3 has a delay of 6 μs with respect to the beginning of the pulse across the ferroelectric (Figure 3.2). The accelerating potential (V_{ak}) was applied using a Marx bank whose output voltage was varied in the range of 15 - 100 kV, although most of the data presented here is of voltages up to 65 kV. The diagnostic for measuring current was a custom-made Rogowskii coil mounted around the glass insulator (Figure 3.1). The anode was a steel cylinder maintained at a distance of 4 cm from the cathode.

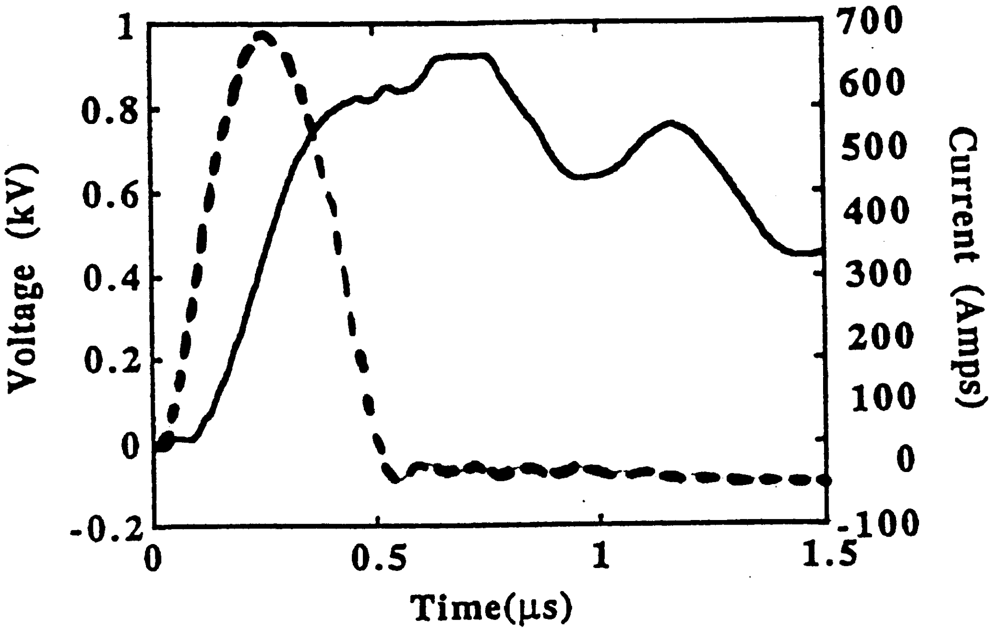

Figure 3.2: Pulse applied across the IAP planar ferroelectric cathode to excite emission - V_{fe}(solid line), I_{fe}(dashed line).

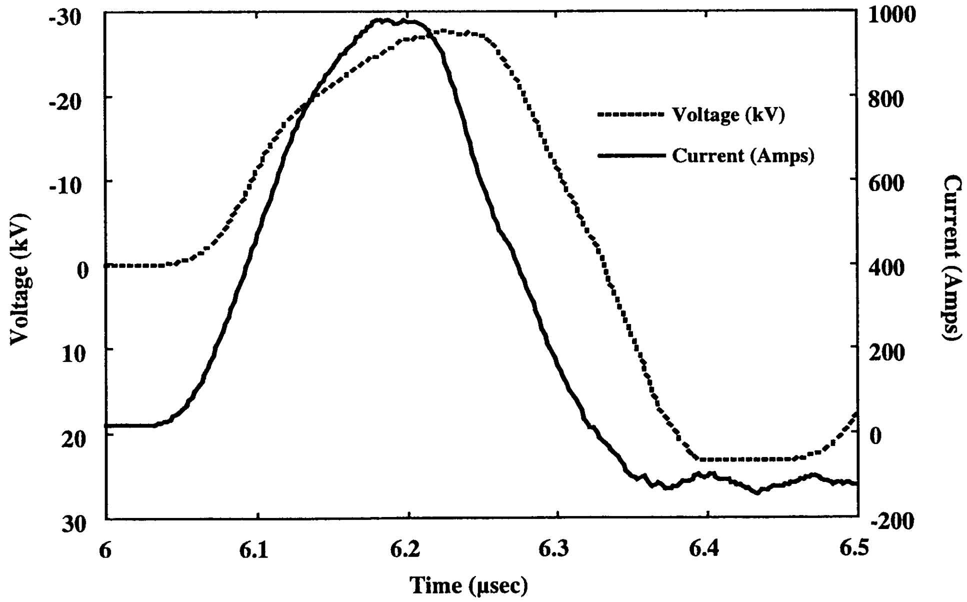

Figure 3.3: Accelerating potential (~30 kV) and emitted current (~1000 A) for the planar ferroelectric gun. This pulse follows that in Fig.2 by 6 μs.

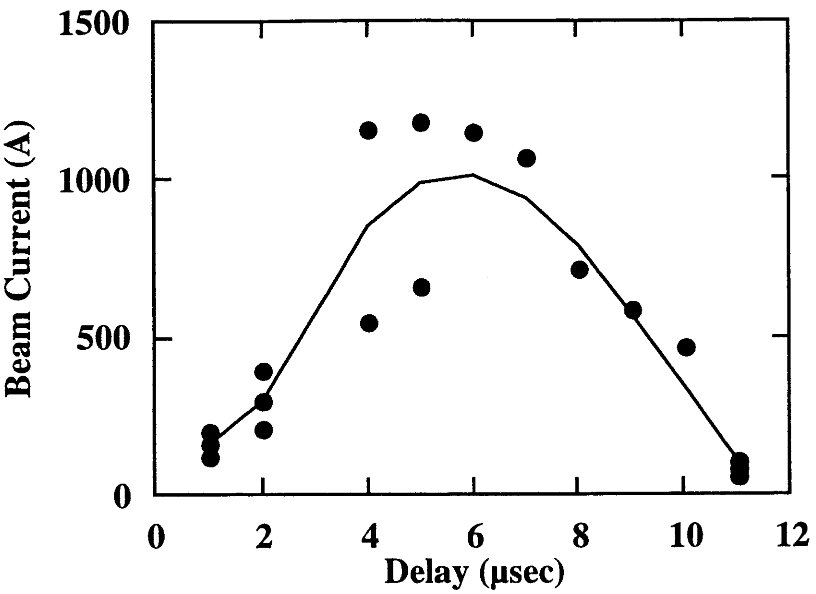

Figure 3.4: Beam current vs. delay between the pulse applied across the ferroelectric and the accelerating pulse across the anode-cathode (V_{ak} =50 kV).

Another parameter measured was the beam current versus the delay between the application of the pulse across the ferroelectric and the application of the anode-cathode accelerating potential. The results of the observed current vs. the delay are shown in Fig.4. This measurement was made with the anode-cathode voltage set at 50 kV. The V-I characteristic of this gun is shown in Figure 3.5. One observes that the maximum current in this case was just 325 Amps and the diode impedance was ~200 Ω (data at 2 µs delay). One should note that the V-I curve shown in Figure 3.5 was for 2 µs delay, while higher currents were obtained for delays ~5 µs. Also shown in Figure 3.5 is the current predicted for the diode with space charge limited flow i.e. the Child-Langmuir limit [48]. Current in excess of the Child-Langmuir limit has been observed in previous experiments [21-29] and discussed therein.

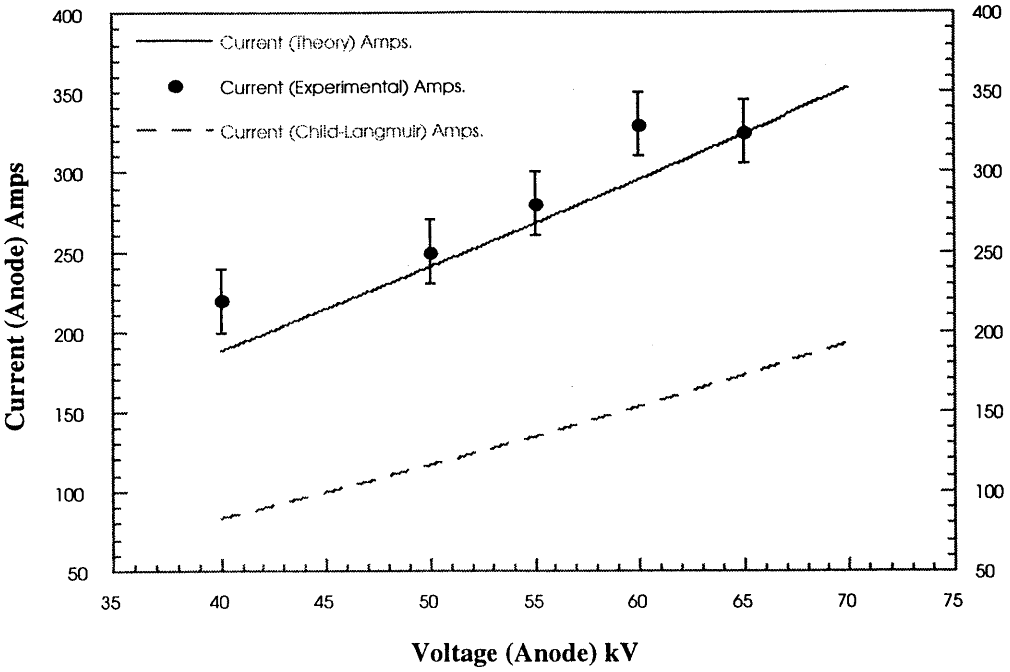

Figure 3.5: V-I characteristics of the planar ferroelectric gun. Impedance ~200 ohms.

3.2.2 Annular beam experiment

The annular beam experiment was conducted using a 12.2 cm diameter, 1.5 mm thick, APC-851 ferroelectric disk (made by American Piezo Ceramics [49]). The annular emitting strip (on the 12.2 cm diameter disk) was centered at a diameter of 11.4 cm and had a width of 2.5 mm. Thus, the total emitting area was about 8.95 cm^2. The emitting side was patterned with a honeycomb silver pattern. The open areas of the honeycombs were of diameter 200 μm and had a closely packed structure with a total open area of about 40%. The capacitance of the ferroelectric cathode was measured to be 40 nF. The ferroelectric was poled and had a dielectric constant of 2200 [49]. The cathode and emitter shape were optimized using the code EGUN [17], to produce a high quality electron beam for possible use in a 1 MW Gyrotron experiment. One should also note the novelty of this Gyrotron gun is that it uses a flat cathode, as opposed to the usual Magnetron Injection Guns (MIG) which use an emitting strip at an angle with the magnetic axis (see figure 2.1). The EGUN design was made with an effort to keep the velocity spread to a few percent, to keep the electric field strength below 50 kV/cm, and to get a transverse to parallel velocity ratio (of the electron beam) of about 1.6. This had to be done while maintaining a flat cathode shape, and was designed as shown in Figure 3.6. The vertical lines in this figure are lines of constant potential while the thick wavy horizontal line is the electron beam emanating from the cathode. The magnetic field is shown increasing across the gun from 0.13 T to 0.25 T.

The mechanical setup of the gun is shown in Figure 3.7. Care had to be taken in holding the ferroelectric firmly but without any stresses, which would crack the disk. This was done by using spring plungers, which were etched to weaken them, and gold contacts to provide a mechanically soft but an electrically strong contact. This ended up being an important lesson that we learnt regarding the fragility of such large ferroelectric cathode, and how important it is to provide the right contact for them. The anode-cathode distance was 2.16 cm. The electrical circuit used to apply a pulse across the ferroelectric consisted of a pulse forming network, a Thyratron switch, and a 3:1 iron-core isolation transformer.

The entire gun was supported on a stand made of an insulating material (G-10). A port on the gun side was added later where we put a flange with a quartz window in order to try and observe any plasma, if possible. We did not observe any such plasma, due to the low pressure inside the gun and because the cathode material was in the ferroelectric phase and not the paralectric phase, which is a known effect [21,31].

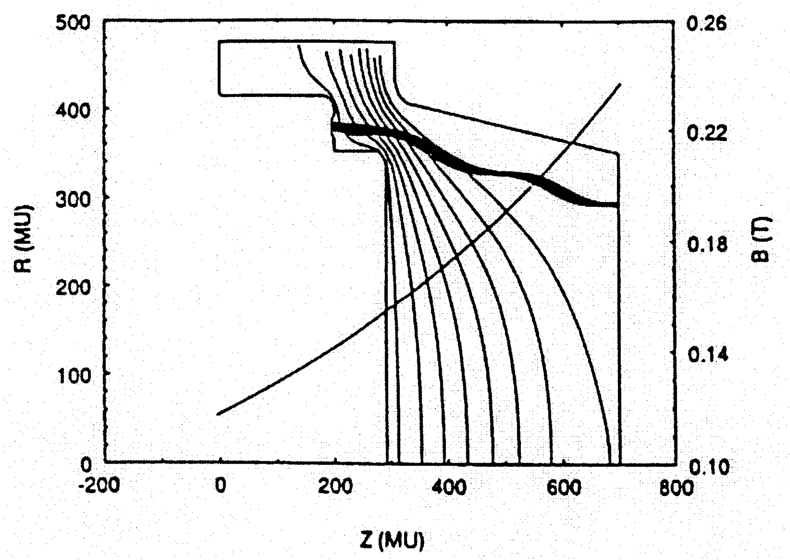

Figure 3.6: EGUN design of the annular ferroelectric gun at MIT. The velocity spread (at the cavity injection point) is 6.9 %, and the transverse to parallel velocity ratio is 1.6.

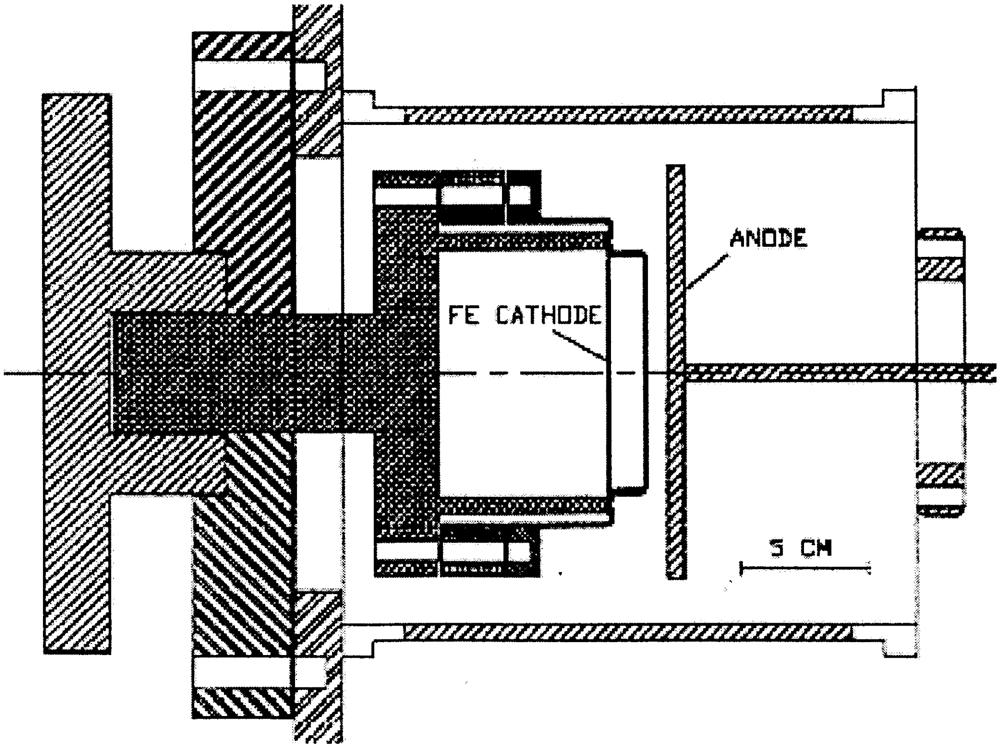

Figure 3.7: AutoCAD drawing of the mechanical setup used to test the annular ferroelectric gun at MIT.

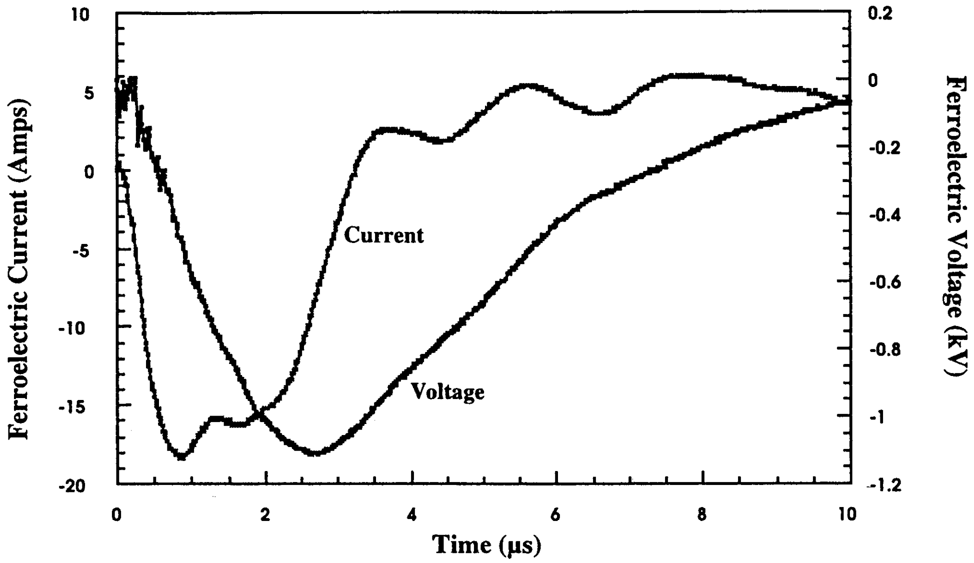

Figure 3.8 (a): Pulse applied across the MIT annular ferroelectric cathode to excite emission - V_{fe}, I_{fe} are the voltage and current of the pulse across the ferroelectric.

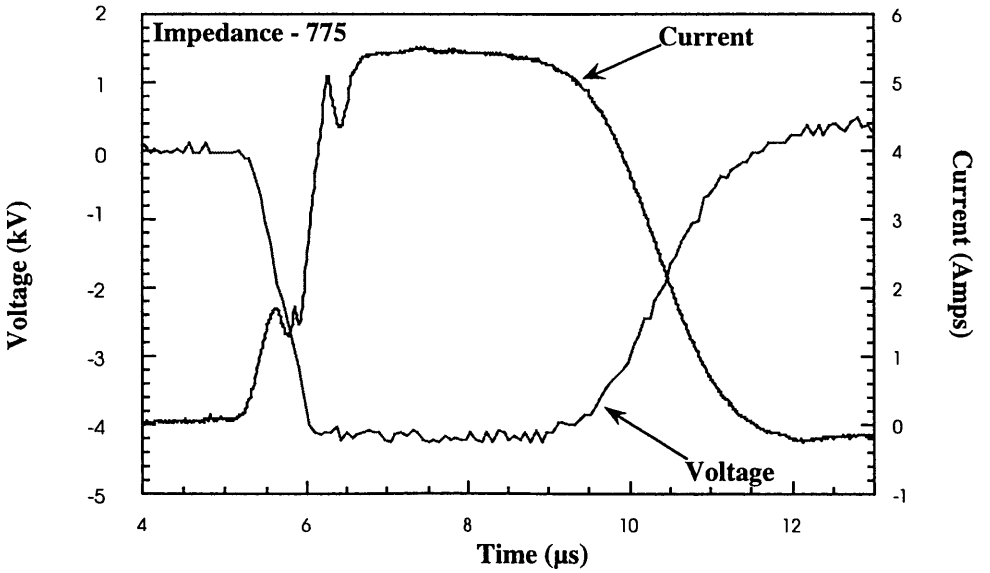

Figure 3.8 (b): Emitted current reaching the anode and acceleration voltage - I_{ak}, V_{ak} (bottom). The delay in this case is ~5 μs (from Figure 3.8 (a) above).

The pulse applied across the ferroelectric (V_{fe}, I_{fe}) was usually in the range of 1.1 - 1.8 kV, 20 Amps. The accelerating voltage applied across the anode- cathode gap (V_{ak}) was in the range of 0 - 15 kV. For testing the gun, we used a simple aluminum plate as the anode. The plate has a diameter of 16.5 cm, a thickness of 8 mm and the plate was maintained 2.16 cm from the emitting ferroelectric surface.

This whole diode was then held inside a 21.3 cm diameter, 22.8 cm long ceramic (MACOR) cylinder with metal flanges brazed on both the ends. The anode plate was grounded, and the cathode had the negative high voltage. The V_{fe} was applied to the ferroelectric through an isolation transformer. The base pressure was 2×10^{-7} Torr.

Using this setup, experiments were carried out with typical pulses applied across the ferroelectric (V_{fe}, I_{fe}) shown in Figure 3.8 (top). The anode-cathode accelerating voltage applied (V_{ak}) and the emitted current (I_{ak}) are shown in Figure 3.8 (bottom). Note that the two traces are plotted on the same time scale, and thus the delay of emission in this case is ~5 μs. The emission delay is the measured delay in time between the application of the switching pulse across the ferroelectric cathode and the observation of current at the anode. The V-I characteristic curve for this diode gun was measured over several shots and is shown in Figure 3.9. The gap impedance from this curve was estimated to be 600-800 Ω.

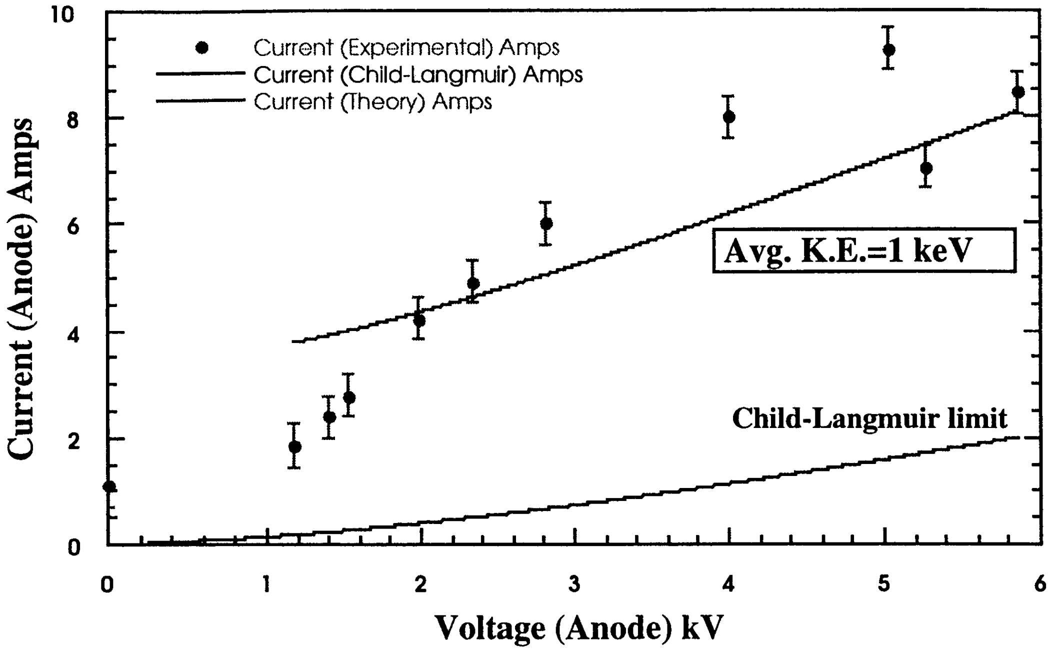

Figure 3.9: V-I characteristics of the annular ferroelectric gun at MIT. The diode impedance can be estimated as 600-800 Ω.

3.3 Microwave generation from ferroelectrics

Collaborative experiments were conducted at Tel-Aviv University [41], which used a ferroelectric cathode to generate microwave power. The interaction was of the ferroelectric electron beam in a cyclotron-resonance maser (CRM). The CRM oscillator operated at ~ 7 GHz, near the cut-off frequency of a hollow cylindrical cavity. The cathode itself was a PLZT (Lead-Zirconium-Titanate) ferroelectric with a high dielectric constant of 4000.

The schematic of the experimental setup is shown in Figure 3.10 below. The experiment consisted of a cylindrical cavity of length 60 cm, and diameter of 2.6 cm. One end of the cavity was formed by the grid on the ferroelectric cathodes emitting surface and the other end was formed by a partial RF mirror.

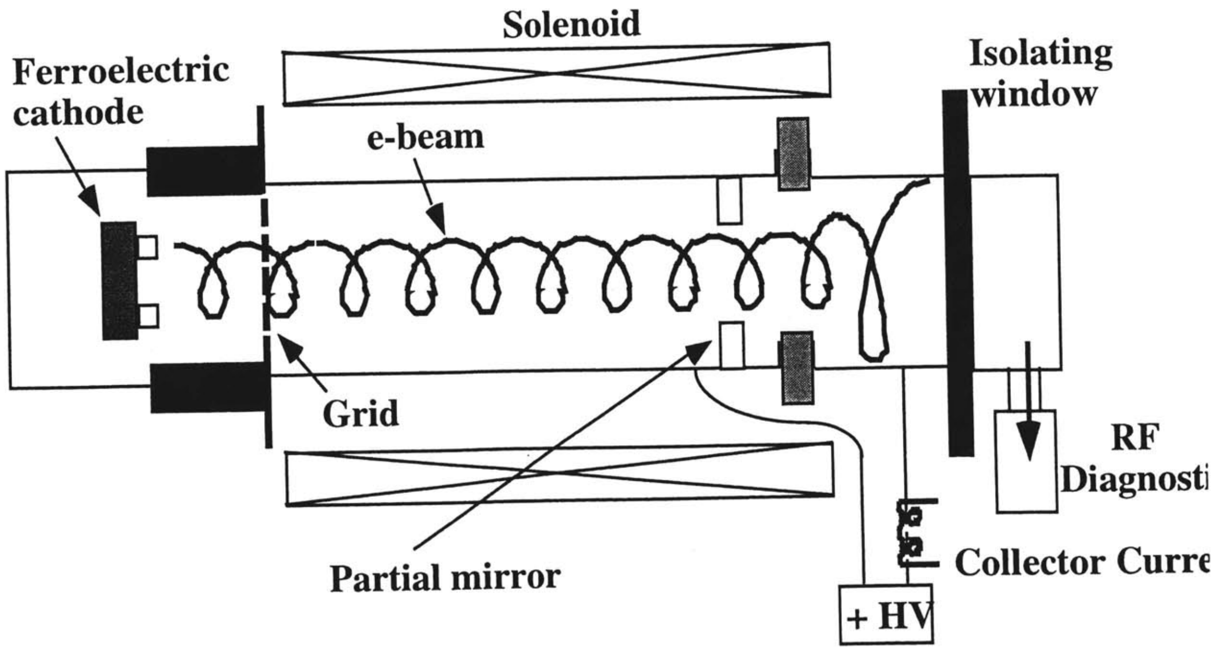

Figure 3.10: Schematic of experimental setup for the ferroelectric microwave experiment.

Accelerating voltages between the anode-cathode gap of 2.5 cm were up to 9 kV. The RF partial mirror consisted of a disc with a hole to let the electron beam through and to permit coupling of the electron beam. The electron beam was then collected at a collector where current was measured by an external Rogowskii coil.

The typical traces for the collector current and the microwave output signal are shown in Figure 3.11 and Figure 3.12. The collector current was up to 0.4 A with a pulsewidth of ~ 1 μs, while the RF output power exceeded 25 W when the electron beam was accelerated to 9 kV. Typical efficiencies were ~ 1%. Figure 3.13 shows the RF output power versus frequency.

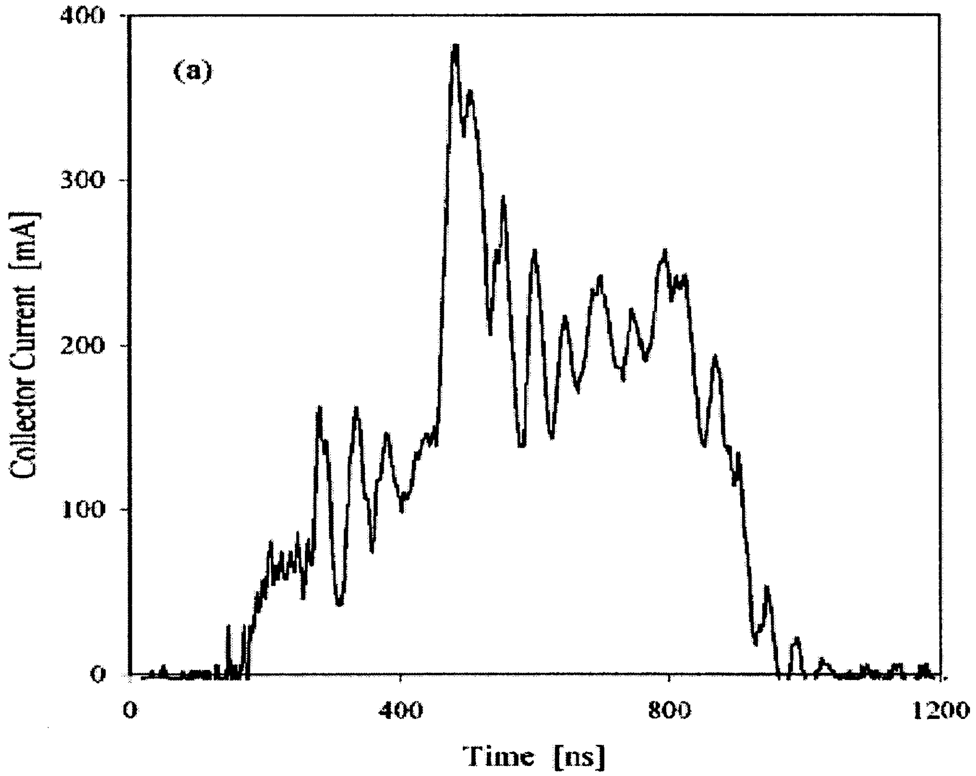

Figure 3.11: Collector current (generated from ferroelectric cathode)

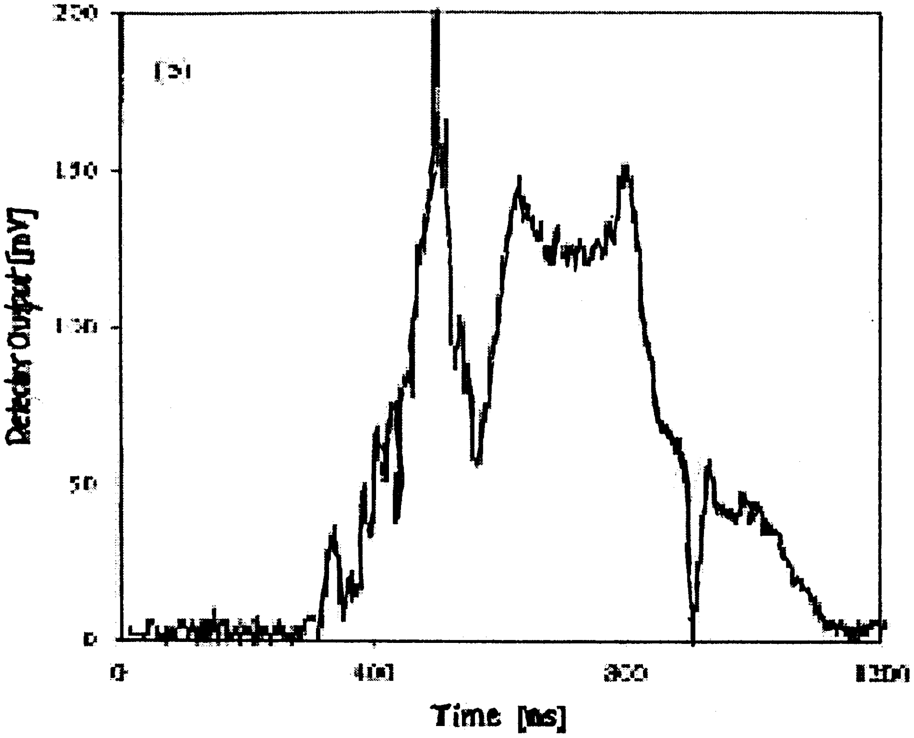

Figure 3.12: Typical RF output trace measured.

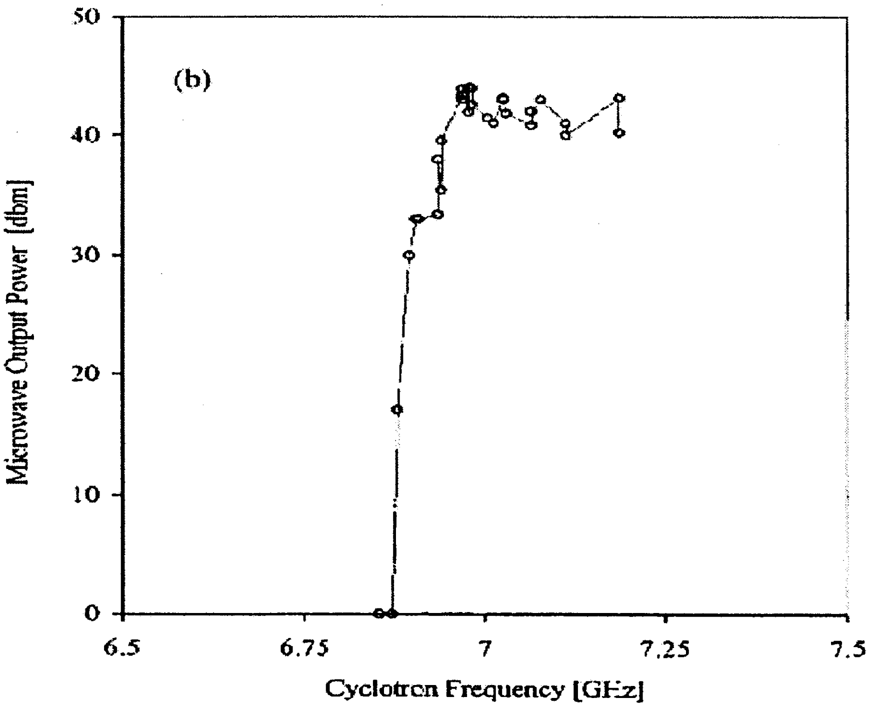

Figure 3.13: RF output power vs. frequency.

3.4 Ferroelectric emission characteristics

Understanding the ferroectric cathodes emission process has been one of the ongoing goals of the ferroelectric program at MIT. Theoretical studies have been done using results obtained from several experiments conducted at MIT, and during a collaboration with Tel-Aviv University, as well as results reported in literature.

The two explanations of the emission from ferroelectrics surround either a polarization switching effect initiated by a pulse across the ferroelectric causing electrons to be emitted from the surface layer; or electron emission caused by a plasma layer which is formed on the surface of the ferroelectric when it is switched. We proposed that it did not have to be either the first one or the second, but that different effects were dominant in different phases of the ferroelectric emission. Hence, we investigated two major effects governing ferroelectric emission. Experiments were done to demonstrate that the electrons emitted from the ferroelectric cathode surface had a (i) *initial energy,* and a (ii) *surface plasma* on the ferroelectric cathode surface. Both these effects cause the Child-Langmuir limit to be exceeded. Both the effects are dependent on the phase of the ferroelectric material being used, and are dominant at different times after the ferroelectric cathode has been pulsed. Using a modified Child-Langmuir relation, we found that by including the initial (kinetic) energy of electrons, one observes good agreement with experimental data. The initial energy of the emitted electrons is taken as a gaussian distribution with an average value of 1.4 - 2.25 keV, which is consistent with experimentally observed values. Furthermore, the effect of a low density plasma on the ferroelectric surface is also investigated, the plasma density is found to be of order 10^{10}-10^{12} cm^{-3}. With these effects one can explain exceeding the traditional Child-Langmuir limit, having a non-zero current at zero accelerating potential across the diode gap, and a host of other experimental observations which have been made using ferroelectric cathodes (further explained in section 3.4.4). Thus, our explanation of the ferroelectric cathode emission process proposes that there are two dominant effects governing ferroelectric emission:

I. Initial energy of emitted electrons.

II. Low density plasma on the ferroelectric cathode surface.

3.4.1 Initial Energy Effects

The traditional explanation for electrically stimulated ferroelectric electron emission has been that when a pulse is applied across the polarized ferroelectric, the polarization of the ferroelectric is switched creating uncompensated charge on the surface. This charge is then ejected in the form of an energetic electron beam. Although this argument is roughly correct, it does not specify the origin of the electrons and cannot explain the different time delays observed in electron emission in all the experiments [21-31, 42-46] (including Figure 3.4). Also it does not quantify any parameters which could be measured and checked directly against experimental observations.

(i) Direct experimental verification of electron distribution

To verify the estimates of the previous section, the distribution function of the energies of the electrons from the ferroelectric surface has been directly measured using a retarding potential [31]. The experimental setup of this is shown in Figure 3.14. The ferroelectric crystal used was PLZT 12/65/35. The rear contact was grounded and the front (emitting) side was connected to the trigger through a ring electrode with a fine mesh on it. The trigger provided was negative and between 1.5 – 2.2 kV, with a pulse width of 150 ns. An intermediate grid was placed 3mm from the cathode and was used for either electron acceleration (with a positive voltage) or electron retardation (with a negative voltage). This grid voltage was varied between 0 kV and –3 kV. The Collimated Faraday Cup (CFC) was placed 2 cm from the cathode and its grid was grounded. The CFC eliminates the influence of the faraday cups bias potential when measuring electrons. The faraday cup was bias voltage varied from –2.5 kV to 2.5 kV. The DC axial magnetic field used was ~500 G.

For the experiment to obtain the initial energy distribution of the electron beam emitted from the ferroelectric cathode. The collector was biased at +50 V to prevent secondary electron emission. The emitted charge was measured against increasing retarding potential. The plot obtained was then differentiated to give a distribution function of energies of the electrons with a gaussian-like profile of average energy ~1.6 keV, as shown in Figure 3.15.

Although this experiment was collaboratively performed at Tel-Aviv University [31], this result has also been observed at CERN [30] where the observed average energies were of order ~2.5 keV (different ferroelectric material in a different material phase from the 1.6 keV data). Thus, in either case one can see that an estimate of a few keV of electron energies with a gaussian distribution has been observed.

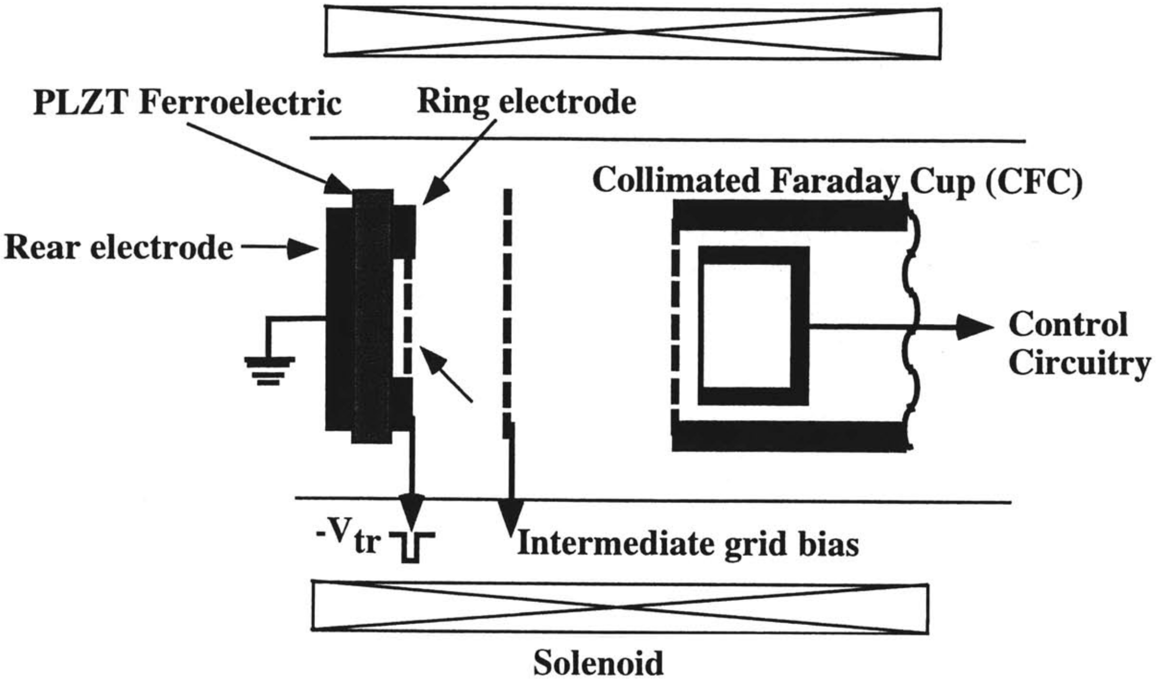

Figure 3.14: Schematic of the experimental setup used to measure the ferroelectric electron beam initial energy distribution.

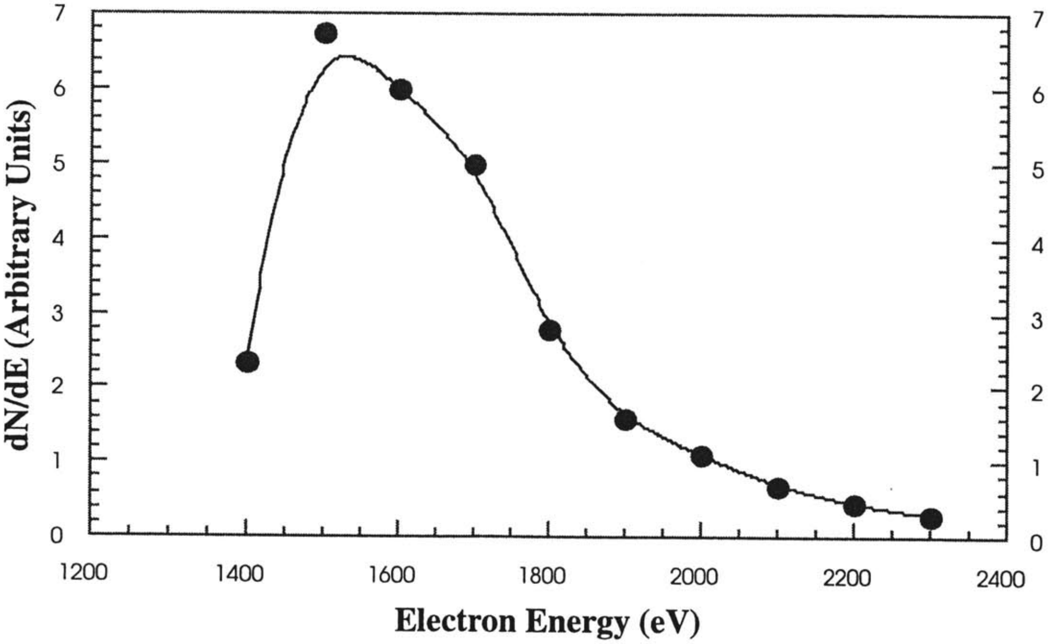

Figure 3.15: Measured electron energy spectrum from ferroelectric cathode. Maximum trigger voltage was –1800 V.

(ii) Modified Child-Langmuir law

Using the initial energy estimates of a few keV, and a gaussian profile for the electron energies, we can proceed with the recalculation of a modified Child-Langmuir law to estimate the enhanced current that one can predict for this non-zero initial energy case. The additional parameter is the *average value* of the kinetic energy that the electrons are born with. This calculation was performed in Langmuir's [50] and Liu's [51] papers, where the Poisson's equation was solved using a gaussian distribution function to obtain the modified Child-Langmuir current density as:

$$J_i = \left(\frac{4\varepsilon_o}{9}\right)\sqrt{\frac{2e}{m_e}}\,\frac{(V-\Phi_m)^{3/2}}{d^2(1-\lambda_m)^2}\left(1+\frac{2.66}{\sqrt{\eta}}\right) \qquad (3.1)$$

where *V=anode-cathode voltage,* v_o *= initial velocity*, and *d = anode-cathode gap* (and the enhanced current density is a function of the three parameters shown below in Eq.3.2 alone).

$$\lambda_m = -\frac{1}{\left(1+\frac{2eV}{m_e v_o^2}\right)^{3/4}-1}; \quad \Phi_m = -\frac{m_e v_o^2}{2e}; \qquad \eta = \frac{2e(V-\Phi_m)}{m_e v_o^2} \qquad (3.2)$$

3.4.2 Surface plasma effect

The formation of a low density plasma on the ferroelectric cathode surface has been recently verified by experimental measurements [21,31] measuring a surface plasma density of ~ 10^{10}-10^{12} cm^{-3} with a temperature of ~ 1 eV. One of the mechanisms by which this plasma could be formed is the breakdown of the adsorbed gasses on the ferroelectric cathode surface (with 0.01-0.1 eV binding energy) by priming electrons generated at the vacuum-metal-dielectric boundary. Surface flashover physics literature estimates the initial ionization to take place within a thin layer of desorbed gas, which is in a layer extending 1-5 μm from the surface [61]. If one utilizes the plasma density of the order $10^{12}\,\mathrm{cm}^{-3}$ and a temperature of 1 eV, one gets the Debye length of over ~ 5 μm. Thus, one can see that the surface plasma is penetrated by the uncompensated charge fields causing the electrons to be accelerated in one direction (towards the anode) and the ions in the opposite direction (shown in Figure 3.16 below). Experimental evidence of the energetic electrons [31] being emitted away from the cathode and ions being accelerated (and getting embedded) into the cathode ferroelectric material [57] on the other side has been established. One must note that this argument requires a collisionless process for the electrons and ions in the plasma, for the electrons and ions to be accelerated by the field without losing energy to collisions. This can be verified by checking that $\nu t \ll 1$ where ν is the collision frequency (electron-electron, electron-ion, electron-neutral) and t is the transit time.

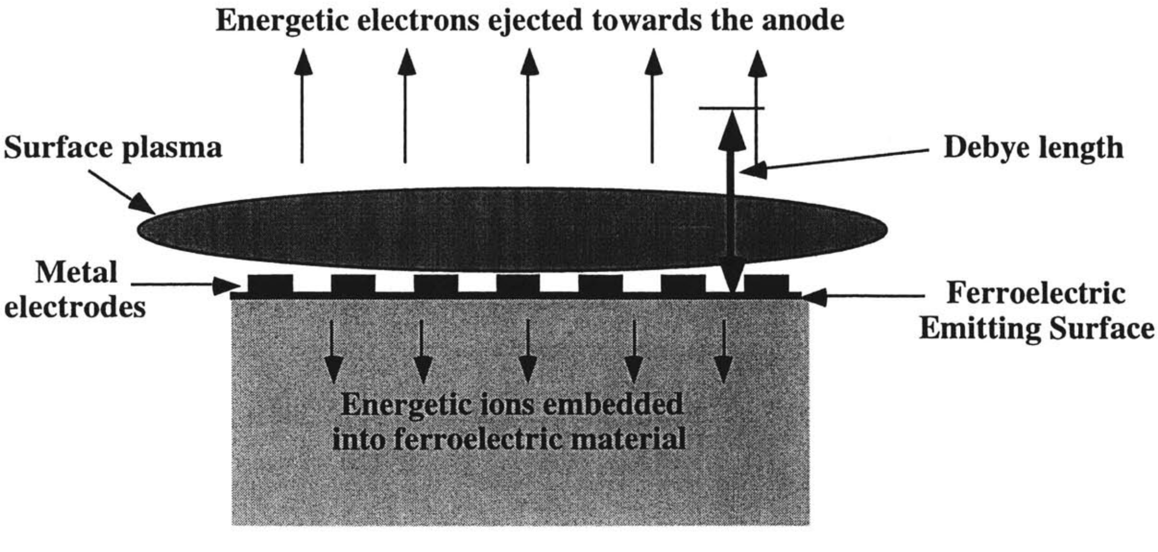

Figure 3.16: Emission process with surface plasma and energetic electrons.

(i) Experimental verification of Surface Plasma

If we carefully examine the trace in Figure 3.3, we see that the accelerating voltage has a negative swing (repelling potential), and during this part of the trace we observe a ion current of ~125A. Using this as the ion saturation current and the relation of j = *env* (where j is ion current density, *n* is plasma density, and *v* is ion velocity), we find that for 78.5 cm^2, and non-relativistic v = 2.17×10^8 cm/s (for 25 kV, 1 a.m.u.); the plasma density can be estimated. When this is weighted by the ratio of the total charge in the ferroelectric switching circuit to the total charge emitted Q_{sw}/Q_e to account for the two parallel circuits [details in Ref. 46], we get the value of the plasma density on the surface as 2.71×10^{12} cm^{-3}. This is slightly higher than the density estimate by Rosenman *et al* [46] by a same technique of 10^{12} cm^{-3}. Besides this evidence, a dull flash has been observed in several ferroelectric cathode experiments [21,24], which is representative of a plasma on the surface of the ferroelectric. Damage observed on the ferroelectric surface after several thousand shots and lack of reproducibility of emission pulses during the initial few thousand shots are all indicators of a surface plasma.

(ii) Parameters of the plasma

A summary of typical plasma parameters measured for ferroelectric cathodes would be:

Surface plasma density ~ 10^{10}-10^{12} cm^{-3} (Tel-Aviv Univ. [46], IAP [22])

Plasma expansion velocity:

Across the surface ~ 1-2 $\times 10^6$ cm/s (Tel-Aviv Univ. [46], IAP [22])

Into the diode ~ 2-6 $\times 10^6$ cm/s (Tel-Aviv Univ. [21])

3.4.3 Discussion of ferroelectric emission process

(i) Emission process

The emission process from ferroelectrics can be explained in terms of the pulse across the ferroelectric causing a partial polarization switching. This creates in turn a bounded uncompensated charge. A small initial priming emission (of the order of a few nano or micro amperes) created by this uncompensated charge at the metal-dielectric-vacuum boundary is what creates a surface plasma [46] (literature does show that priming emission even in the nanoamp range is sufficient to initiate a surface flashover [59-61]). The plasma layer enlarges as the voltage rises and is able to spread across the surface in a time period of ~ 1.33 x Risetime of pulse across ferroelectric. The thin plasma layer of 1-5 μm is formed across the surface, which is less than the Debye length. Hence, the uncompensated charge creates a field, which penetrates the plasma on the surface. This influences the electrons in the plasma, accelerating them towards the anode with an initial energy (which has been measured) [31]; and the ions in the plasma, which are also accelerated in the opposite direction to be embedded in the cathode material (which has also been verified [57]).

The surface plasma is also involved in the dynamic compensation of the switched charge. The bounded uncompensated charge distribution is long lived in comparison to the plasma on the surface which exists for a shorter time period $R \times v$, where R is the radius of the cathode and v is the velocity of the surface plasma on the surface (estimated to be 1-3 cm/μs in the next section). Also note that the uncompensated charge is a function of time and has a dynamic process of compensation associated with it, which includes the creation of uncompensated charge due to domain switching and reduction due to the ions. At longer delay times we see increased emission, which may be attributed to an increased emission area on the cathode surface, which in turn means that the area estimated for non-optimum delays would be smaller and the initial energy larger. The exact initial energy, the energy distribution, and the spatial profile of energies on various points of the cathode surface is dependent on the local uncompensated charge distribution on the surface, and the degree to which the ferroelectric is switched. Therefore, we have taken a average value of a few keV and a gaussian to simplify the calculation and because similar distributions have been experimentally measured (Figure 3.15).

A point to note that the actual emission from the ferroelectric may be just a few nano or micro amperes but it creates the surface plasma from which the many tens of amperes per sq. cm can be obtained. Also, the uncompensated charge gives the plasma electrons an initial energy and thus an inherent directionality, which causes the beam generated to have better brightness and emittance characteristics than one usually expects from plasma cathodes. Although the numbers stated in this paper (for initial energy, plasma density, current density, delay) would probably vary with respect to ferroelectric material, the exact geometry of the diode configuration, temperature, and the phase of the ferroelectric being used; they are representative of most of the ferroelectric experiments carried out to date.

(ii) Application to experimental V-I curves

Application of the modified Child-Langmuir expression to the experimental data is shown in Figure 3.16. The IAP experiment was conducted using a 10.2 cm diameter ferroelectric cathode. In this experiment the anode-cathode distance was 4 cm and the total emitting area was 78.5 cm^2. Figure 3.15 shows the modified Child-Langmuir (Theory curve), the traditional Child-Langmuir curves, and the experiment data points.

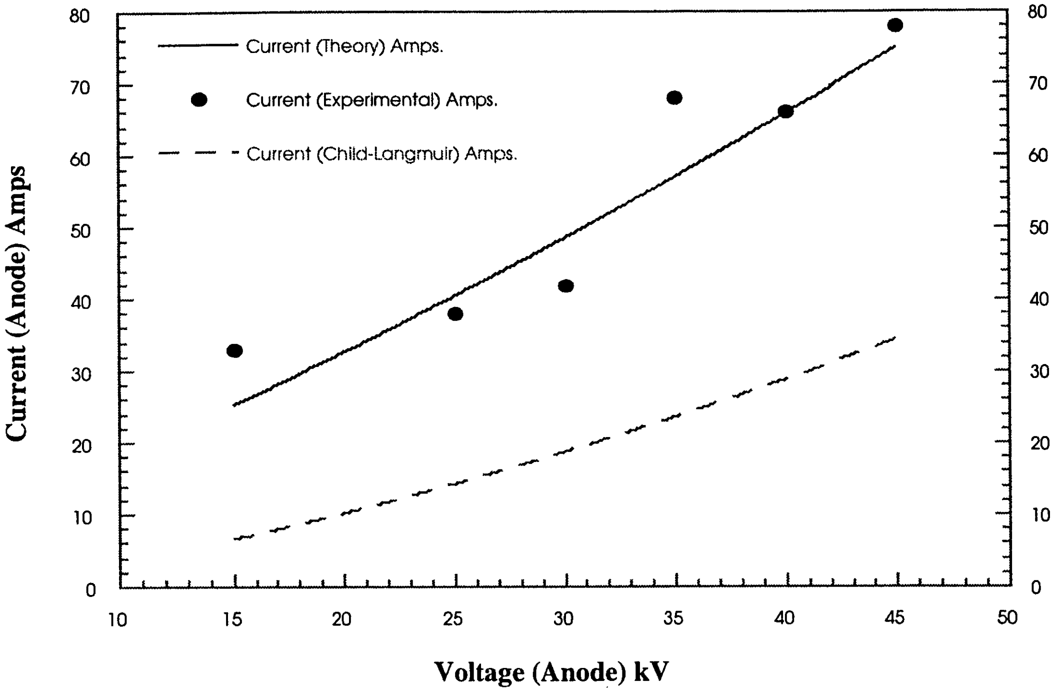

Figure 3.17: Experimental, Child-Langmuir, and theoretical V-I curves for IAP results (Theory curve are fitted to the modified initial energy equations, with an average energy of 2.25 keV).

The theory curve shown in Figure 3.9 was fitted to an average energy of 1 keV. Thus, one can see that the initial energy spectrum that one can measure experimentally is in agreement with the one required to explain the current from ferroelectrics being many times greater that the traditional Child-Langmuir limit. The question that remains is the source of the electrons forming the beam and the interaction between these energetic electrons and the surface plasma, which is discussed next.

(iii) Delay characteristics

Another experimentally observed effect in ferroelectric cathodes is that the emitted current is observed after a finite delay after the pulse across the ferroelectric. This effect has been further experimentally investigated, and results from our experiments and various sources in literature show a linear relationship between the risetime of the pulse across the ferroelectric and the delay observed. As one sees in Figure 3.3 and Figure 3.8 the relation is that the emitted current is observed a short time after the peak of the voltage pulse applied across the ferroelectric (Delay ~ 1.33 × Risetime). This is consistent with flashover occurring at the peak voltage (especially when the ferroelectric is being operated near its threshold voltage for emission, as it is in most ferroelectric experiments). Once the plasma is created, it then propagates across the ferroelectric cathode surface in a finite expansion time leading to a slight further delay (the additional 0.33, in this case). The exact manner in which this plasma would propagate would be dependent on the surface and the geometry of the diode, ratio of the size of the cathode to the anode-cathode gap distance, as well as other geometrical considerations such as solid or annular beam. In cases when the voltage used is much higher than the threshold voltage (for measurable emission current), then one would expect the breakdown to occur before the voltage pulse across the ferroelectric reaches its peak, and has been seen in Cornell's experiments [24].

Also shown in Figure 3.17 is the linear variation of the minimum delay observed in various experiments as a function of the radius of the cathode used. All the data values are shown in Table 3.1. The reason that this is plotted is that the surface plasma originates at a point/points and then spreads over the surface. In zeroth order, we assume

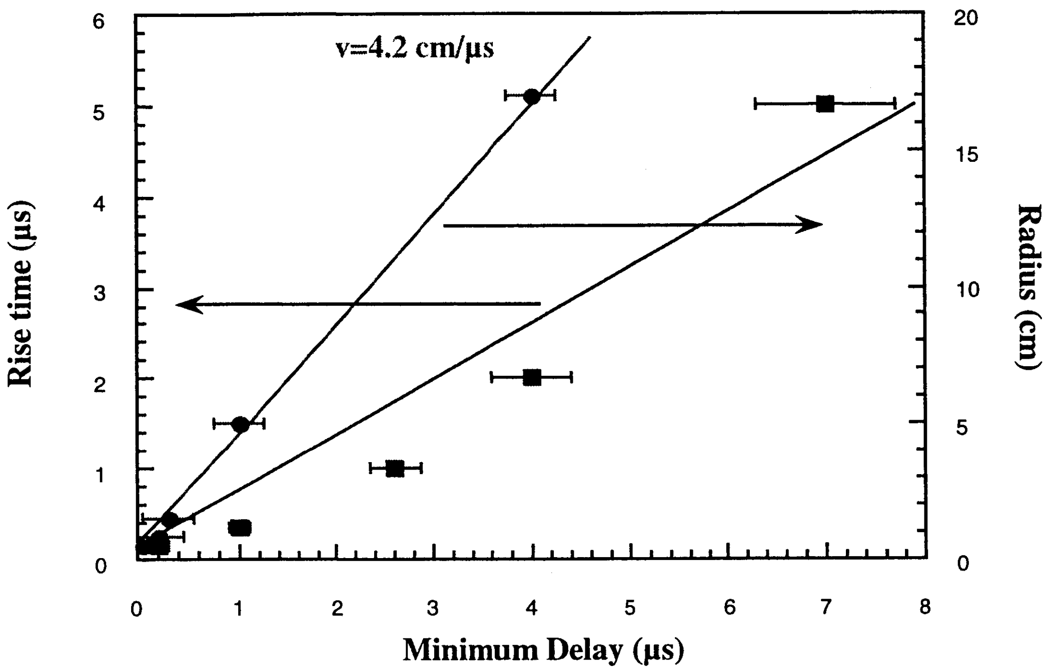

Figure 3.18: Minimum delay of emitted current vs. (i) risetime of pulse applied across the ferroelectric cathode, and (ii) radius of various cathodes (Data in Table 3.1).

that the plasma originates at the center and spreads to the edge, before we see a measurable beam. This gives us an estimate of a plasma velocity across the surface of 4.2 cm/μs. Yet, one must remember that the actual case is probably small microplasma points at various places spreading over the surface (such as shown by Shur *et al* [21]), and this would significantly reduce the plasma expansion velocity across the surface to ~1-2 cm/μs. This is in agreement with plasma expansion velocities [58] observed in other plasma cathode experiments. One can also plot optimum delay (where maximum beam current is obtained) vs. radius of cathode to get comparable results. Also, as the plasma expands over the cathode surface one would expect the measured current to increase initially and then decrease as the plasma formulates on the surface initially and then moves off the surface: this is verified by examining Figure 3.4 and the data from Sampayan *et al* [25].

Minimum Delay (μs)	**Risetime of Pulse across ferroelectric (μs)**	**Radius of cathode (cm)**	**Source of data**
0.05	**0.150**	**-**	**Cornell** [24]
1.0	**0.350**	**-**	**IAP** [22]
2.6	**1.000**	**-**	**MIT (without x-former)**
4.0	**2.000**	**-**	**MIT (with x-former)**
7.0	**5.000**	**-**	**MIT (long pulse)**
0.050	**-**	**0.500**	**Gundel** [55]
0.2	**-**	**0.800**	**Benedek** [43]
0.3	**-**	**1.500**	**Sampayan** [25]
1.0	**-**	**5.000**	**IAP** [22]
4.0	**-**	**16.950**	**MIT**

Table 3.1: Minimum delays, risetime of pulse across ferroelectric, and radii of ferroelectric cathodes from MIT experiments and sources in literature.

(iv) Diode impedance

If one analyzes the diode impedance, the dominant effect that dictates this is the initial energy of the electrons for short pulses and for ferroelectric cathodes in the ferroelectric phase. If long pulses (microseconds) are investigated then plasma expansion becomes an important factor, depending on the diode geometry. Thus, the dominant effect amongst the two is dependent on the amount of polarization switching achieved, the anode-cathode gap distance, and the length of the beam pulse. The greater the polarization switching, the greater is the uncompensated surface charge, leading to higher initial energies. For the plasma effect, we see that the greater the anode-cathode gap, the lower is the effect of gap reduction. Conversely, the lower the switching voltage, the lower is the uncompensated charge and (thus) the initial energy, and the lower is the plasma density [46], and the consequent experimental current is lower due to lower initial energies and lower plasma densities.

(v) Luminosity of surface plasma

Another factor that is observable is the luminosity of the plasma across the surface when a higher density plasma is created across the surface. Lower density plasmas are created when the cathode material used is in the ferroelectric phase. These have low luminosity and may be difficult to observe. On the other hand, when ferroelectric cathodes in the paraelectric phase are used one can see the plasma [56,62]. It can also be said that the plasma expansion velocities will probably be higher for the higher density surface plasmas, and that the lack of luminosity may be an indicator of a weak plasma rather than a lack of emission from a ferroelectric ceramic.

3.4.4 Effects explained by proposed emission process

Thus, the two effects enumerated provide a quantitative basis for further investigation of ferroelectric electron emission. Although the theoretical curves show good agreement with experimental data for average energies in the range of 1 - 2.25 keV (which is within the range of experimentally measured energies), and surface plasma densities of order of ~ 10^{12} cm^{-3} has been experimentally verified. One has to recognize that these estimates will vary during a pulse and across ferroelectrics because of dynamic domain switching and plasma evolution. Nevertheless, initial energy effects and the surface plasma are able to explain:

1. Exceeding the Child-Langmuir limit of current density.
2. Non-zero emission current at zero accelerating voltage and the somewhat linear V-I curves (as compared to the distinct $V^{3/2}$ dependence of the traditional Child-Langmuir).
3. Emittance and brightness comparable to thermionic cathodes, due to the directionality of the electrons born on the cathode surface with an initial energy.
4. Emitted charge, which can exceed bound surface charge, due to the plasma on the ferroelectric cathode's surface.
5. Shot-to-shot inconsistencies (which are frequently observed), as well as some evidence of conditioning - both of which would be typical for a plasma effect on the surface.
6. Experimentally observed energetic electrons with a distribution functions which would be consistent with theoretical analysis, and plasma densities of order ~ 10^{12} cm^{-3}.
7. Delay characteristics being dependent on the risetime of the pulse across the ferroelectric and the radius of the emitter being used, due to the plasma effect.

One can conclude from the experiments described in this chapter that there are several attractive features that have now been proven about ferroelectric cathodes. That being said, there are several other properties such as lifetime of the cathode, poor understanding of the emission process, and several others (application specific), which yet need to be investigated before the widespread adoption of these cathodes in practical settings.

Chapter 4

Coaxial Gyrotron Design

4.1 Introduction

The two most important technical constraints which limit the development of high power gyrotrons are ohmic losses on the cavity walls and the capacity of gyrotron windows to handle megawatts of CW power. Attempts have been made to solve the cavity wall losses problem by increasing the volume/size of the cavity region, but this leads to the choice of higher order modes and hence enhanced mode competition. The second major limitation, which is the availability of microwave windows that are capable of handling megawatts of CW power is also being investigated by several groups. In recent years this limitation has been somewhat alleviated by the introduction of diamond windows [15], dome windows, and other novel window concepts. Hence, the onus is once again on the tube and the cavity to increase the amount of power generated per tube as well as simplify the design of the tube i.e. move toward diode guns instead of the triode guns presently in wide use. One of the promising candidates for this is the diode coaxial gyrotron.

Mode selection has usually been effectively achieved in gyrotrons by placing a thin annular beam at a radius corresponding to the maximum value of the coupling impedance between the beam and the non-symmetric $TE_{m,p}$ mode [1-10] (where m is the azimuthal index number and p is the radial index number). This method is especially effective in selecting whispering gallery modes (m>>p). Thus, the smaller radial index modes are discriminated against because the radii of the electron guiding centers are smaller than the radii of their wave caustic (in the waveguide which makes up the gyrotron), which causes them not to be excited. This places the electron beam in a low coupling region of an exponentially decaying field, making the coupling with these modes quite small. On the other hand, modes with higher radial index numbers are strongly coupled to the electron beam and have lower starting currents. The drawback of whispering gallery modes is that they are concentrated somewhat close to the walls of the cavity, causing the fields to be substantial at the cavity walls as the microwave power levels exceed a megawatt, making the ohmic power losses prohibitively high. As the requirements for power and frequency rise, the operating mode radial index increases and mode selectivity decreases.

Selectivity of modes with large radial indexes can be achieved by a cavity with a coaxial conductor [67]. The presence of a coaxial conductor leads to the deformation of the spectrum of mode eigen-frequencies that rarify the competing modes around the operating mode, if the conductor is chosen properly. Also, the coax radius can be arranged such that it is smaller than the caustic of the operating mode but closer to the caustic radii of the parasitic modes with larger indices. This helps in the further degradation of the competing modes by profiling the shape of the conductor. Finally, the introduction of the coaxial conductor as a ground plane closer to the electron beam helps reduce the voltage depression and corresponding degradation of the electronic efficiency.

This chapter discusses the design of a coaxial gyrotron, which is a tube built and operated within collaboration with Physical Sciences Incorporated (PSI). The tube was designed at PSI under a Small Business Innovative Research grant. PSI also fabricated the initial tube design, while several subsequent changes to the tube were made at MIT. The design is for a 3 MW, 140 GHz gyrotron in the $TE_{21,13}$ mode. A schematic of the gyrotron is shown in Figure 4.1. The figure shows the configuration where the gyrotron was operated with a fixed coaxial conductor and power was extracted axially. (A mechanical drawing of the gyrotron with the mode converter and a single mirror is shown in Figure 4.26).

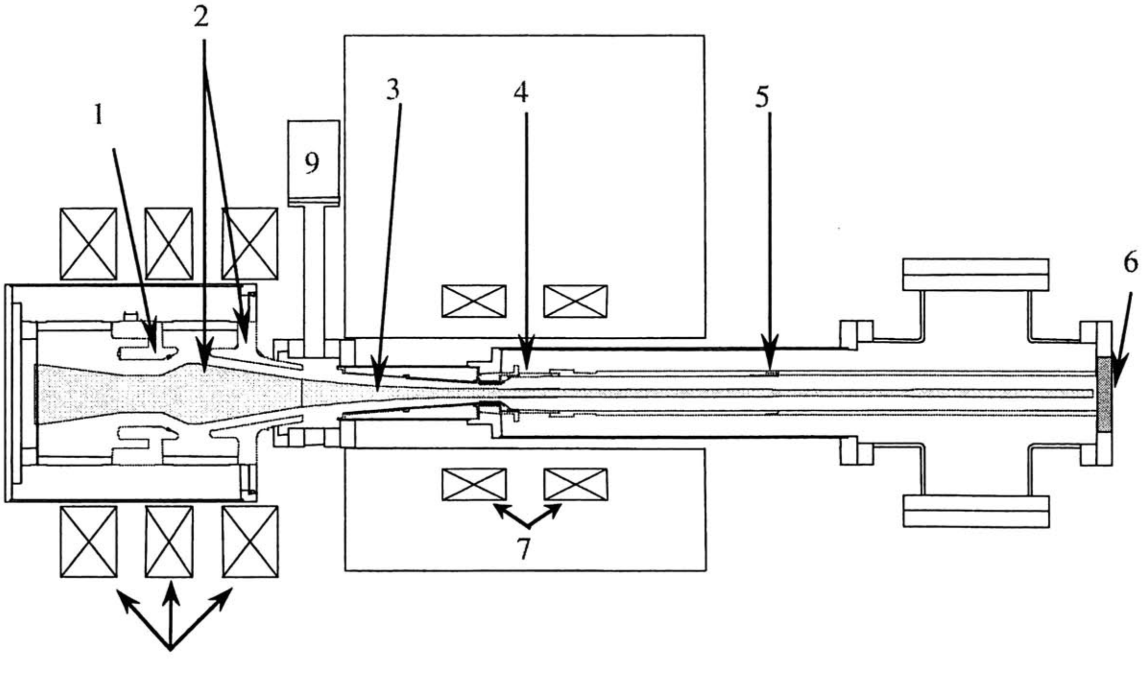

Figure 4.1: Schematic of the 3MW, 140 GHz gyrotron operated at MIT.

1. Cathode 2. Anodes 3. Coaxial Conductor 4.Cavity 5. Collector

6. Window 7. Superconducting Magnet 8. Gun coils 9. Valve

4.2 Gyrotron cavity

The mode in the coaxial gyrotron had to satisfy several constraints. It was selected in a manner that ohmic heating on the inner and outer conductors was within acceptable parameters for CW operation (600 W/cm^2). The outer walls of the cavity were made of copper while the inner coaxial conductor was made from 304 stainless steel. The inner conductor was made of steel instead of copper, as copper is much softer than steel and could have resulted in a sag due to the long length of the inner conductor of ~100 cm. For machining ease several sections were made, all of which were held together with a strength press fit. The cavity section of this tube was designed with a slightly smaller radius than the theoretical value in order for us to be able to make a sleeve which could be slid on and fixed. The advantage of this system was that if at some point if one wanted to change the shape (taper, corrugations, etc.) of the inner conductor then this sleeve would provide the flexibility to do so without having to entirely re-machine one of the coaxial conductor sections. Figure 4.2 below shows a schematic of the cavity with some dimensions.

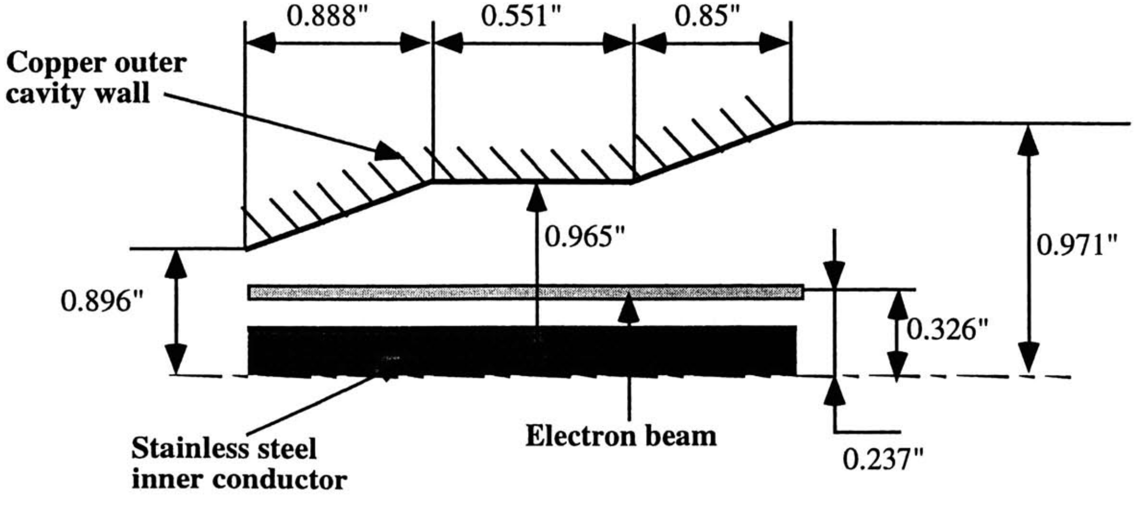

Figure 4.2: Schematic of the cavity section of the coaxial gyrotron.

4.2.1 Cavity Mode

Previous studies [64,68] have shown that the $TE_{m,p}$ with m~p is the most promising for high power coaxial gyrotrons (m,p are azimuthal,radial index). These are the so called 'body' modes which have their fields concentrated away from the cavity walls which reduces the ohmic wall loading (which is a limiting issue in whispering gallery modes with m>>p). Figure 4.3 shows a good graphical representation of how higher radial index (p) modes allow higher powers to be achieved from gyrotron tubes. The modes were chosen such that the peak ohmic heat loading on the outer wall was below $3kW/cm^2$ with an average value of $1.5\ kW/cm^2$. The heating on the inner conductor was kept below $600\ W/cm^2$ by keeping the radius of the conductor small enough. The appropriate design of a 3 MW gyrotron at 140 GHz was made using the expressions in reference [69]. The average density of ohmic power was $1.5\ kW/cm^2$, at the output power level of 3 MW at 140GHz, with a resonator length to wavelength ratio of 8.5, and eigen-number close to 65. There were several modes with roots near the eigen-number of 65, but the $TE_{21,13}$ mode was chosen because of previous Russian results of over 2 MW power [64,68].

Once the mode is selected one can then determine the efficiency of operation at the desired output power level. The effect of the inner conductor on the design mode must be small for this to be a viable option and efficiency can then be calculated neglecting the effects of the inner conductor. This was done using the codes CAVRF and EFF written by Fliflet *et al* [70]. These codes assume a slowly varying axial profile, and no velocity spread is included for this stage. The field and the cavity profile are shown in Figure 4.4. The beam position then was calculated by investigating the coupling impedance as a function of beam radius (shown in Figure 4.5).

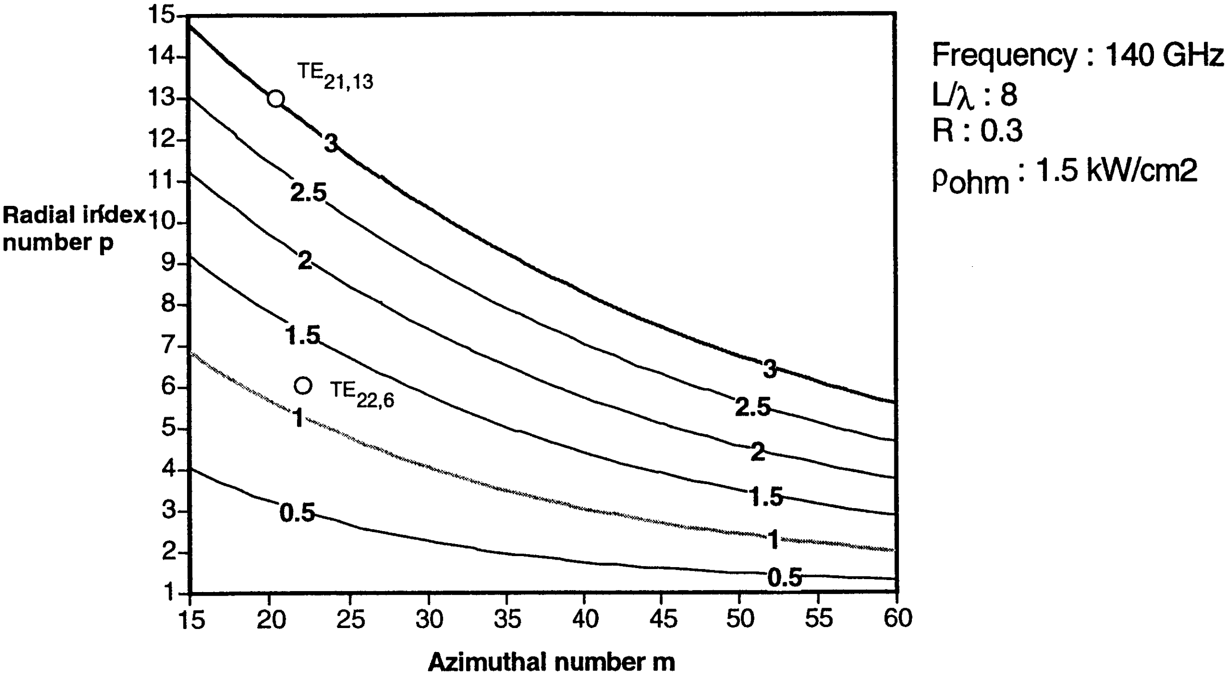

Figure 4.3: Output power vs. waveguide indices at a fixed average ohmic wall loading. The lines indicate the constant power contours. Hence, the 21,13 mode clearly lies on the 3 MW power level.

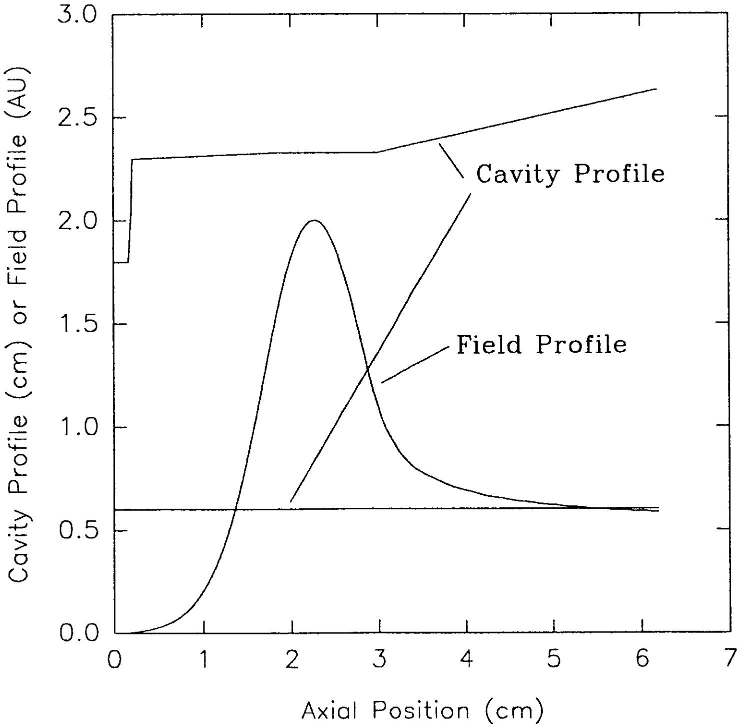

Figure 4.4: Cavity and the RF field profile in the $TE_{21,13}$ mode [11].

The two peaks at r = 7.5 mm and 8.2 mm are for the co-rotating wave (left) and counter wave (right). To reduce mode competition the outer peak mode was chosen, which is shown in Figure 4.6. Figure 4.7 shows the efficiency versus beam current for the case of 95 kV, and a velocity ratio of 1.5. Table 4.1 summarizes the cavity parameters where the back leakage is the power leaking towards the gun and μ and F are the normalized cavity length (normalized to the wavelength at the design frequency) and field strength parameters respectively (normalized to power levels), as defined in [69]. These normalized parameters are important in the comparison of one gyrotron tube to another. They are independent of frequency, power levels, and design variances between tube. Hence, most theory of gyrotron tubes is usually reported in terms of these parameters which makes its applicability to different gyrotrons easier. In fact, in the next chapter this fact is used in analyzing some of the results from this tube.

Q diffraction	1467
l/λ	8.5
Peak ohmic heating	2.8 kW/cm^2
Back leakage to gun	0.06 %
μ, defined in [67]	18.96
F, defined in [67]	0.095

Table 4.1: $TE_{21,13}$ cavity parameters from the single mode code [11].

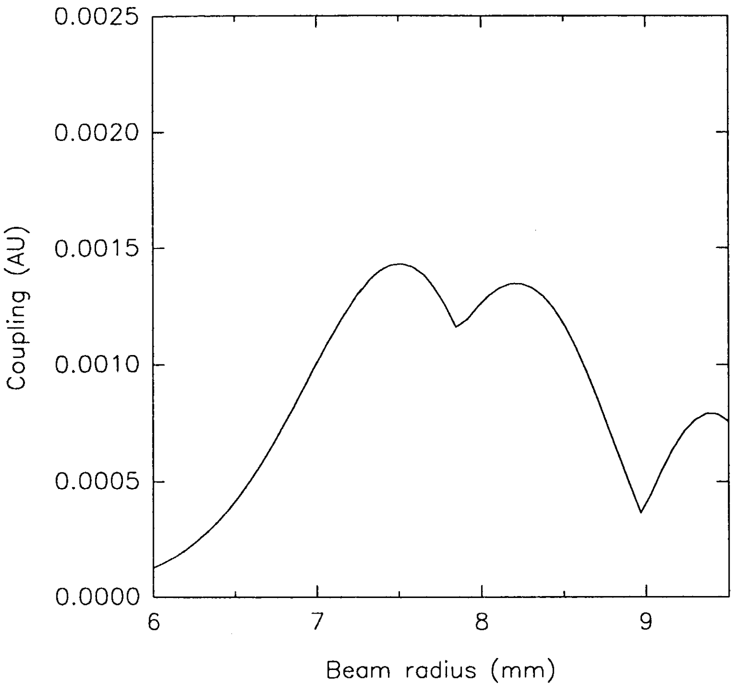

Figure 4.5: Coupling for the $TE_{21,13}$ mode as a function of beam radius [11].

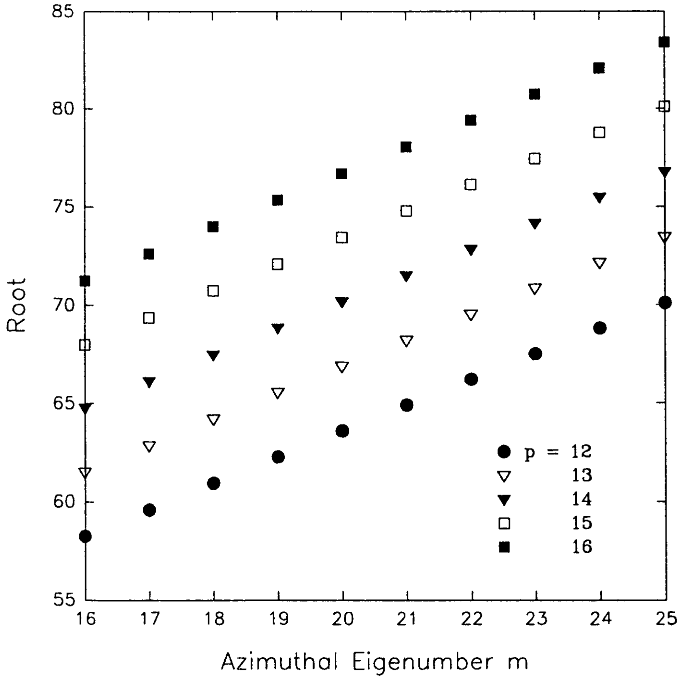

Figure 4.6: Competing modes near the $TE_{21,13}$ mode [11].

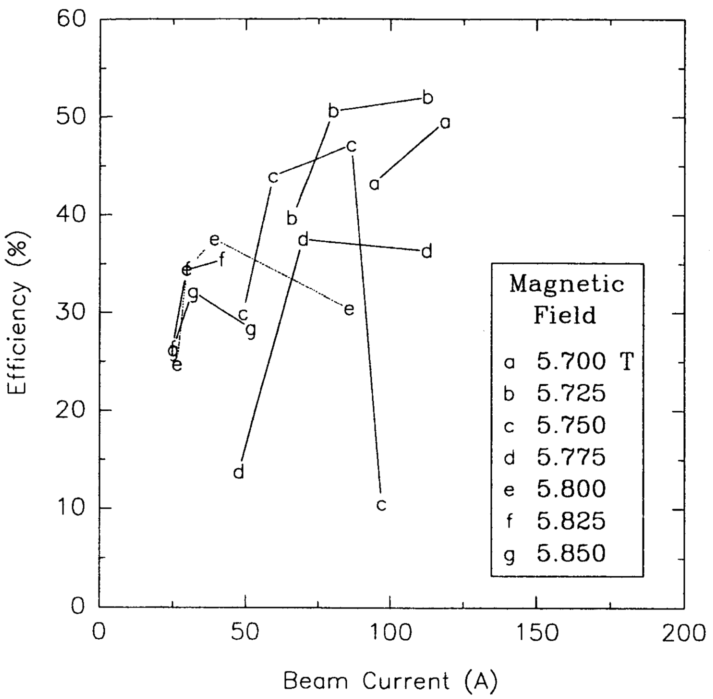

Figure 4.7: Electronic efficiency versus beam current for the $TE_{21,13}$ mode [11].

4.2.2 Mode Competition

Mode competition is a critical issue in the design of any gyrotron and is even more important for the present gyrotron because of the choice of a high radial index mode, m~p. Hence, mode density around the design mode was high and special attention was paid to this issue. Figure 4.6 shows the eigen-number χ ($\chi = k_{mp}r_w$) proportional to the cutoff frequency versus the azimuthal index for the competing modes, where k_{mp} is the transverse wave number and r_w is the waveguide radius. For the chosen beam radius of r = 8.2 mm, not all the modes have a high coupling impedance. For p < 12 , the interaction is weak because the beam is inside the caustic of the mode, and the modes with a high radial index are strongly affected by the inner conductor. Nevertheless, there are several competing modes, and in pulsed operation, the problem is exacerbated due to the different voltages that the are swept through when the voltage is rising up to the operating value of 95 kV [69]. Based on these arguments and those made previously [70] the modes that are good candidates for mode competition are the TE modes: 23,12; 24,12; 20,13; 22,13; 23,13; 18,14; 20,14; 21,14; 22,14; 16,15; and 17,15. The frequencies of these modes normalized to the frequency of the 21,13 mode and the results are plotted versus the inner conductor radius is shown in Figure 4.8.

The Q of a mode is a monotonically increasing function of the product dχ/da and the slope of the taper of the inner conductor [70]. The goal is to perturb the Q of the competing modes without affecting the Q of the design mode. Thus, dχ/da ~ 0 should ideally be chosen for the operating mode. Figure 4.8 shows that the radius that would be

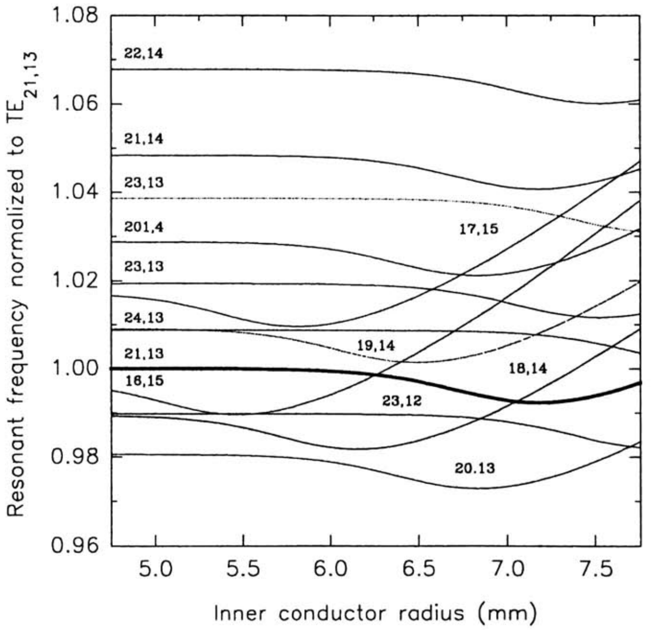

Figure 4.8: Mode roots versus the inner conductor radius for the competing modes in a TE$_{21,13}$ cavity. The roots are normalized to the TE$_{21,13}$ mode without an inner conductor [11].

picked by these criteria would be 7.2 mm, but this would cause unacceptably large ohmic losses on the inner conductor (as seen in Figure 4.9) and thus the radius chosen for the inner conductor was 6.02 mm. At this point the heat load is 600 W/cm^2. Earlier studies have shown that a negative taper of 2° on the inner conductor suppresses the competing modes. The Q's were calculated with CAVRF [68] and are shown figure 4.10. As can be seen from Figure 4.10 certain modes such as $TE_{15,15}$ were greatly reduced while others such as $TE_{19,15}$ were significantly increased.

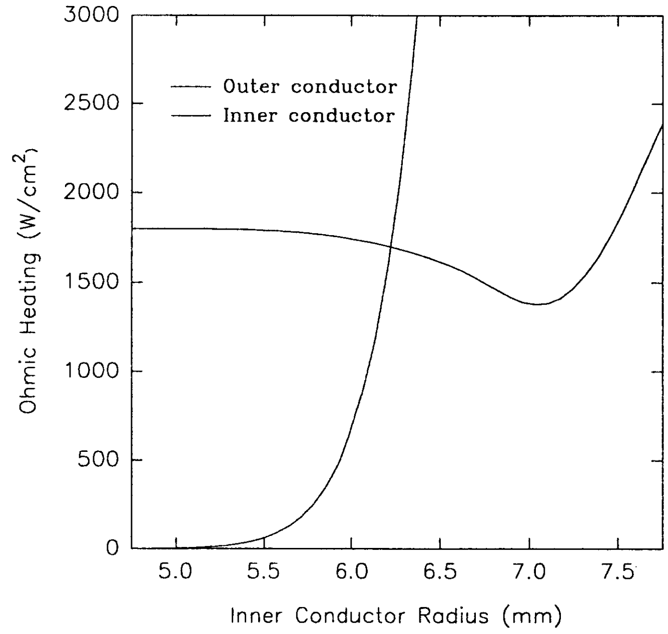

Figure 4.9: Ohmic heating of the inner and outer conductor versus the inner conductor radius – calculated with 1.5 times the conductivity of OFHC copper at 300°C [11].

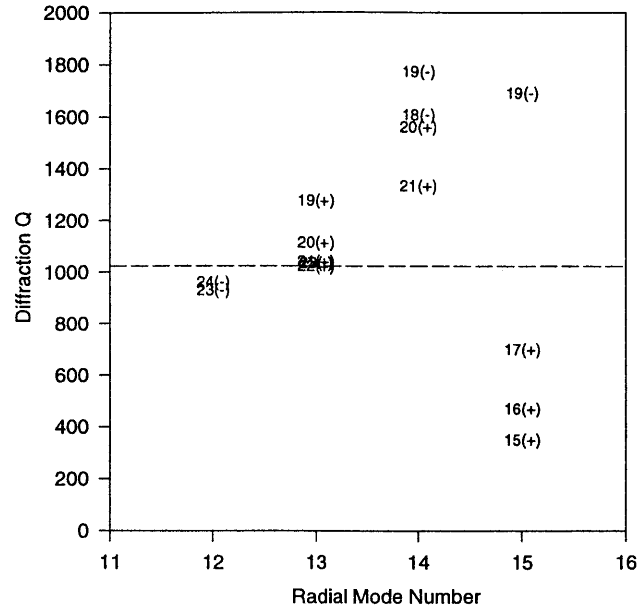

Figure 4.10: Diffractive Q's as a function of radial mode index and azimuthal mode for the case of a 1° taper of the inner coaxial conductor [11]. The '+' and the '-' subscript stand for co-rotating and counter-rotating waves.

Hence, a compromise has to be reached in terms of the radius and the taper of the inner conductor to be used. Figure 4.11 - 4.12 shows the starting currents for the modes of interest with no conductor and an inner conductor with an radius of 6.02 mm. In both the cases the operating voltage was 95 kV. A higher voltage of 105 kV had to be used to achieve stable operation for the tapered (1°) conductor, hence making it unsuitable as a useful operating scenario. The velocity ratio for both cases shown was 1.44. A careful inspection of the two diagrams shows that in the region of the design mode ($TE_{21,13}$) and at the operating current levels (76 Amps) we see fewer modes for the case with the coaxial conductor (Figure 4.12).

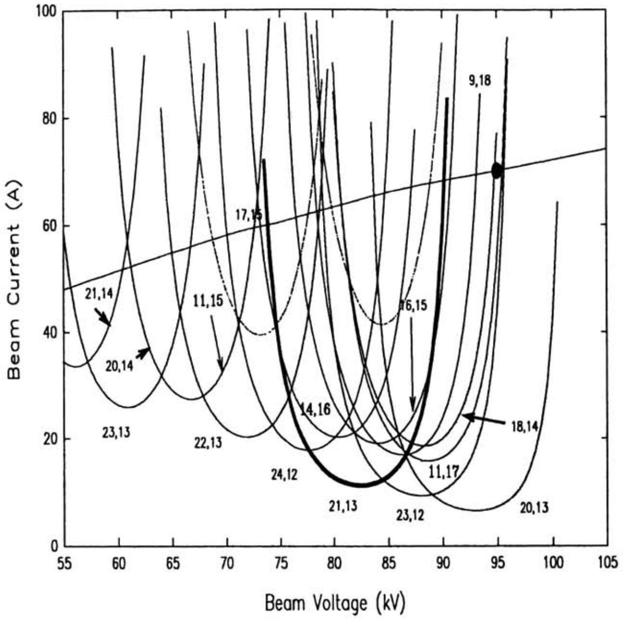

Figure 4.11: Starting current as a function of beam voltage for the case with no inner conductor. The beam load line is also shown [11].

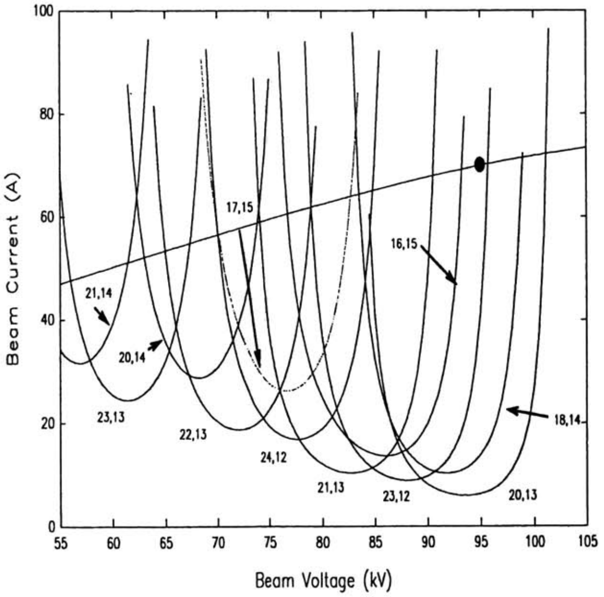

Figure 4.12: Starting current as a function of beam voltage for the case of a 6.02 mm uniform inner conductor (the line is an approximation of the non-linear excitation region) [11].

4.3.2 Multimode code simulations

The multimode performance is modeled by using a code that calculates the growth and saturation amplitudes of a set of modes in a coaxial cavity [71]. The growth is modeled with a series of simulations starting with a low beam voltage, then proceeding in steps to the final voltage. This code differs from the single mode code in that it takes into account the history of the various modes that the tubes cycles through to get to the design mode, with the field levels of previous modes. The beam velocity ratio corresponding to the beam voltage was determined from the beam simulations that are discussed in section 2.3.2. For each voltage step, only those modes which had starting currents less than the operating current were considered, as determined by,

$$I_{beam} = \left(\frac{1}{I_{temp}} + \frac{1}{I_{sc}} \right)^{-1} \qquad (4.1)$$

where I_{temp} and I_{sc} are the temperature and space charge limited diode currents. I_{sc} is proportional to the beam voltage raised to the 3/2 power, with a multiplier determined from simulations [72].

Multimode results from the case without an inner conductor are shown in Figure 4.13. Oscillations start at 65 kV with the appearance of the $TE_{23,13}$ mode. This mode increases in amplitude up to 75 kV and then subsides around 85 kV where the $TE_{14,16}$ mode starts dominating. At 90 kV, the $TE_{23,12}$ takes over along with the $TE_{11,17}$ mode. These modes coexist at 95 kV and electronic efficiency at 95 kV is 37%. (Note that for all the multimode code results shown the amplitude is in arbitrary units and the time is normalized to the decay time of the operating mode). We would like to thank Dr. Nusinovich and Dr. Read for these simulations.

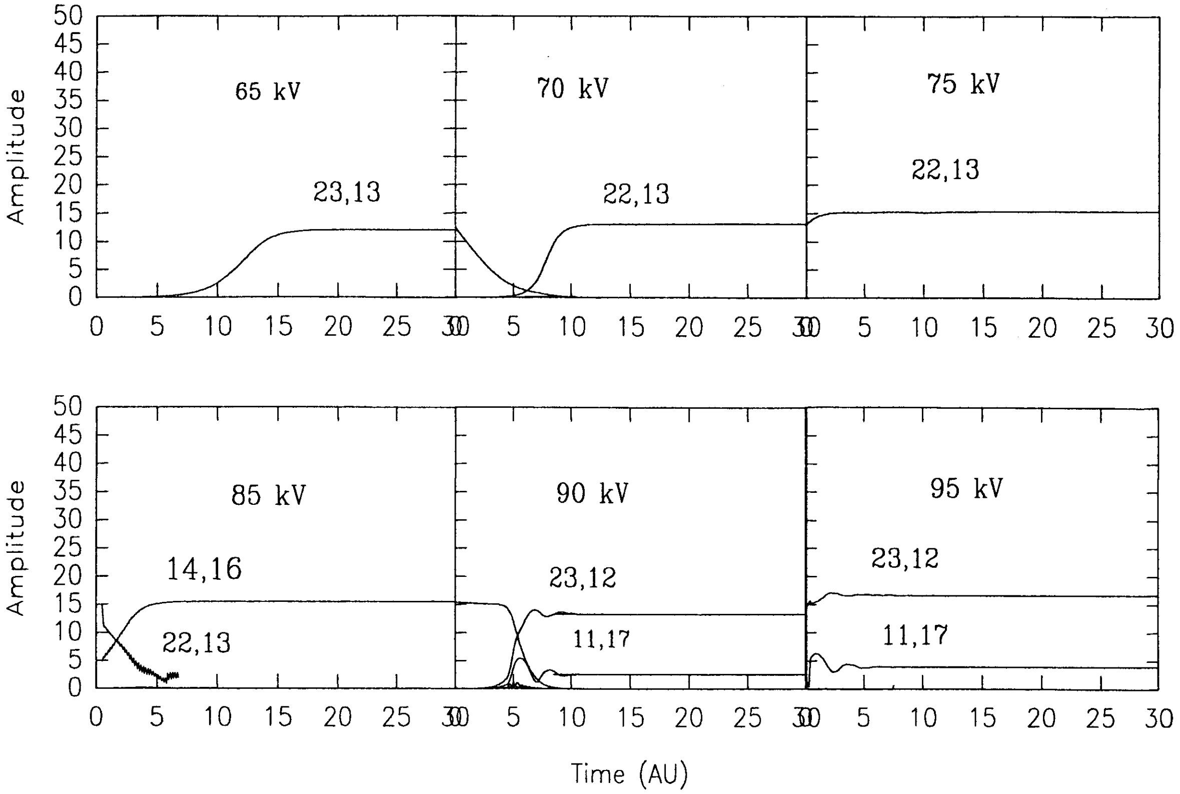

Figure 4.13: Multimode simulations for the case without the inner conductor. The $TE_{21,13}$ mode could not be obtained [11].

Multimode code results from the uniform and untapered inner conductor case are shown in Figure 4.14. Oscillations were found to start in the $TE_{21,14}$ mode. At 70 kV, the mode was changed to the $TE_{22,13}$ mode, while several others died quickly. At 90 kV, the desired mode of $TE_{21,13}$ started and suppressed all others. This mode remained stable until 98 kV, where it was replaced by the $TE_{23,12}$ mode. This gives sufficient operating space to allow for voltage variations found with most power supplies/modulators. The final efficiency is 45%.

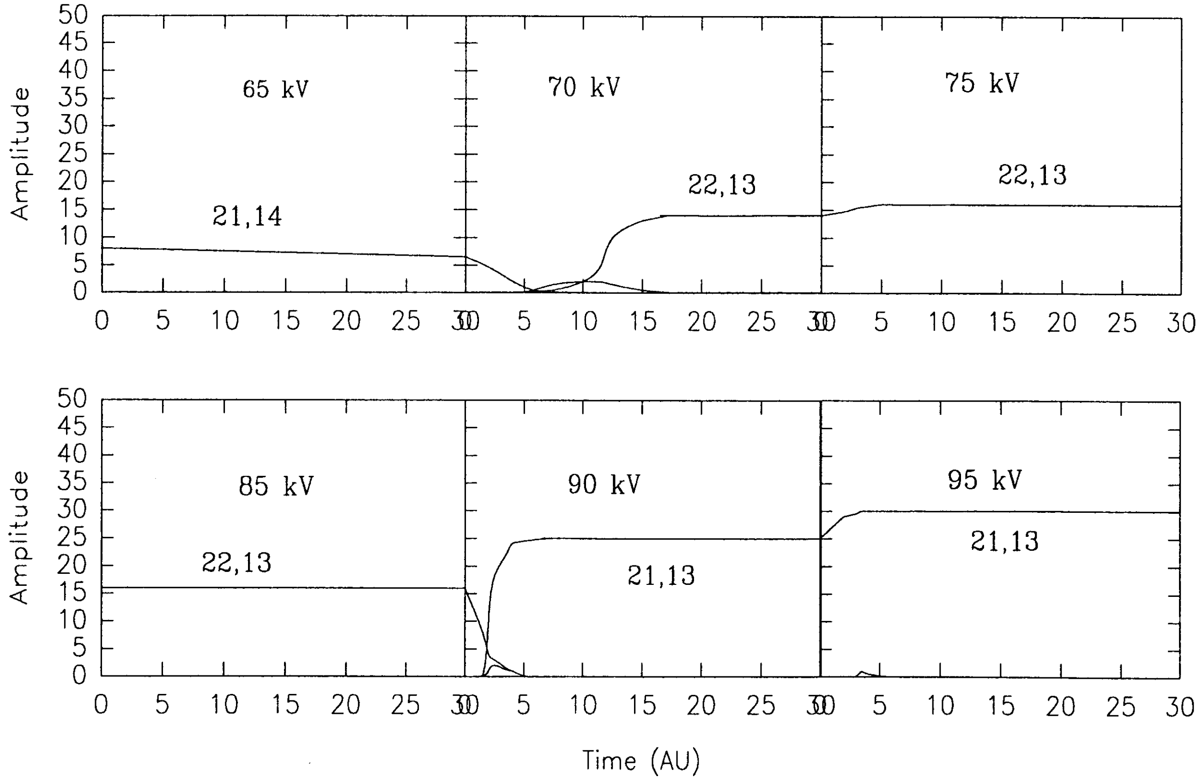

Figure 4.14 (a): Multimode simulations for the case with an inner conductor - uniform 6.02 mm radius inner conductor [11].

With the inner conductor having a 1° taper, the $TE_{19,14}$ mode dominated and operated with poor efficiency. This was attributed to the high Q value caused by the taper. Although another taper angle could have mitigated this issue, the simulations with a uniform inner conductor predicted good efficiency and thus were chosen for the final design.

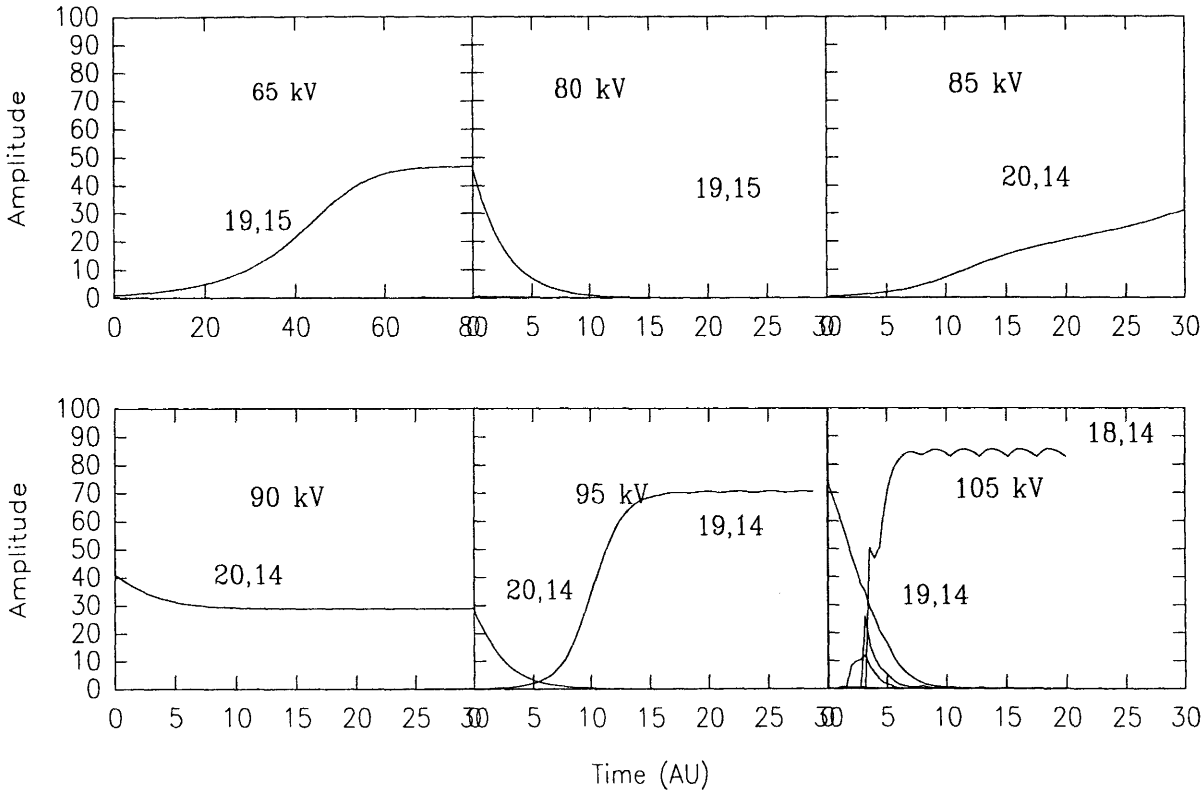

Figure 4.14 (b): Multimode simulations for the case with an inner conductor - 1° tapered inner conductor [11].

4.3 Electron gun design

The electron gun was built in the Inverted Magnetron Injection Gun (IMIG) configuration, which has a configuration with the cathode at a larger radius than the first anode as shown in Figure 2.1 and discussed in section 2.1. The inner anode is held at ground potential and serves as a support for the coaxial conductor at the gun end as well as the collector end of the gyrotron. The inner anode is electrically isolated from the coaxial conductor in order to measure the beam interception on them independently. Since the required tolerances are small and the inner conductor needs to be cooled in a CW device, this configuration is necessary.

Baird and Lawson's [73] equations were the starting point of the analytical calculations for the electron gun. The design was to have an 8.4 MW beam which would provide 3 MW RF power, at an efficiency of 36%, and an average radius of 0.775 cm. Further, the beam width in the cavity (fully compressed) i.e. the spread in gyrocenters was held to 0.35 mm ~ $1/6\lambda$. The electric field strength at the anode was limited to 70 kV/cm, which is a conservative maximum for CW operation. These parameters and constraints helped determine the remaining parameters, which are summarized in Table 4.2. The design current density of the M-type dispenser cathode was 5.5 A/cm^2 at a temperature of 950°C [32], 0.39 times that of the space charge limit (which is usually conservatively indicated by these calculations).

The gun was modeled using the EGUN [17], on a DOS-based personal computer. Five sections were used to remain within the 500×500 mesh unit limit found with a compilation designed to run on a 486 computer with 8 MB of memory, and to appropriately vary the mesh size to adapt to the beam larmor orbit (as shown in Figure

Cathode Radius	4.9 cm
Anode radius	3.2 cm
Cathode current	0 – 95 Amps
Cathode voltage	0 – 110 kV
Anode electric field	62 kV/cm
Magnetic field at cavity	5.9 Tesla
Magnetic compression	35
Operating current/space charge	0.39
Cathode current density	5.5 A/cm^2
Beam thickness (fully compressed)	0.035 cm
Average beam radius (fully compressed)	0.82 cm
Cathode slant angle	25°
Cathode slant length	0.468 cm

Table 4.2: Gun parameters, from analytical calculations.

4.15). Further detailed investigations of the gun were done on a 300 MHz Pentium based machine and different characteristics of the gun, the magnetic fields, and the mechanical alignment was noted, as discussed in section 4.3.1. Each of the simulations took around 10 minutes on the Pentium machine. The magnetic field was input via an on-axis array, which the code used to generate the appropriate off-axis fields.

A plot of the trajectories and the magnetic field profile done during the design phase is shown in Figure 4.15, which shows all the five sections. The final beam parameters are summarized in Table 4.3. The perpendicular velocity spread was quite low, 3.4% at an alpha of 1.44. The alpha was sensitive to the beam current, although the spread remained reasonable throughout the range of 7.6 to 76 A. The design simulations of beam alpha and velocity spread as functions of the beam currents are plotted in Figure 4.16. The alpha was easily controlled with the beam voltage, as shown in Figure 4.17, which allows control of alpha without changing the final beam position (which would happen if one changed the magnetic field at the cathode with the help of the gun coils).

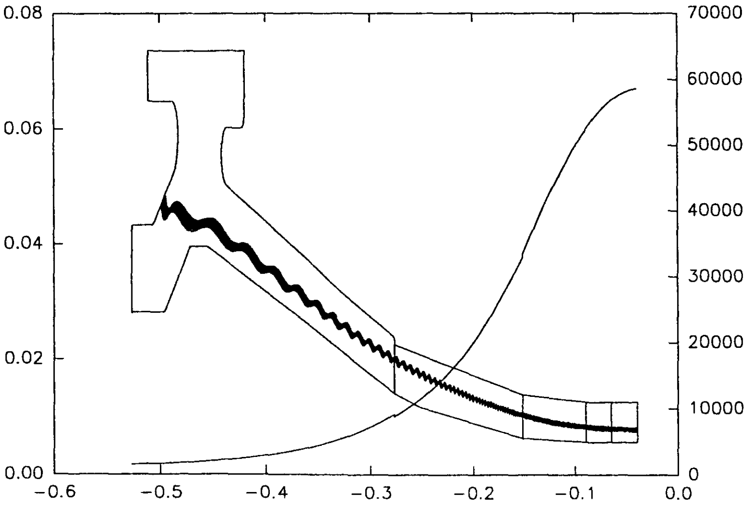

Figure 4.15: Beam trajectories and magnetic field profile for a design EGUN simulation [11].

The beam velocity spread is quite sensitive to the beam's position relative to the inner anode. Hence, final optimization of that distance in the final gun is controlled by a pair of oppositely driven magnetic field copper gun coils centered at the cathode – called the *gradient* coils. To adjust the field at the cathode and thus the alpha (and consequently beam radius), a smaller copper gun coil was placed in between these two coils – called the *absolute* coil. As is true in most gyrotrons these days, the main field was provided by a superconducting magnet which has a bore of ~15 cm and a flat field region of ~ 20 cm. The electric field near the electrodes was found to be 85 kV/cm by the code POISSON [74], which is slightly larger than desired, but within engineering bounds [75].

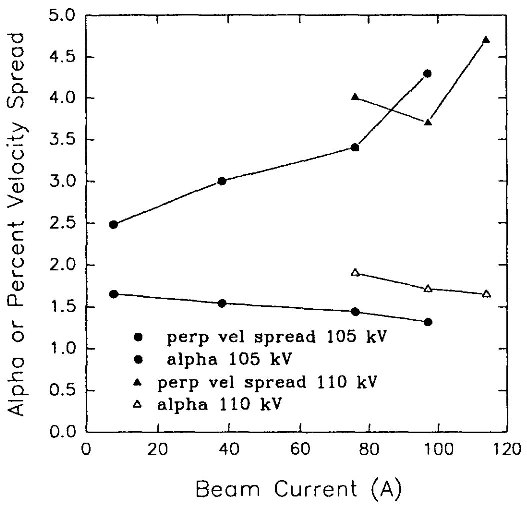

Figure 4.16: Alpha and perpendicular velocity spread versus beam current (V = 95 kV = const.) [11].

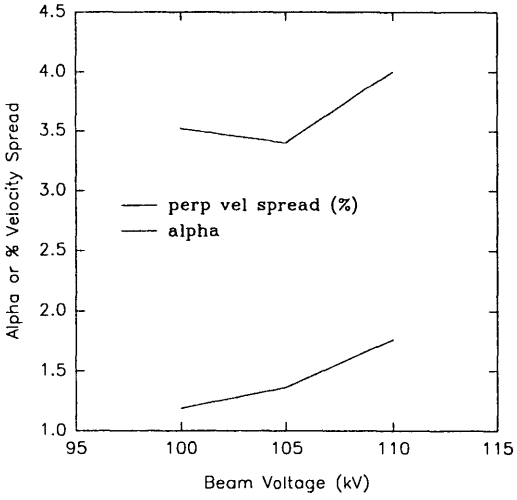

Figure 4.17: Alpha (bottom) and perpendicular velocity spread (top) versus beam voltage (I = 88 Amps = const.) [11].

A mechanical design for the gun is shown in Figure 4.18. The outer diameter of the ceramic chosen was 20.3 cm (8 inches) to allow satisfactory distribution of the potential along its length. The inner conductor forced the potential distribution near the center, over a relatively short length. The electric field along the insulator was found to be less than 20 kV/cm (using POISSON [74]).

Alignment and centering of the inner conductor with the cavity and the magnetic field is done without breaking vacuum, in deference to the sensitivity of the position of the anode near the cathode. The anode design includes three spring plungers which allows adjustment of the anode with respect to the cathode and the electron beam. The gun can be isolated from the tube vacuum with the help of a standard gate valve. Initially, the inner conductor from the cavity was inserted into the inner anode while the tube was under vacuum with a bellows arrangement at the collector end of the tube (see Figure 4.26). Later, this arrangement was simplified with an axial output mode (discussed in section 4.5).

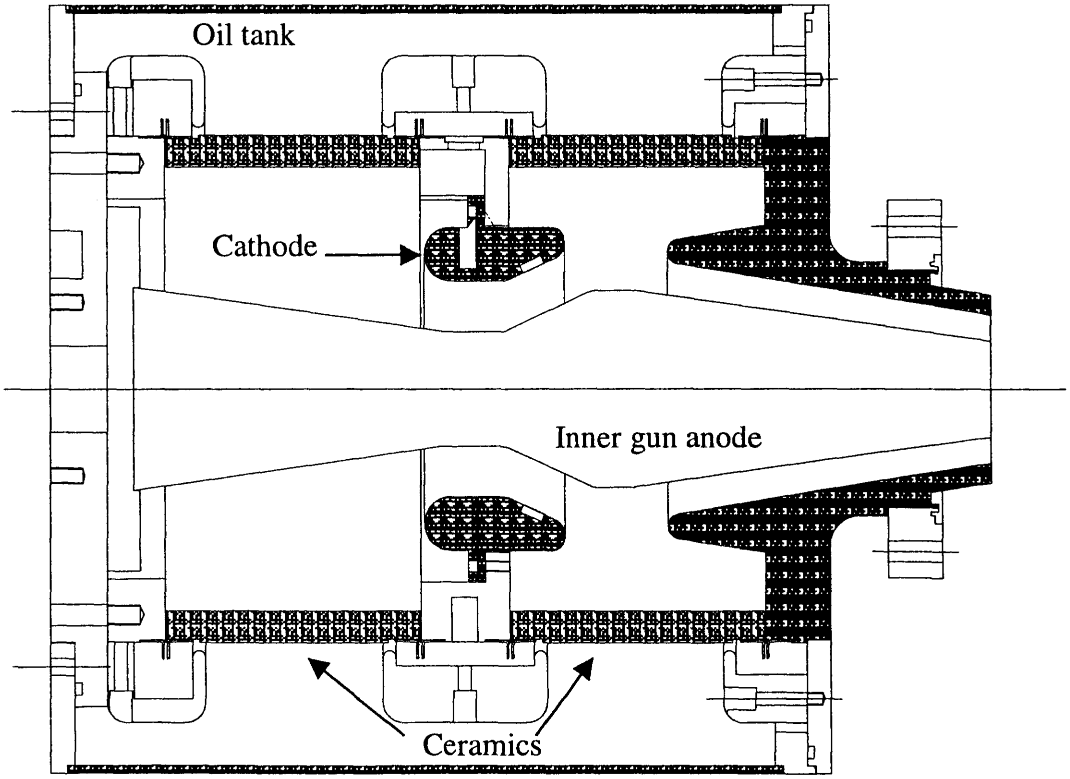

Figure 4.18: Mechanical drawing of the inverted MIG electron gun used for the coaxial gyrotron experiment [11].

4.3.1 Detailed EGUN simulations

Detailed simulations regarding the operational parameters was done for the coaxial gyrotron in1998. These simulations helped in the day-to-day operation of the gyrotron by providing the exact values of alpha, velocity spreads (perpendicular and parallel), beam width, etc. versus small changes in the magnetic field, mechanical alignment, and operating voltages and currents. These simulations were also done with the help of an advanced four-point scheme of space charge weighting [75] in EGUN as compared to the design which was done with a slightly lesser sophisticated two-point weighting scheme. Also the number of mesh points that each of these simulations could accept was 3×10^6, which meant that we could simulate the entire gyrotron structure, from gun to cavity, in one section rather that the five sections used for the EGUN simulations during the design.

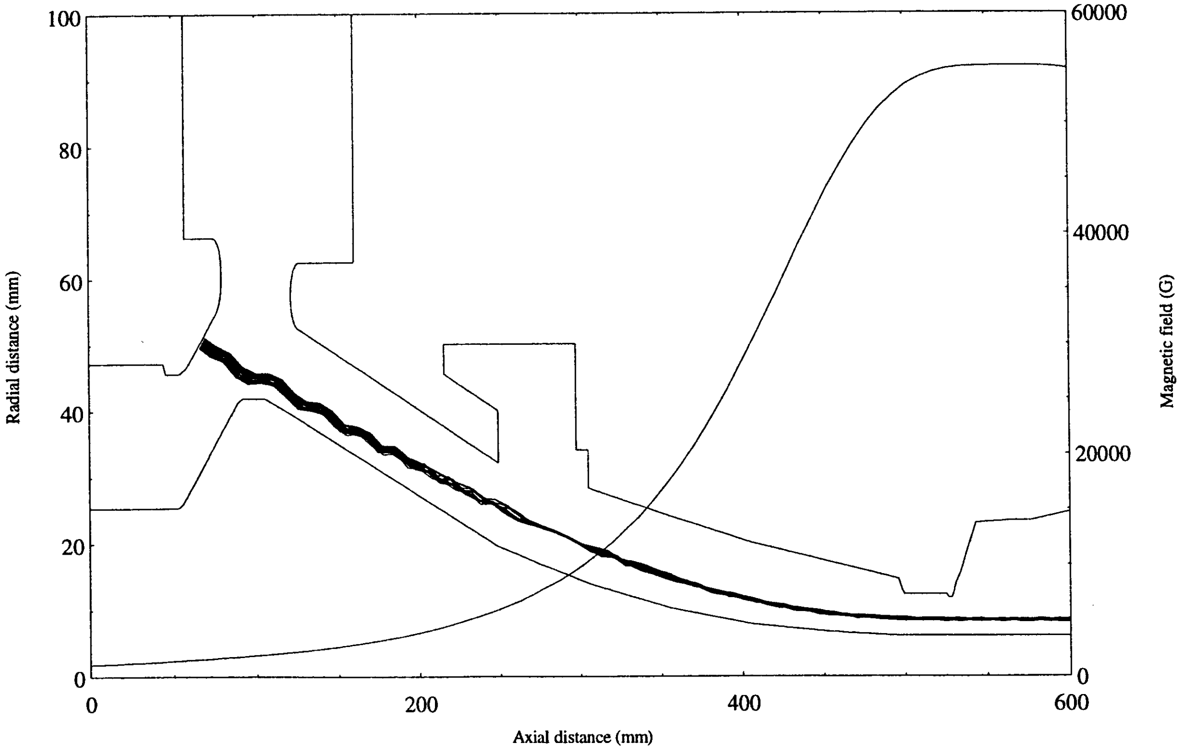

Figure 4.19: Beam trajectories and magnetic field profile for a design EGUN simulation.

The simulations were run on a faster 300 MHz Pentium computer and with approximately twice the mesh density of the previous design EGUN runs. Due to all these improvements and the greater number of parameters investigated, we were able to generate a detailed picture of the coaxial gyrotron, which aided during the operation of the tube and in comparisons of experimental data with simulations.

Figure 4.19 shows the beam trajectories and the geometry of the simulation, which looks similar to the previous simulations (as can be expected). One can note that this simulation is clearly in one section as compared to the design simulation shown earlier in Figure 4.15. Figure 4.20 and 4.21 show the variations of alpha and velocity spread as a function of beam voltage and beam current. These results are in general agreement with the EGUN results from the design, and are more precise because of the improved EGUN version and mesh sizes (which are actually twice as fine from the design runs) for these runs.

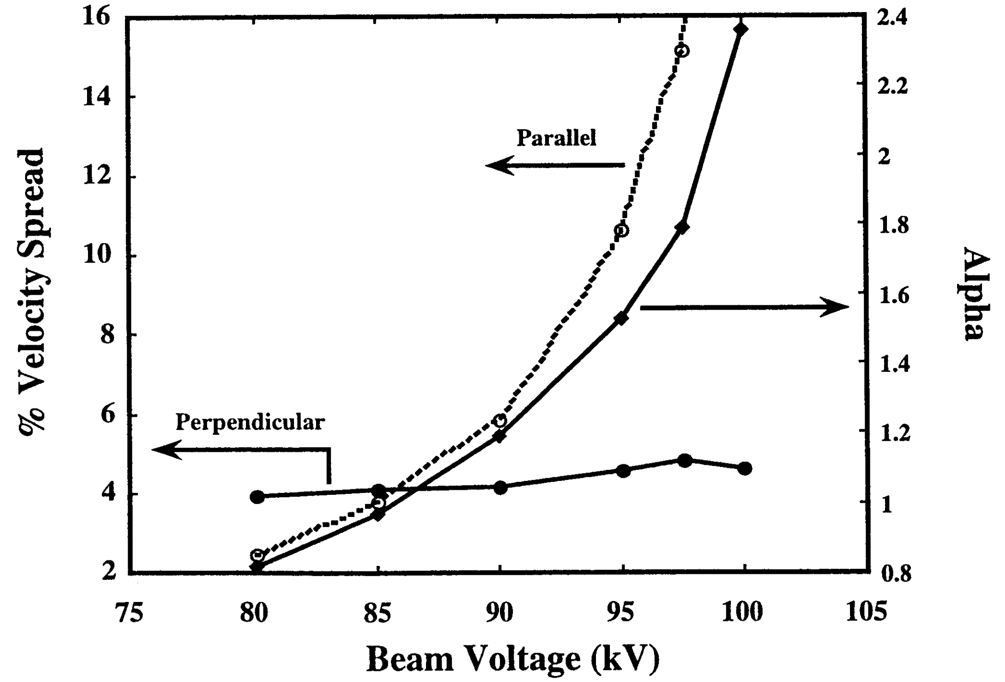

Figure 4.20: Velocity ratio (alpha), parallel and perpendicular velocity spread versus beam voltage.

Figure 4.20 above again demonstrates the ability to control the alpha by changing the voltage. This establishes a method to change the alpha without changing the magnetic field at the cathode (which would otherwise change the beam radius).

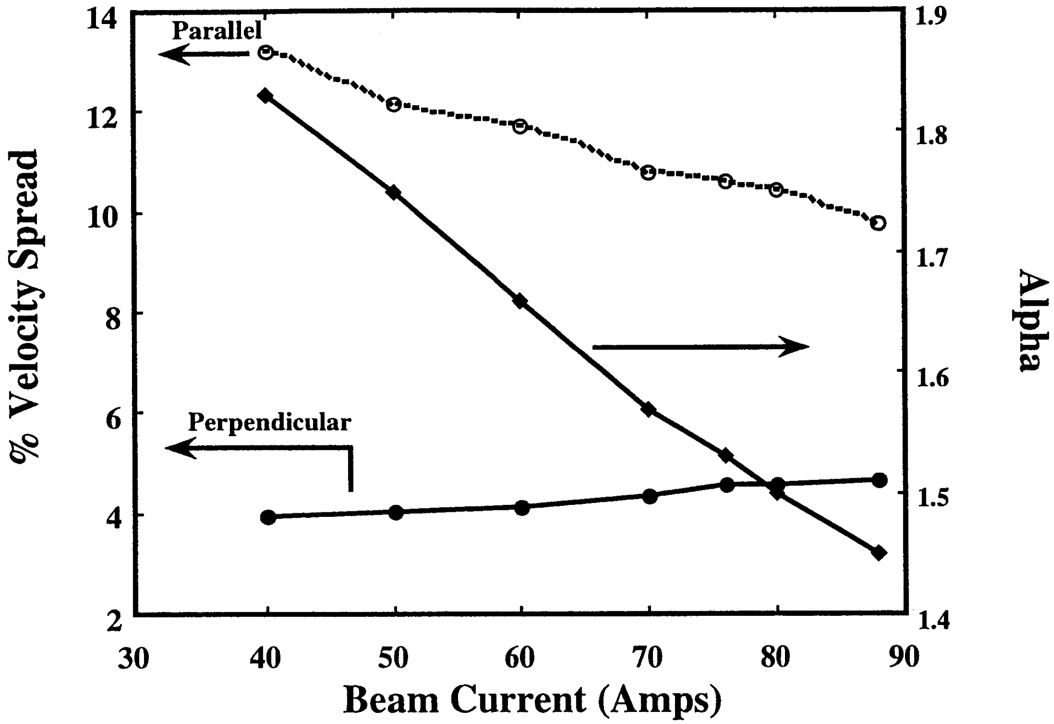

Figure 4.21: Velocity ratio (alpha), parallel and perpendicular velocity spread versus beam current.

Figure 4.22 shows the variation of the velocity spread and alpha with respect to axial displacement of the inner conductor. Here, the coaxial conductor and the inner anode (together) were intentionally displaced from its design value in the axial direction keeping the cathode in a fixed position. The data shown in Figure 4.22 is from –1 cm (moved toward the cathode) to +1 cm (moved toward the cavity). The changes in alpha and velocity spread in this case followed the adiabatic scaling law.

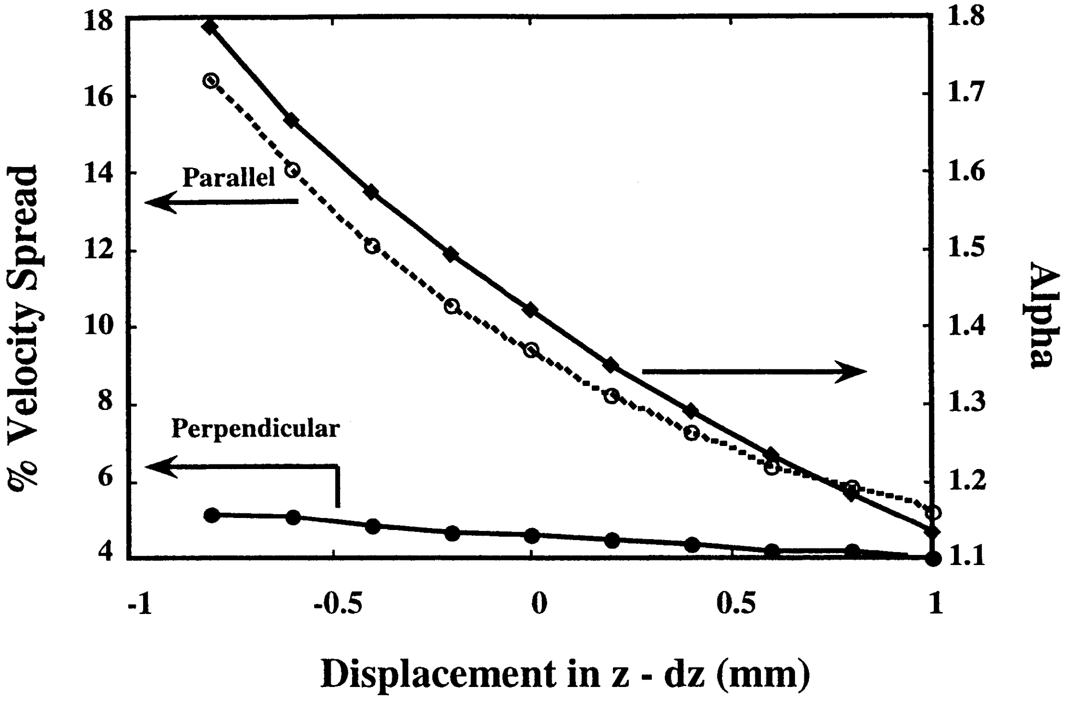

Figure 4.22: Velocity ratio (alpha), parallel and perpendicular velocity spread versus displacement of inner conductor in the axial direction.

Another misalignment that we investigated was radial misalignment of the inner conductor with respect to the cathode. This is a slightly tricky calculation, since, if the inner conductor is closer to the cathode on one side by 0.5 mm then it is further away from the cathode by the same amount on the other side. Thus, a displacement of 0.5 mm was calculated by taking the average of all radii between – 0.5 mm and + 0.5 mm. This was done for both the velocity spreads and the alpha values. The results thus obtained from these simulations are shown in Figure 4.23. One can note from Figure 4.23 that misalignment in the radial direction has a rather modest effect on the alpha and the velocity spread.

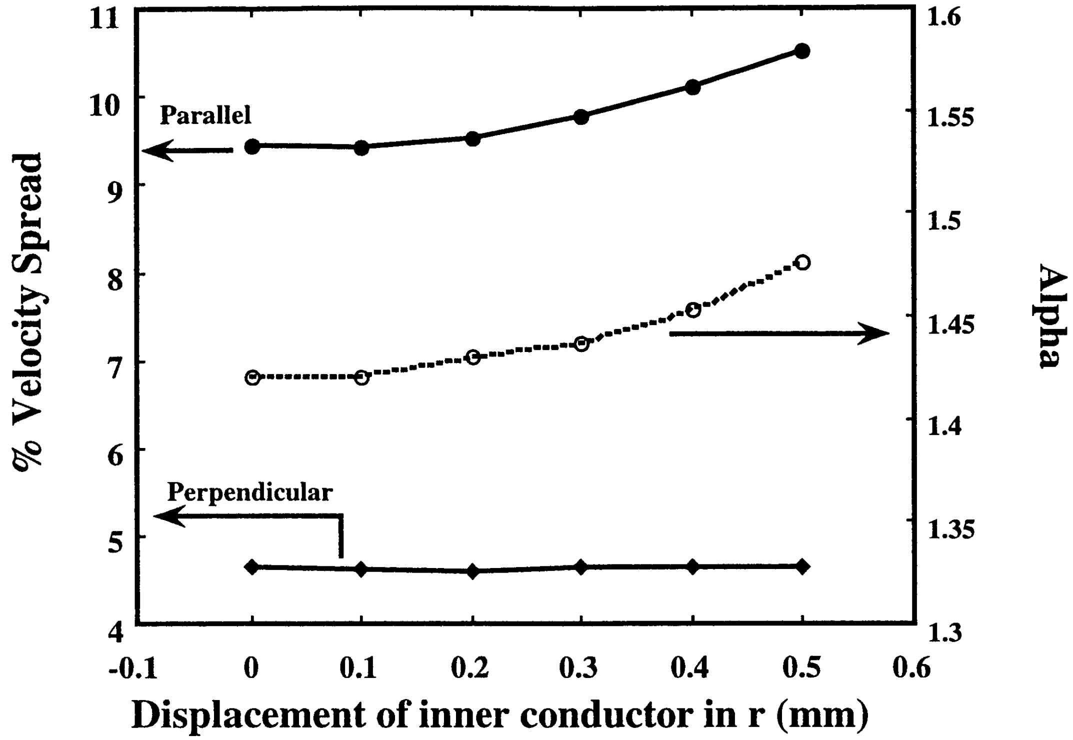

Figure 4.23: Velocity ratio (alpha), parallel and perpendicular velocity spread versus misalignment of inner conductor in the radial direction.

During the operation even the data shown in Figure 4.20 to 4.23 is sometimes not sufficient and more granular detail of changes in alpha and velocity spread versus changes in individual gun coil currents is required. An example of such data is shown below in Figure 4.24, which demonstrates the curves one uses for velocity ratio and velocity spread when changing the current in a particular gun coil (in this case the center gun coil – *absolute* gun coil).

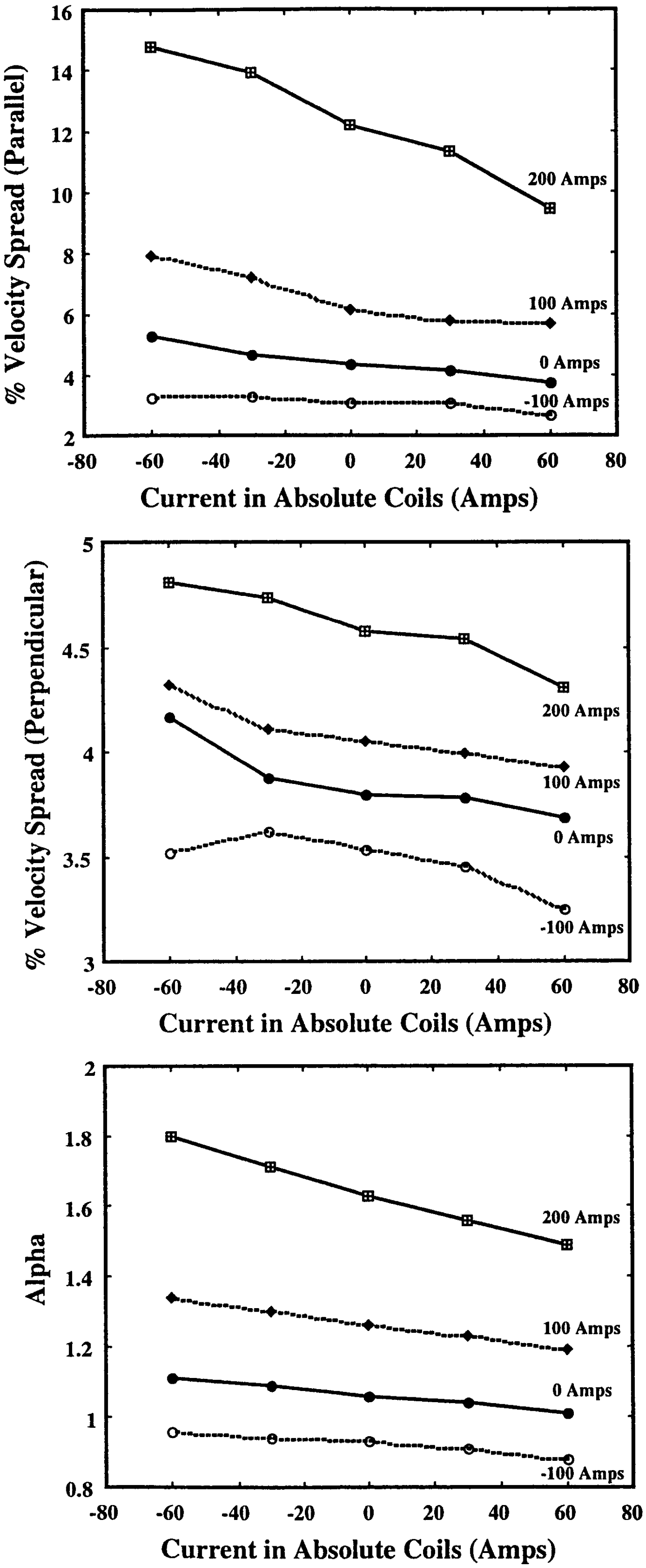

Figure 4.24: Velocity ratio (alpha), parallel and perpendicular velocity spread versus current in the absolute coil (the center one of the gun coils).

4.4 Mode converter

A quasi-optical mode converter was used for the initial experimental runs. The $TE_{21,13}$ power was converted to a guassian beam in free space and power was extracted radially. The mode converter was designed to transform the $TE_{21,13}$ cylindrical waveguide mode at 140 GHz to two satellite modes ($TE_{18,14}$ & $TE_{22,13}$), which form a guassian beam in free space. The converter itself is an irregular cylindrical waveguide section followed by a step-cut launching aperture and a single reflector for beam focussing and steering.

The irregular waveguide (or prebunching section) obtained the mode mix in the launching waveguide such that the field intensity on the wall (or wall current) has a Gaussian profile [77-79]. A Gaussian profile of the field intensity was achieved by pumping power from the main mode, $TE_{21,13}$, to the two satellite modes, the $TE_{18,14}$ (i) and the $TE_{22,13}$ (j). A helicoidal converter, described by Equation 4.2, is used to obtain this type of mode conversion:

$$r(\phi, z) = r_0[1 + \varepsilon_1 \cos(\beta_1 z - l_1\phi) + \varepsilon_2 \cos(\beta_2 z - l_2\phi)] \tag{4.2}$$

where $\beta_1 \approx \pm(\beta_0 - \beta_i); \beta_2 \approx \pm(\beta_0 - \beta_j); l_1 \approx \pm(m_0 - m_i); l_2 \approx \pm(m_0 - m_j)$. The subscript 0 corresponds to the main mode ($TE_{21,13}$). The design parameters for the mode converter are shown in Table 4.4. Coupled mode theory is used to analyze the operation of the prebunching section. In addition to the two selected satellite modes, seventeen other modes were found to couple to the $TE_{21,13}$ mode through the helicoidal wall perturbations. These modes increased the Gaussian amplitude and reduced the side lobe levels. Figure 4.25 shows the mode content in the prebunching launcher, as predicted by coupled mode theory.

Table 4.4: Design parameters of the mode converter [11].

Input Mode	$TE_{21,13}$
First Satellite Mode	$TE_{18,14}$
Second Satellite Mode	$TE_{22,13}$
β_1	0.71 1/cm
β_2	1.53 1/cm
l_1	3
l_2	1
ε_1	0.0012
ε_2	0.0016

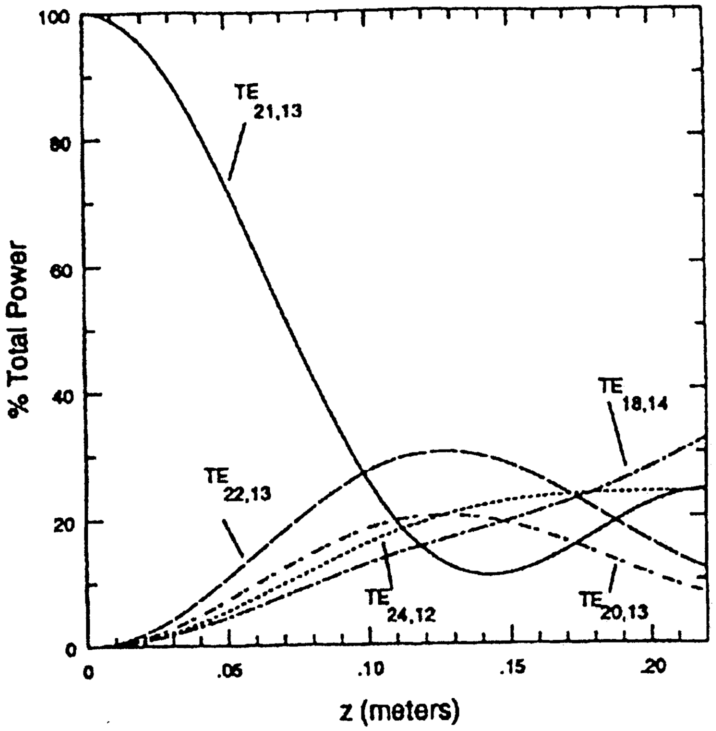

Figure 4.25: Mode composition versus axis in the pre-buncher. The input mode and the four most significant satellite modes shown (15 other smaller modes are not shown) [11].

The radiation is launched by cutting the waveguide wall around a Gaussian bunch. The wall is cut at a position where the wall current is a minimum to reduce edge diffraction effects. The Stratton-Chu diffraction theory [80] was used to simulate the launch of the radiation from the prebunching section and to predict the expansion of the launched beam. Good agreement was obtained when the theoretical expansion was compared to the expansion of an elliptic Gaussian beam. Since, the prebunching launcher radiates a Gaussian-like beam; the preliminary design of the reflector was made using Gaussian optics. The reflection at the single steering and focussing mirror and to predict the final output beam was done by Stratton-Chu diffraction theory. The reflector design was made based on the results of this simulation. Diffraction analysis shows that > 90% of the incident $TE_{21,13}$ radiation would propagate through the quasi-optical mode converter and exit radially through the window as a Gaussian-like beam.

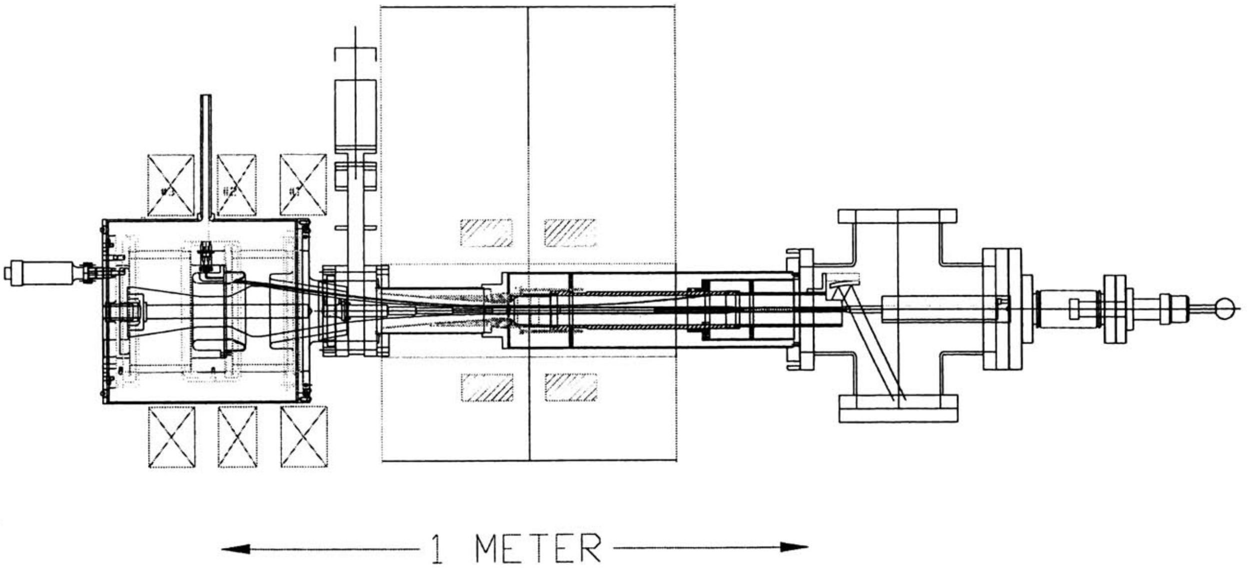

Figure 4.26: Mechanical (AutoCAD) drawing of the gyrotron with the mode converter and radial power output. Note the plunger arrangement on the collector (right) end, which helped us introduce the coaxial conductor without breaking vacuum [11].

4.5 Experimental runs

In this section we describe the various modes in which we ran the gyrotron, besides the measurement of the electron beam parameter mentioned in section 2.3. The initial design of the gyrotron was with a mode converter and one mirror. The power was mode converted to a gaussian beam, which was then reflected by the mirror and extracted radially from the gyrotron, as shown in figure 4.27.

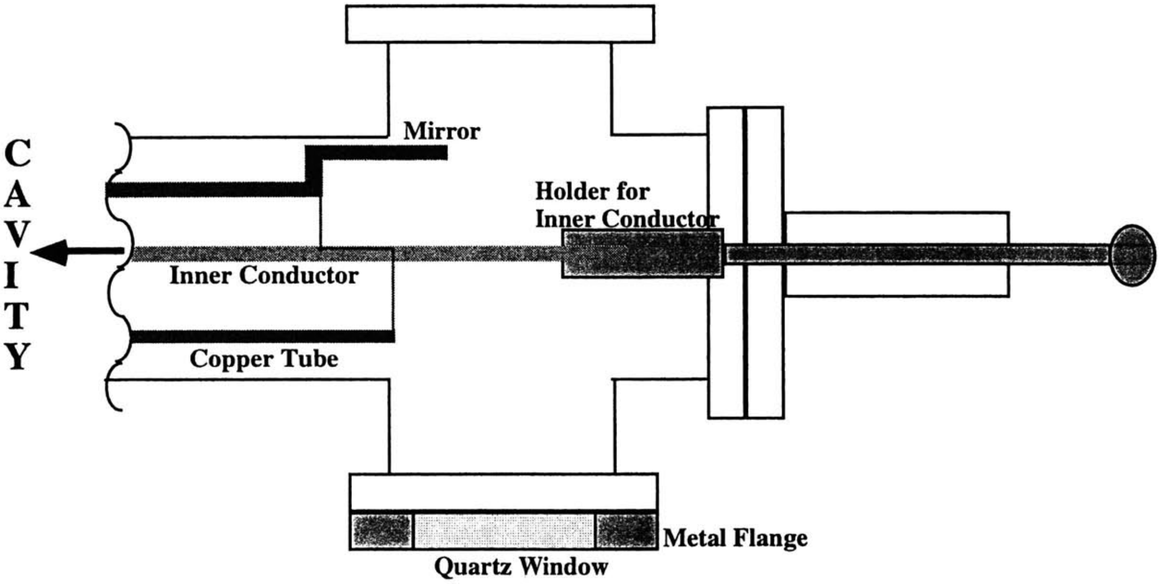

Figure 4.27: Schematic of initial runs with a mode converter and one mirror. Power was extracted radially from the quartz window.

The radial extraction mode was found to have problems with some of the power being scattered away from the window and onto the flanges. Hence, we simplified the geometry by removing the mode converter and adding a straight section, which just transported the power from the cavity to the window. Here power was extracted axially as shown in Figure 4.28. The support shown in the figure are two 0.32 cm diameter solid MACOR rods which hold and center the coaxial conductor on the output side of the tube.

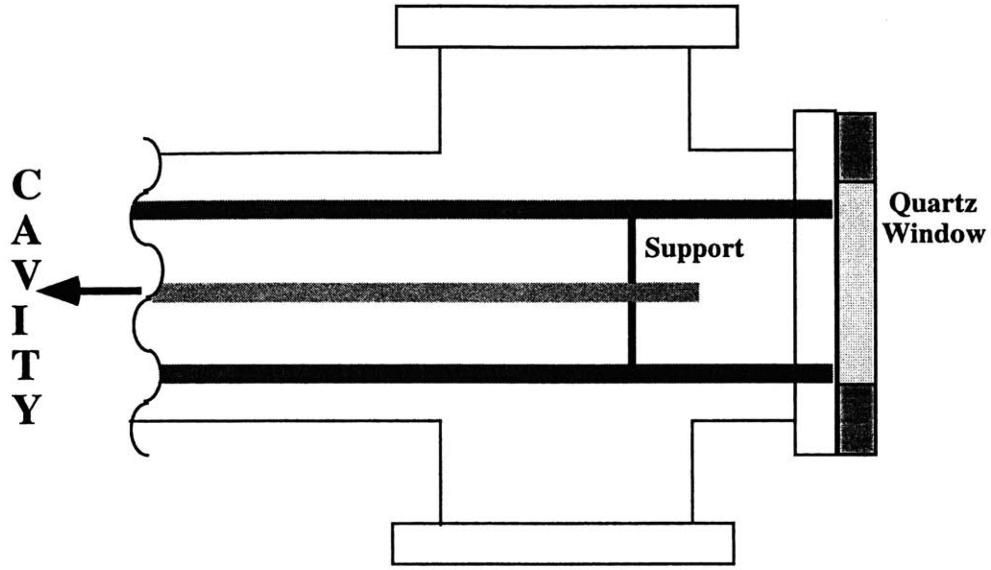

Figure 4.28: Schematic of runs with axial power extraction from the quartz window.

Furthermore, since there is good understanding of the behavior of a gyrotron oscillator without a coaxial insert, we ran the gyrotron in a 'empty cavity mode' where the coaxial insert was removed and power and modes were investigated. This mode is shown in Figure 4.29. The main motivation for this operational mode was the benchmarking of this tube to known results – since we know and understand the operation of gyrotron tubes without coaxial conductors much better – due to the years of experience of operating several of them at MIT. The results that we obtained from all these runs are discussed in chapter 5.

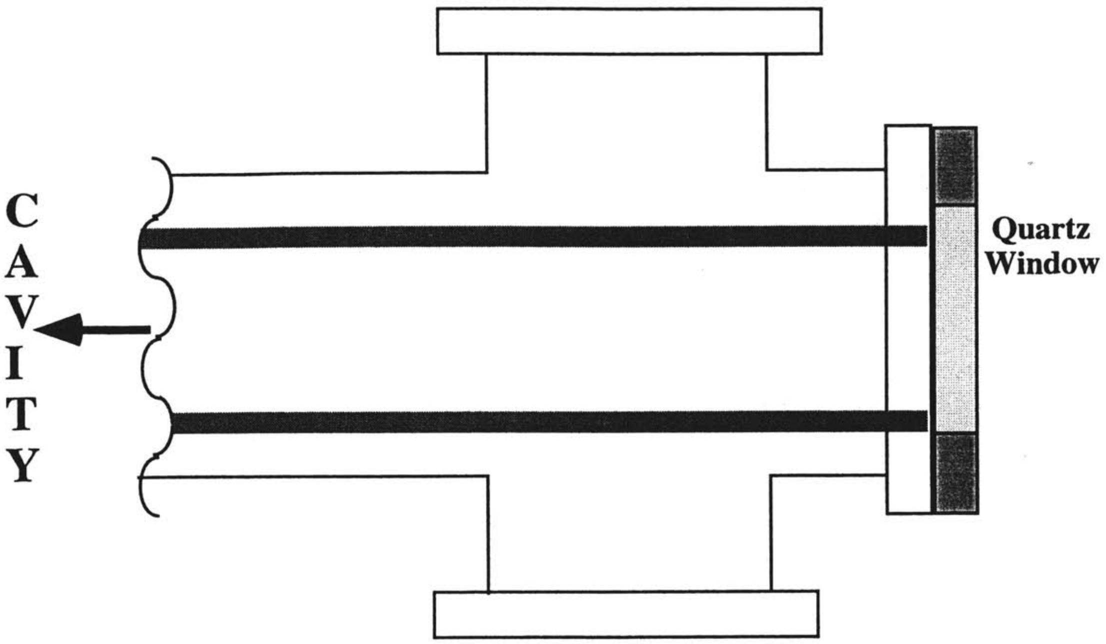

Figure 4.29: Schematic of the empty cavity runs with axial power extraction from the quartz window.

Chapter 5

Coaxial Gyrotron Experimental Results

5.1 Introduction

The previous chapter described the design of the coaxial gyrotron experiment that was operated at MIT. The operation of the gyrotron involved three different modes of operation. The first was the mode where we had the coaxial conductor inserted and had a mode converter with which power was extracted radially – *the coaxial conductor with mode converter*. The second operational mode was with the coaxial conductor was removed and the tube run as a regular gyrotron tube – *the empty cavity mode*. This was done primarily to understand the behavior of power and modes from the gyrotron in order to compare these parameters with the known behavior of several gyrotron oscillators that have been previously operated at MIT in the same mode. The final mode of operation was one with the *coaxial insert and without the converter*, where power was extracted axially. Between the second and the third modes of operation there was an extensive study done of electron beam in the gyrotron where three different techniques were used to measure and understand the cathode emission as a function of the azimuthal angle. All of these results are presented in this chapter and are discussed in chapter 6. A schematic of the coaxial gyrotron is shown in Figure 4.1 and a mechanical drawing is shown in Figure 4.26.

5.2 Coaxial conductor with converter mode

The first set of experiments that were initiated after the coaxial gyrotron was designed and built was the one in which we used a mode converter and a single mirror. In order to visualize the tube for these results, we once again show Figure 4.27 below in Figure 5.1.

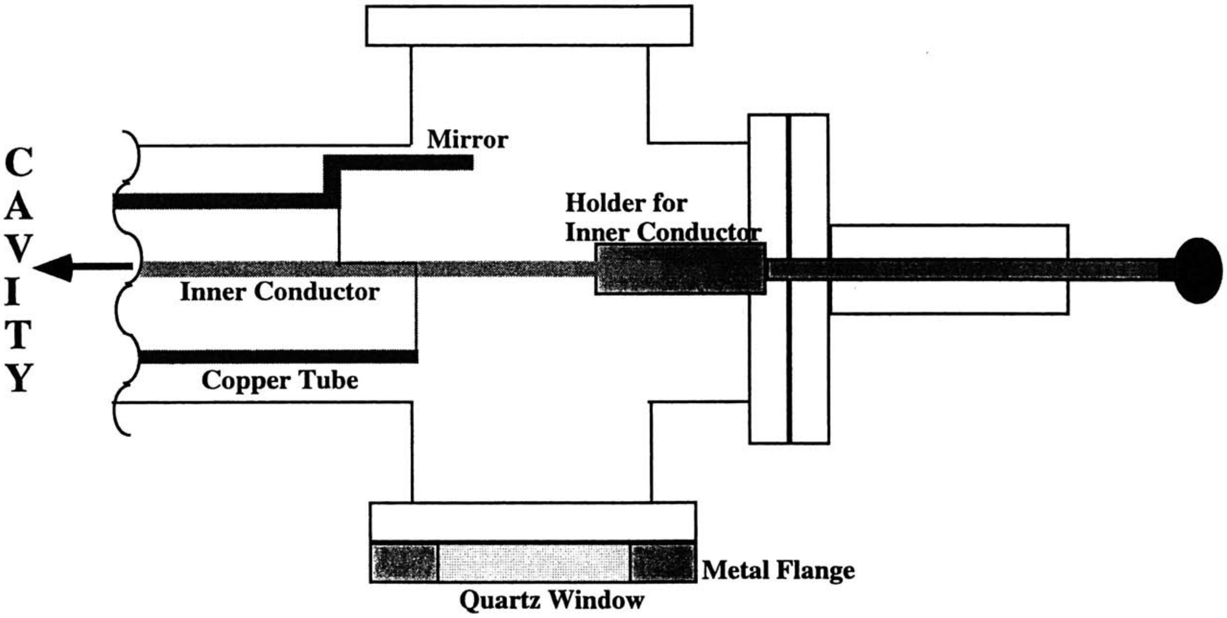

Figure 5.1: Schematic of initial runs with a mode converter and one mirror. Power was extracted radially from the quartz window shown.

The mode converter in these runs converted the $TE_{21,13}$ cylindrical waveguide mode into two satellite modes, $TE_{18,14}$ and $TE_{22,13}$, which form a gaussian beam in free space. In this mode the gyrotron was usually operated at full parameters of 95 kV, 76 Amps. The gun itself was tested up to ~ 10 MW i.e. 105 kV, 93 Amps, which is a record for this class of gyrotron oscillator tubes (to the best of the author's knowledge). The beam was transported from the gun to the collector without interception, and microwaves were generated in the 135 – 143 GHz range. Operation was limited to the low alpha regime of $\alpha \approx 1.1$ above which the beam started intercepting the coaxial insert. The maximum power obtained was ~ 1 MW. Figure 5.2 shows the result of the power obtained versus the main magnetic field. The plot also shows the dominant modes that were observed at each of the points of operation. Experimentally, we saw some mode competition and that the design mode was not observed.

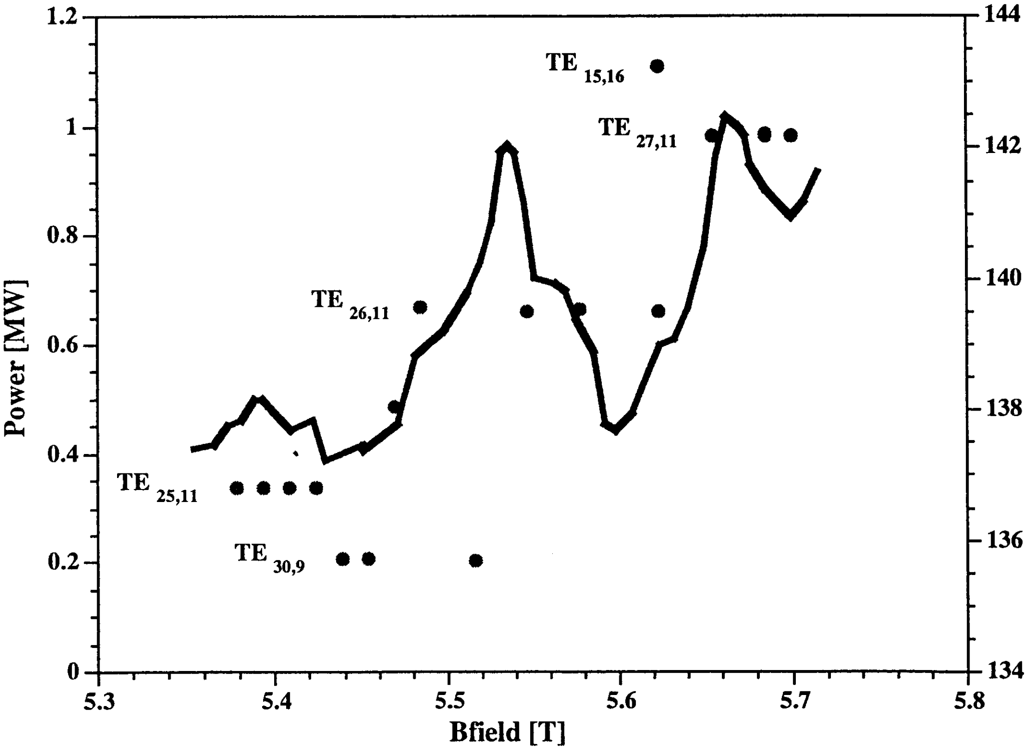

Figure 5.2: Output power (curve) and frequency/modes (points) versus the main magnetic field. The operating parameters were 92 kV, 70 Amps, giving an efficiency of operation of ~14 % for a maximum power output of ~ 1 MW (cathode 1).

On closer inspection, we found that the reason that the design mode, $TE_{21,13}$, was not observed was because the main magnetic field was directed so as to excite the left-handed co-rotating polarized modes (as opposed to the right-handed modes that the tube was designed for). Hence, upon switching the direction of the magnetic field we did observe the $TE_{21,13}$ mode, although the power obtained was only 0.5 MW. Other results that we obtained at this point are shown in Figure 5.3 and 5.4 which show the output power and efficiency versus beam current and main magnetic field. The modes were not specifically measured for these sets of data.

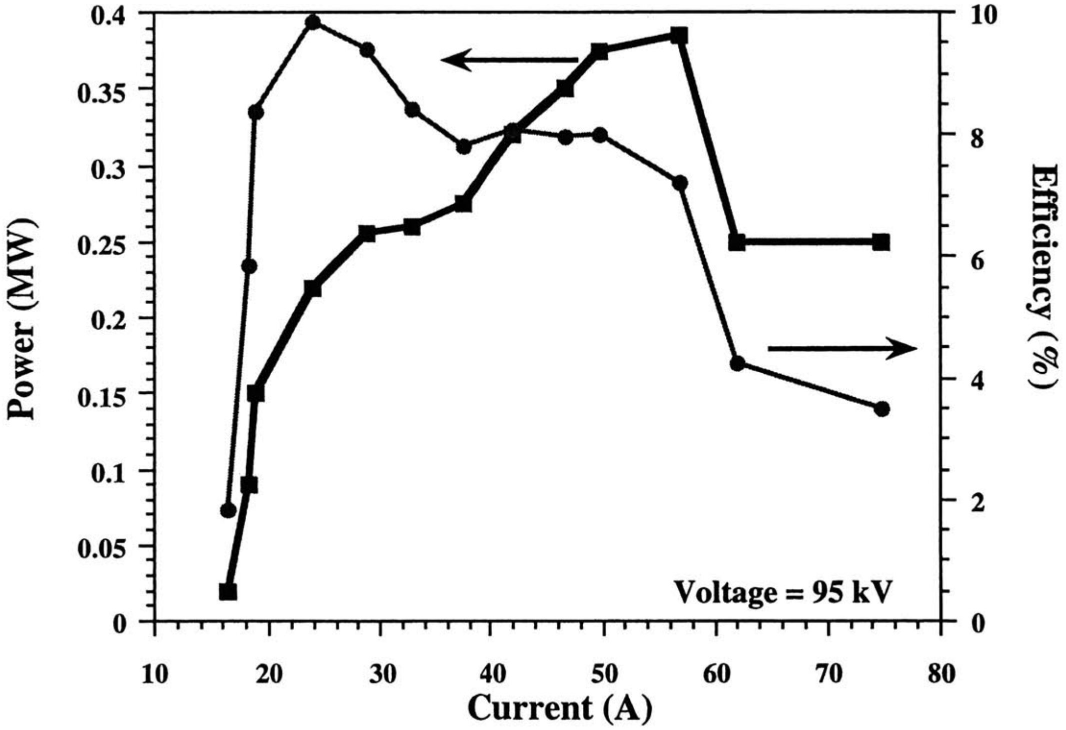

Figure 5.3: Output power and efficiency versus beam current. Operating voltage was 95 kV (cathode 1).

During these runs, which lasted over six months, we were unable to get any more power than the 1 MW result we had recorded earlier. At the time, the main concern was thought to be the exact alignment of the cavity , the electron beam itself, and the coaxial

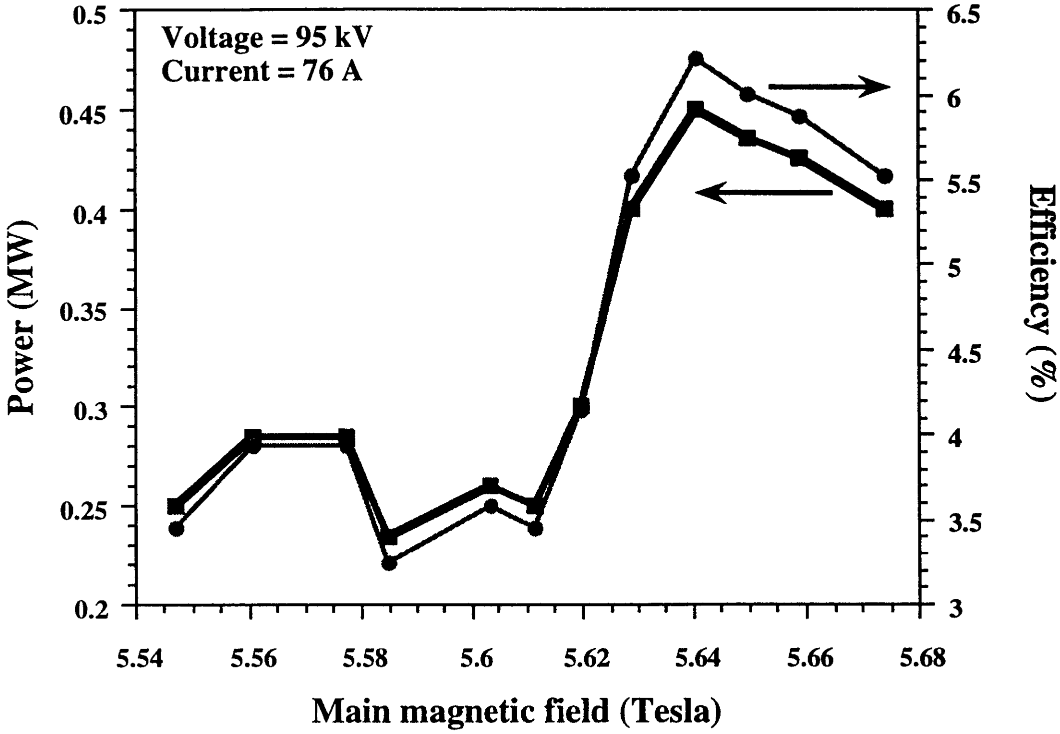

Figure 5.4: Output power and efficiency versus main field (cathode 1).

conductor – all three aligned with respect to each other to within 0.25 mm. This is a general concern that has been expressed by several groups working on coaxial gyrotrons as well as regular gyrotrons [13,81,82,83]. Upon opening the tube, we found that some of the power was not making it out of the tube and was hitting the flange. This prompted a decision to simplify the geometry and get the maximum power output out of the tube by removing the mode converter and mirror. Thus, the mode converter and the mirror were replaced with a straight copper section, which would faithfully transport the power out of the tube. At this point, we also decided to first operate the gyrotron without a coaxial conductor in order to understand the output power, mode, and efficiency of the tube.

5.3 Empty cavity mode (without coaxial conductor)

After the initial set of runs we simplified the collector end of the tube by removing the mode converter and the single mirror and having an axial output. Additionally, for these runs we also removed the coaxial conductor (the inner anode in the gun region was not removed) and operated the tube in order to investigate the power, the modes, the alpha, and the efficiency. The reasoning behind this was to compare the results between the coaxial conductor and no coaxial conductor cases as well as to try and understand the general mode characteristics and mode competition in the tube. The electron gun and the cathode were not changed for this experiment. Also, alignment in this mode of operation was easier since we only had to align two things – the electron beam and the cavity. A schematic of this mode of operation is shown in Figure 5.5.

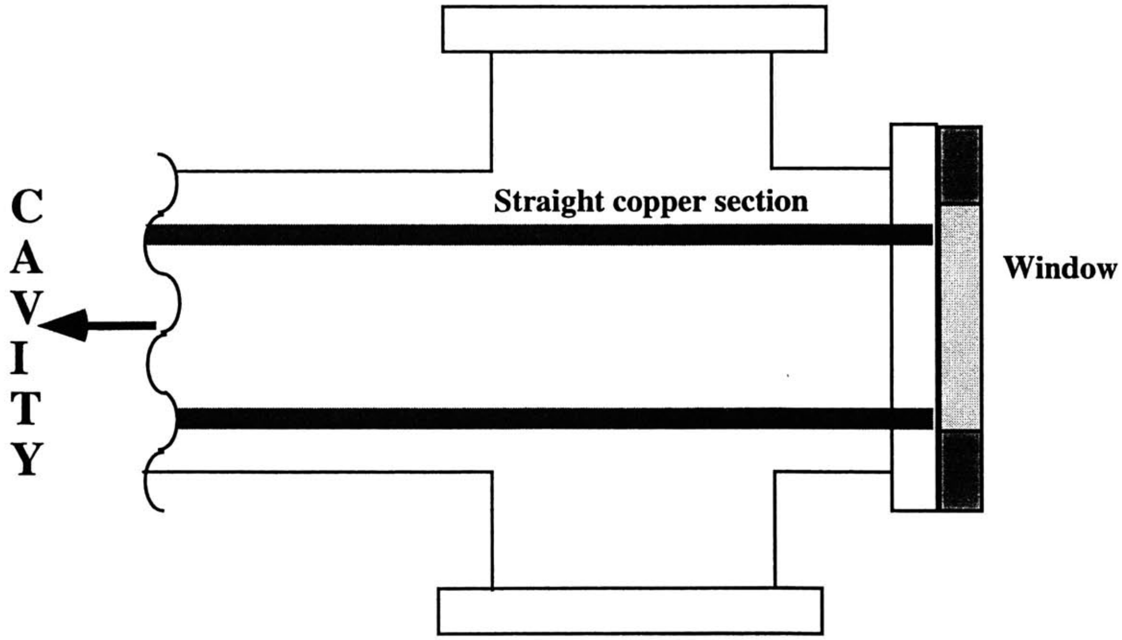

Figure 5.5: Schematic of the empty cavity mode of operation. The coax conductor has been removed, and power is extracted radially.

In this mode of operation we observed microwave power in the frequency range of 135 - 144 GHz. Figure 5.6 shows a plot of the output power and frequency versus the main magnetic field.

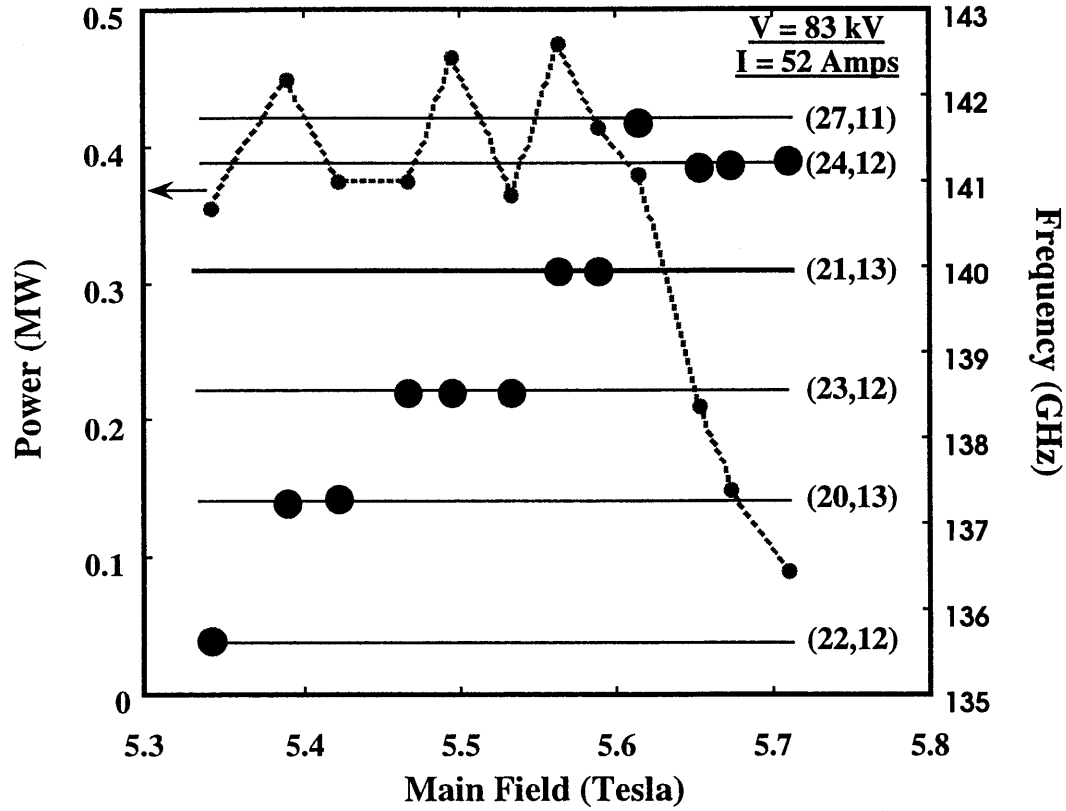

Figure 5.6: Power and frequency versus main magnetic field in the empty cavity mode. The design mode shown above is the $TE_{21,13}$ mode with a frequency of 139.95 GHz (cathode 1).

One can see from the above graph that the maximum power that was observed was about 0.47 MW. One also sees that this maximum power was obtained in the design mode, $TE_{21,13}$, in single mode operation and the efficiency was only 10.9 %. This is quite low in comparison to the prediction that was calculated from single mode theory of an output power of 1.44 MW at 28.9 % efficiency.

We also carefully compared all the experimentally observed modes with the theoretically predicted modes. Figure 5.7 (a) shows a plot of all the theoretically observed modes and experimentally obtained modes. One can see that although there is good agreement between them there are several modes that are not seen experimentally i.e. the TE$_{20,14}$; TE$_{9,18}$; TE$_{17,15}$.

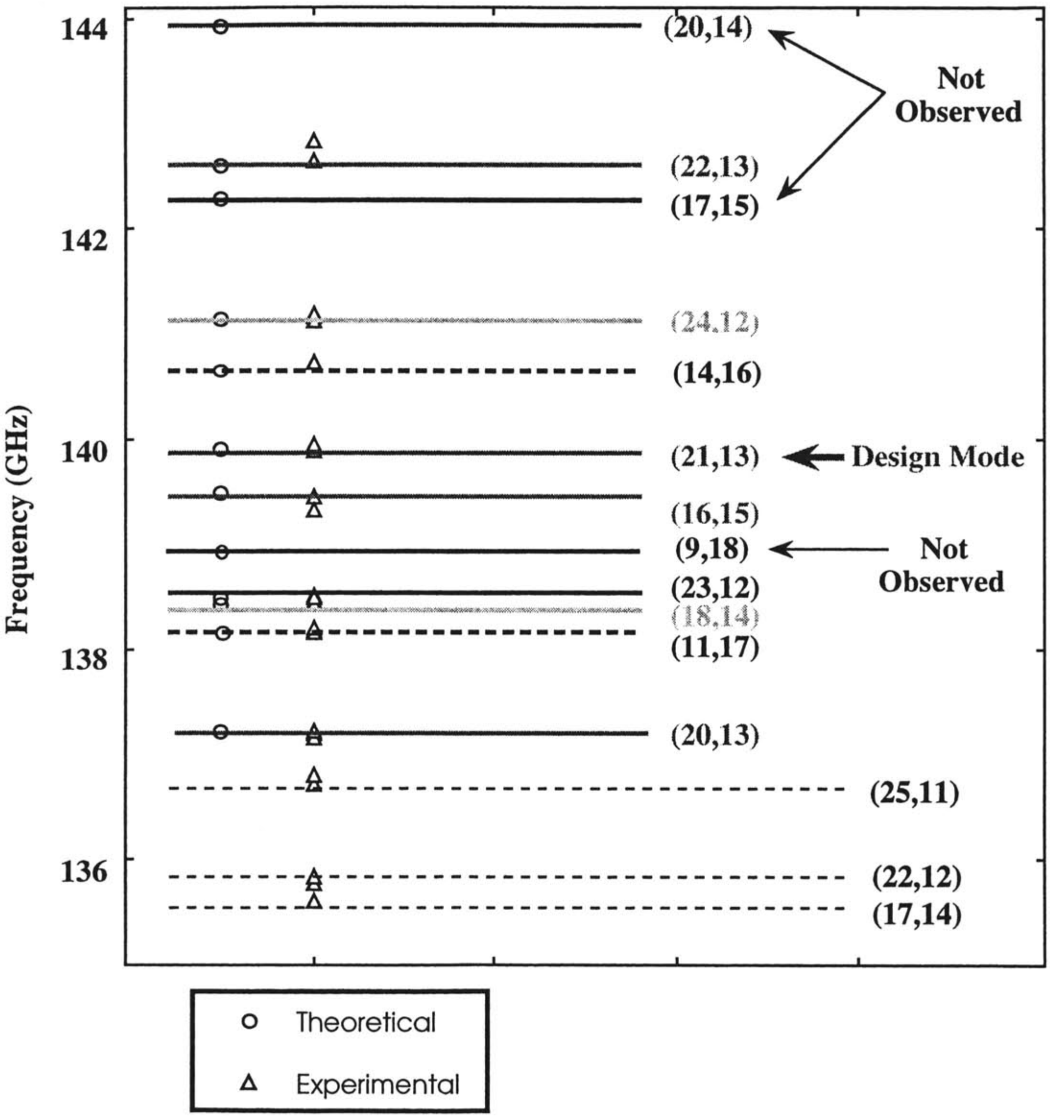

Figure 5.7 (a): Experimentally obtained modes and theoretically expected modes in the empty cavity mode of operation (cathode 1).

Figure 5.7 (b) shows a plot of the coupling coefficient of the modes. One can see from the figure that the modes that were not observed have the lowest coupling coefficients (C_{mp}),

$$C_{mp} = \frac{J^2_{m\pm n}(k_\perp r_b)}{\pi(\chi^2 - m^2)J^2_m(\chi)} \tag{5.1}$$

where $k_\perp$ and r_b are the perpendicular wave number and the beam radius. χ is the eigenvalue, which in our case is 65.

Hence, we see that the agreement between the theoretical and the experimental modes is complete and the modes not observed experimentally are explicable on the basis of low coupling coefficients.

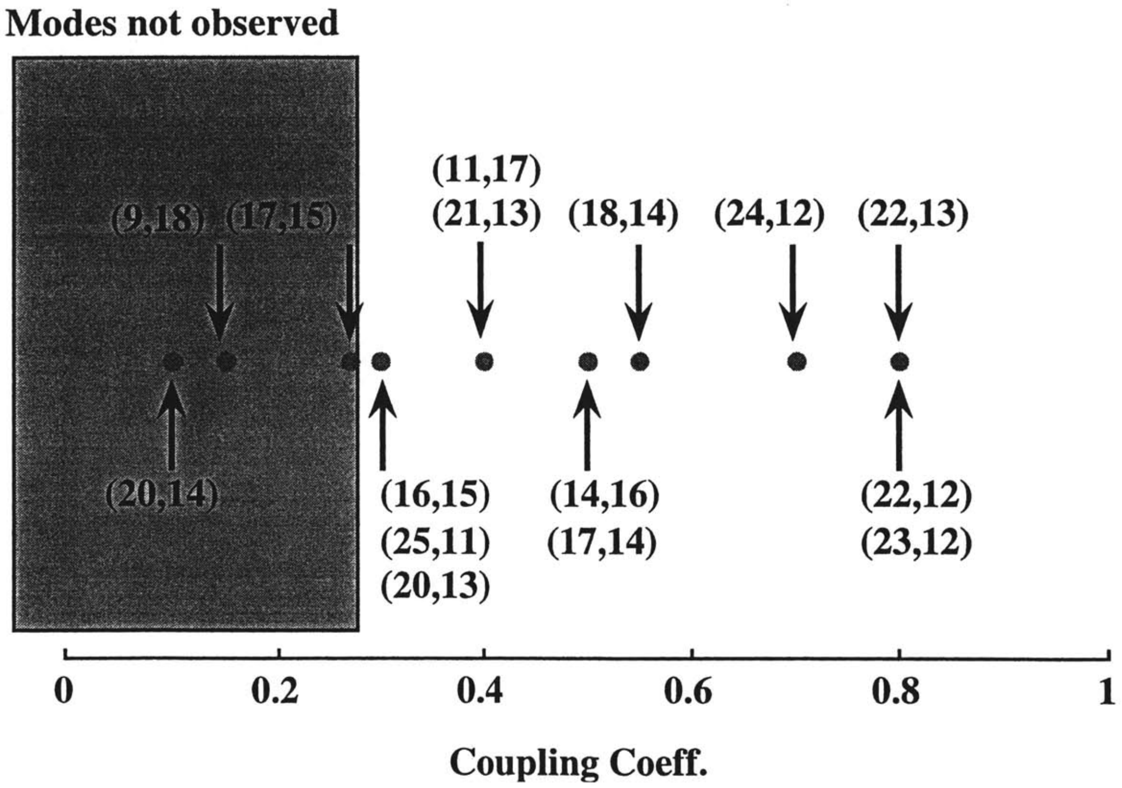

Figure 5.7 (b): Experimentally obtained modes and theoretically expected modes in the empty cavity mode of operation (cathode 1).

In spite of the good agreement between the modes and the frequencies that we observed during the empty cavity runs, we had to acknowledge the fact that the power obtained was relatively low. This caused us to question the quality of the electron beam in the gyrotron. This was then investigated and our suspicions were confirmed regarding the poor azimuthal symmetry of the electron beam (the investigation of the azimuthal symmetry of the electron beam is described in detail in section 5.4). This meant that we would have to replace the cathode with a new one. After the new cathode was installed, we again ran the experiment in the empty cavity mode and obtained better results in terms of power. Figure 5.8 shows a new plot of the power and frequency with respect to the main magnetic field using the new cathode.

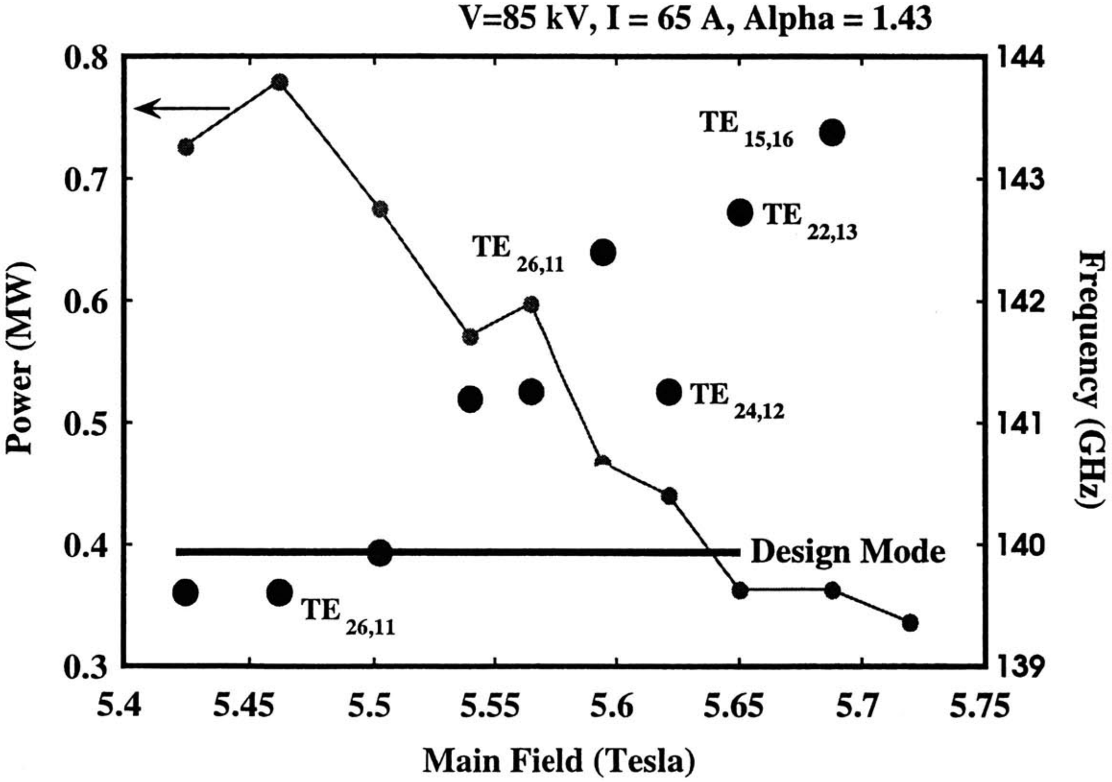

Figure 5.8: Power and frequency with respect to the main magnetic field with the new cathode in the empty cavity mode of operation. Beam parameters V=85 kV, I = 65 A, $\alpha = 1.43$ for entire scan (cathode 2).

From figure 5.8 we see that the dominant mode over a large range was the design mode $TE_{21,13}$ (shown by the dark inverted triangles below) and that although there was some mode competition throughout, there were regions where the design mode dominated all other modes. Figure 5.9 shows the plot of the current and power versus voltage. We have superimposed the theoretical starting current curves and we see that there is considerable agreement between theory and experiment. We see that the design mode is excited in a relatively large range of voltages between 65 kV and 80 kV.

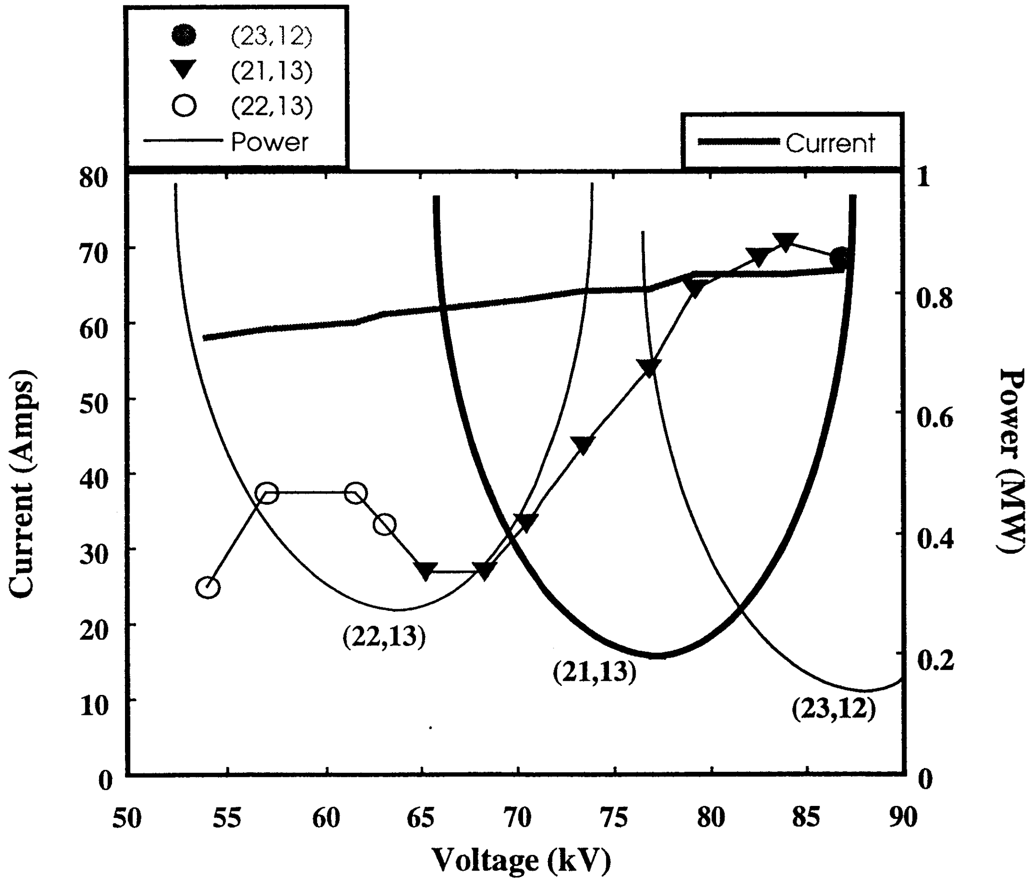

Figure 5.9: Current and power versus voltage during empty cavity operation. The starting current curve for the $TE_{21,13}$ mode is shown in bold (U-shaped curve) while the dots are actually the experimentally measured modes (cathode 2).

Figure 5.10 shows a plot of the alpha scan where the alpha was measured with the velocity probe described in section 2.3.3. Here the voltage was maintained at 85 kV, beam current was 65 Amps, and the main field was held at 5.46 Tesla. The alpha was changed by changing the current in the gun coil (absolute coils). We can see from the plot below that there was a large region where the $TE_{21,13}$ mode was the dominant one. This region is especially interesting because of alpha being between 1.3 and 1.8 (Note: the design alpha was 1.44).

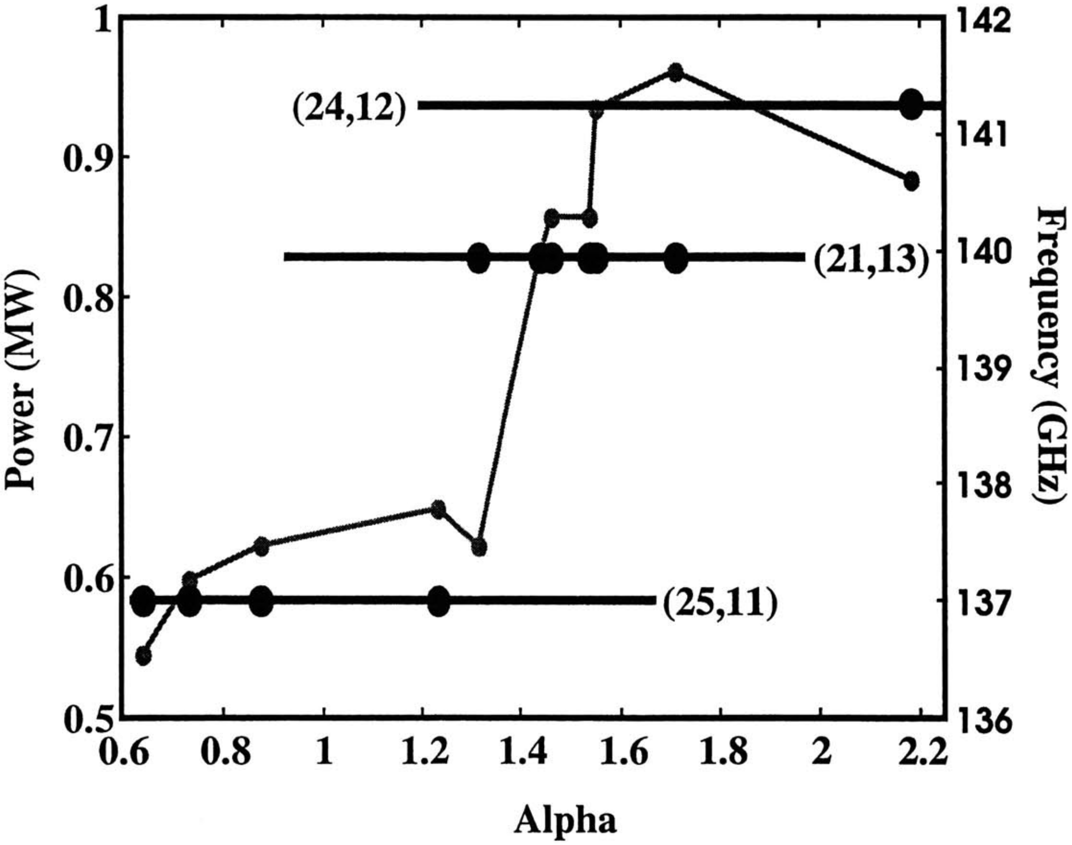

Figure 5.10: Power and frequency observed from the tube as a function of alpha. The alpha was raised using the absolute gun coil. The design mode $TE_{21,13}$ is shown above to be dominant over a large range, which is the reason that this set of data was chosen (cathode 2).

We also took some of the data from the alpha probe as a function of cathode magnetic field and voltage and compared the experimentally obtained alpha with the theoretical ones that can be calculated from EGUN [17] simulations. Figure 5.11 shows a plot of theoretical and experimental alpha's versus cathode magnetic field. Again, one observes relatively good agreement between theory and experiment. The experimentally measured values have a sizable error bar due to the shot-to-shot noise and ringing generated from capacitive coupling in such an electrically noisy environment.

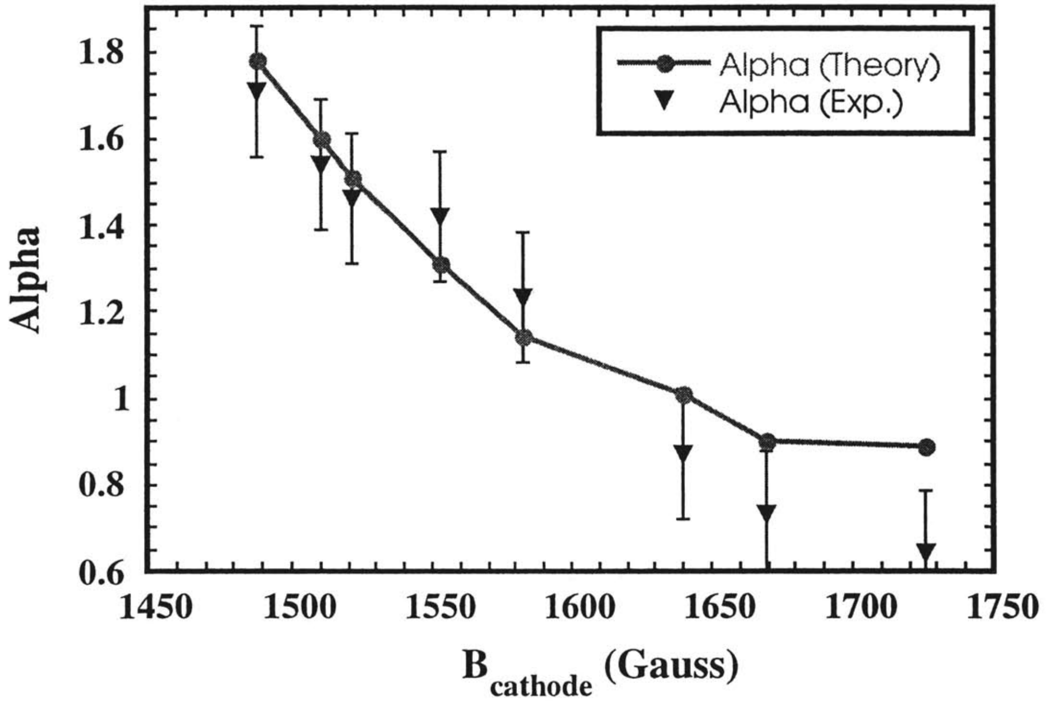

Figure 5.11: Theoretical (EGUN simulations) and experimental values of velocity ratio (alpha) vs. changes in cathode magnetic field. Cathode magnetic field varied using the absolute gun coils (cathode 1).

Figure 5.12 shows a plot of the theoretical and experimental alpha's with respect to a beam voltage scan. Here too, we can see good agreement except for a small discontinuity at 65 kV, which can be attributed to errors due to shot-to-shot noise. Hence, one can conclude that the empty cavity experiments met our expectations for modes observed but we were able to get only 18.7 % efficiency. Yet, the operation helped us identify the problem area in the tube i.e. the electron gun. We now have a good understanding of the modes and the power that we are able to obtain in the empty cavity mode. We also observed improved performance with the new cathode with better beam quality which gave us a maximum power of 1 MW in the design mode (as compared to the of 0.47 MW with the first cathode). The new result of 1 MW power in the empty cavity mode is lower than the theoretically predicted power of 1.44 MW (single mode code) due to the new cathode continuing to have some beam asymmetries (see section 5.4.2). We have 60% variance in azimuthal symmetry while a good cathode should have less than 20% variance, as has been observed in the results of the 170 GHz tube [33].

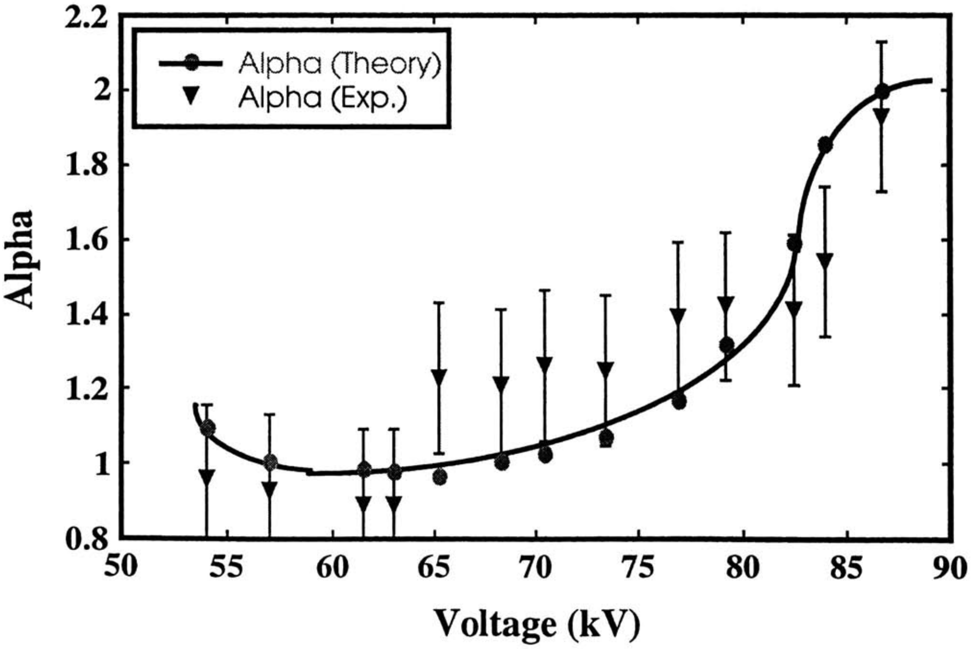

Figure 5.12: Theoretical (EGUN) and experimental values of alpha vs. beam voltage (cathode 1).

5.4 Electron beam – azimuthal symmetry analysis

The co-relation between poor electron beam azimuthal symmetry [84] and low output power in gyrotrons has been observed and studied [82,85]. Glyavin *et al* [82] showed that the increase in inhomogeneity did decrease the power output from the tube, which they were able to show experimentally. The primary reasons for the inhomogeneity not only in beam current but also in velocity spread (which also degrades efficiency in a gyrotron tube) are:

(i) Azimuthal temperature variations of the emitter (beam),

(ii) Differences in emissive coating on the cathode and thus work function (beam),

The effects above introduce an inhomogeneity in the electron beam and leads to differences in emission current density from different parts of the cathode. Thus, for a constant perveance gun, the higher density regions are closer to the space-charge limited regime and have greater velocity spreads than the design values. Hence, when after several runs of the tube (with and without the coaxial conductor), we did not get reasonable output power, we decided to investigate the electron beam that was being used for the tube.

5.4.1 First cathode : Electron beam azimuthal symmetry analysis

(i) Witness-plate measurement

Since we suspected the electron beam to be of poor quality, the first test that we performed was a witness-plate test where we let the electron beam strike a simple copper plate (that we inserted manually). We made sure that the target was in the region of the cavity so that we could not only measure the beam symmetry but also the radius of the electron beam and compare it to the theoretical design value. Hence, we inserted the copper target and ran at a modest 30 Amps beam current at 30 kV (because full power would cause arcing and poor pressure which would harm the cathode emitter). We ran 20 shots of ~ 4 μs at 1 Hz and then ran another 20 shots after a few hours (because the pressure was getting quite high after the first 20 shots and we had to wait for the pressure to improve). The image of the witness plate with the impression of the beam is shown in Figure 5.14. Using a microscope we then measured the width at 12 points around the circular image, at ~ 30° intervals. This data is plotted in figure 5.13. The beam radius was measured to be 8.1 mm which agreed fairly well with the EGUN predictions of a beam radius of 8.2 mm. We also noted that although we had expected the beam to be aligned with the tube and thus centered on the witness plate it was displaced by 1.13 mm toward one side, which meant the beam was misaligned.

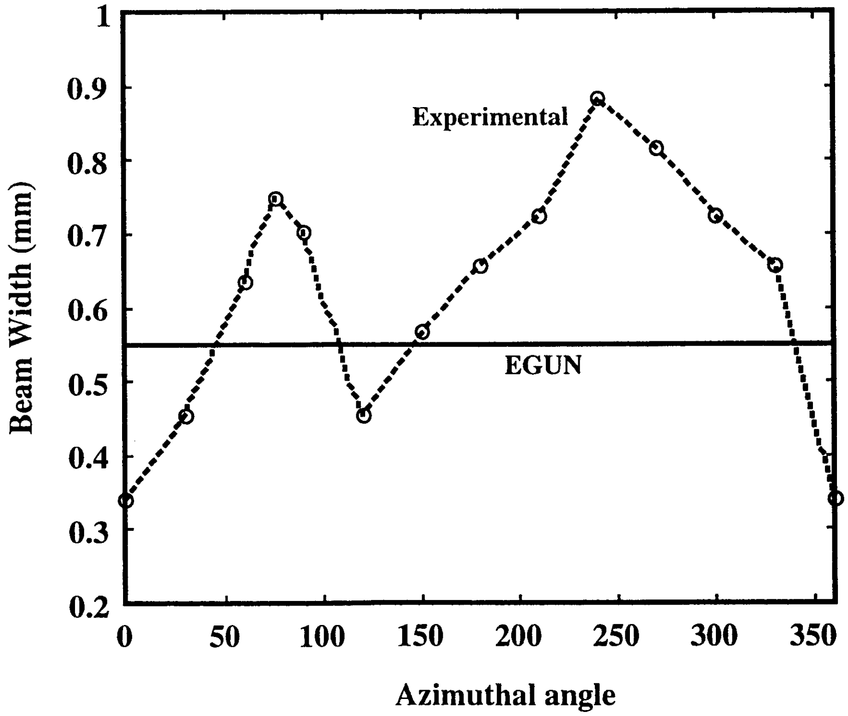

Figure 5.13: Beam width measured versus azimuthal angle. 0° in all our measurements is where the heater lead enters the cathode housing (cathode 1).

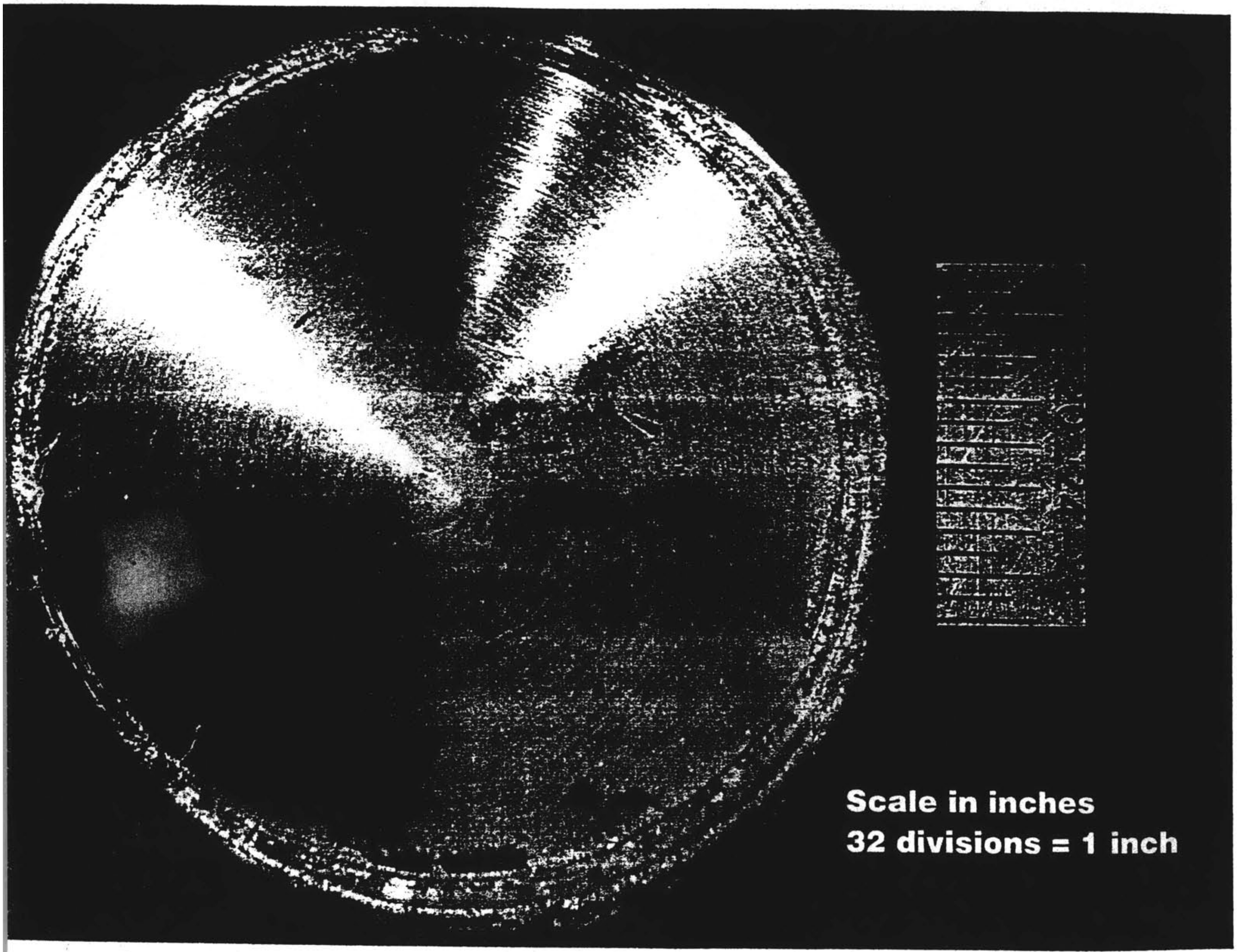

Figure 5.14: Scan of an electronic microscope image of the witness plate used for the electron beam asymmetry measurement (cathode 1).

The measurements in figure 5.13 and 5.14 clearly show that there are large asymmetries and there seems to be a double hump structure. The weak emission spots seem to be at 0° and 100° while the strong emission spot seems to be ~ 240° to 260°. This data certainly confirmed our suspicions that the beam had large asymmetries but could not tell us the exact difference in emission densities (because the beam impression in copper can be non-linear). Hence, we decided to measure the beam current directly as a function of azimuthal angle.

(ii) Rotating-probe measurement

The rotating probe experiment consisted of a 30° sector, which could be rotated from outside the tube with a rotary feed-through. The sector had a hood in order to ensure that the entire beam in a sector was being collected. The rotating probe assembly is shown in figure 2.3. Thus, we had measurements coming from this 30° sector as well as the rest of the 330° which was measured at the collector as usual. Thus, after the rotating probe apparatus was inserted the beam and the tube were aligned and the data obtained is plotted in figure 5.15. 0° to 360° is the same as in other beam measurement experiments. One can see a general agreement in the data shown in current distribution of figure 5.14 and 5.15. There is a double hump structure with the lowest current density spot at ~ 0° and 100° while the highest current density at ~ 250°. All these experiments were run with total beam currents of 5-30 Amps and at voltages up to 40 kV, again because we wanted to prevent arcing, poor pressure in the tube, and oscillations from being excited in the tube.

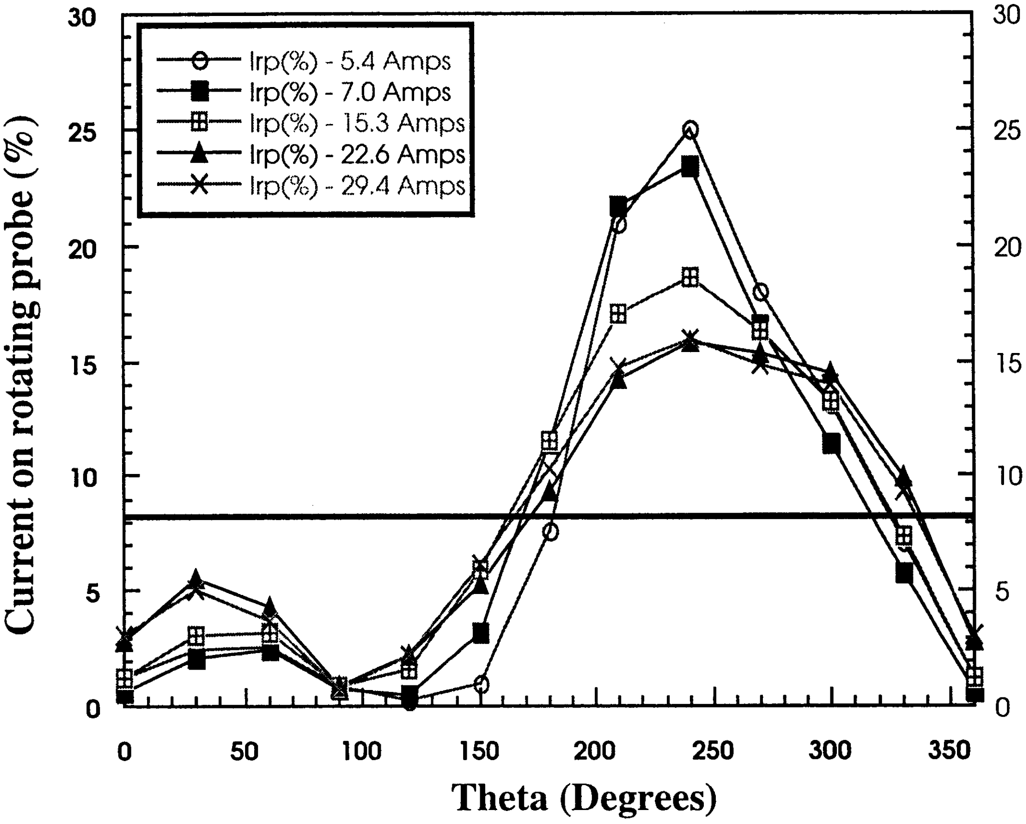

Figure 5.15: Normalized beam current vs. azimuthal angle. Beam current at any angle is normalized to the average total current - sector + collector (cathode 1).

(iii) Temperature measurement

A final test of the cathode was made with a temperature measurement of the cathode in order to confirm that that was the source of the differences in current emission from different parts of the cathode. The cathode was kept on a stand inside a bell jar which maintained vacuum at ~ 10^{-7} Torr. Heater current was then provided to the cathode and measurements were made with an optical pyrometer of the temperature at various azimuthal angles. For a schematic of the setup see figure 2.4. Figure 5.16 shows a plot of the temperature versus azimuthal angle for four different power levels. One notes from the plot that the hottest point is around 250° and the coldest point is at 0°. The difference in temperature between the hottest point and the coldest point for the 428 W, 500 W, and 562 W was approximately 50°C.

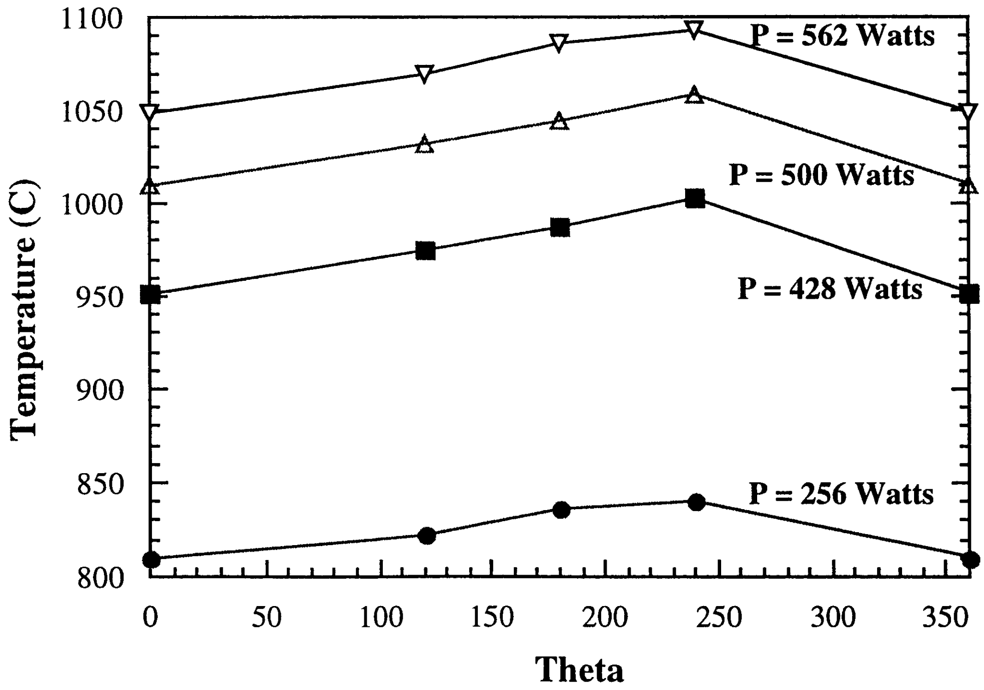

Figure 5.16: Temperature versus azimuthal angle for four different power levels. The temperature was measured with an optical pyrometer whose range was 750°C to 1300°C (cathode 1).

Using the temperature data and an emission curve for the M-type thermionic cathode we are using (published by the manufacturer of the cathode – Spectramat [32]) we are able to generate Figure 5.17, which shows emission density as a function of azimuthal angle. This curve also shows the qualitative result that the lowest and the highest emission spots are aligned with those measured from other techniques.

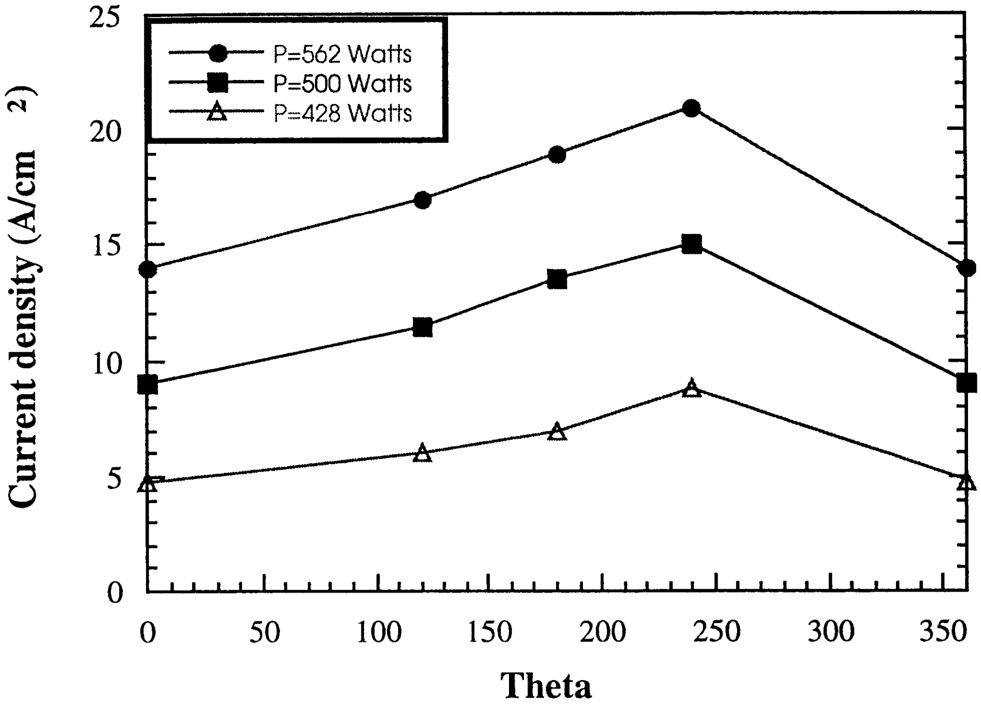

Figure 5.17: Calculated emission density versus azimuthal angle. The emission density was gleaned from the manufacturer data on emission density vs. temperature for this cathode [32] (cathode 1).

An analysis was done of the temperature based measurements with those from the rotating probe measurements. Figure 5.18 shows the data where one can see that there is qualitative agreement between the azimuthal angle for the hot spot and the cold spot measured from the two techniques. The temperature data does not explain as large a current density variation as observed from the rotating probe measurements. This is because the measurement does not take into account the effects of variation in emissive coating on the cathode or the space charge limits at the high current density spots. A error in angle (of order ± 5°) that could also have been introduced due to the physical constraints of not having a marked table with repeatable angle positions during the temperature measurements. Nevertheless, the case is complete that the cathode in question has poor beam azimuthal symmetry a substantial part of it is due to temperature variations. Other effects that add to the asymmetry are the emissive coating differences on the emitter and damage of the thermal insulation between the emitter and the cathode holding structure.

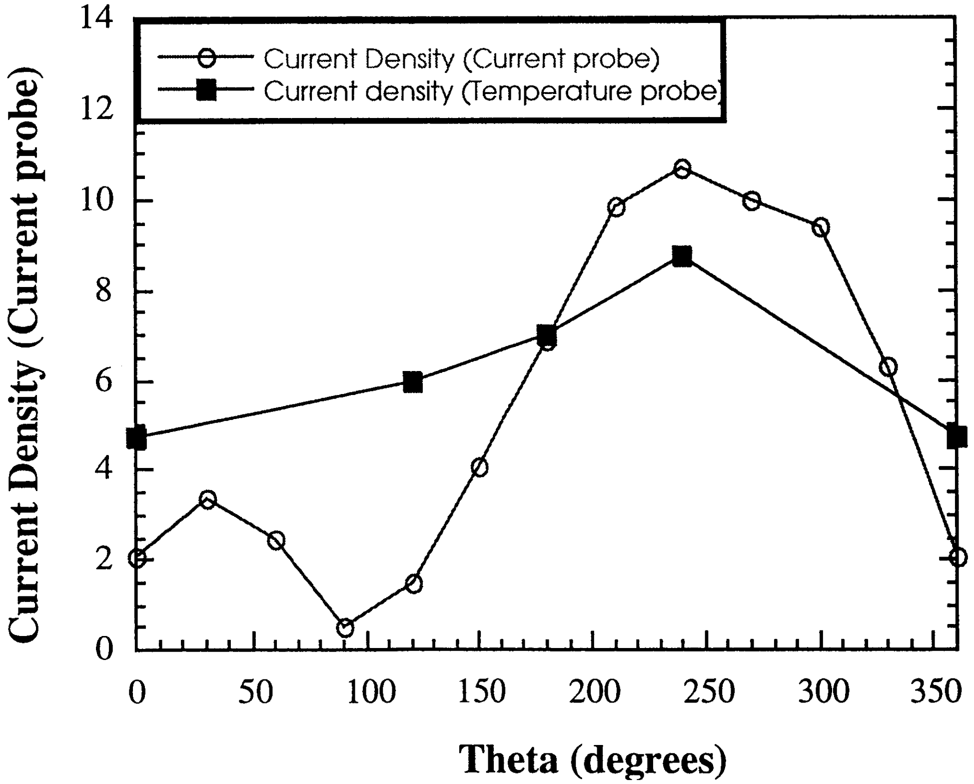

Figure 5.18: Comparison of emission density versus azimuthal angle for two different techniques. The temperature measurements are shown by the solid squares while the hollow dots show the rotating probe measurements (cathode 1).

5.4.2 Second cathode - Electron beam azimuthal symmetry analysis

Upon realizing the poor electron beam symmetry of the first cathode we decided to replace that one with a spare second cathode that we had. This was a fairly complicated task since the cathode is surrounded by an oil chamber, supports, and one welded connection. This is then surrounded by magnetic gun coils and a support frame. The entire structure is over 300 kilograms and has to be handled by cranes. Regardless, we took apart the gun and replaced the cathode. Once the new cathode was in place we once again examined its electron beam azimuthal symmetry using the rotating probe apparatus. Figure 5.19 shows a plot of the normalized current on the rotating probe with respect to the azimuthal angle for three different voltages, heater power was held constant at 540 W.

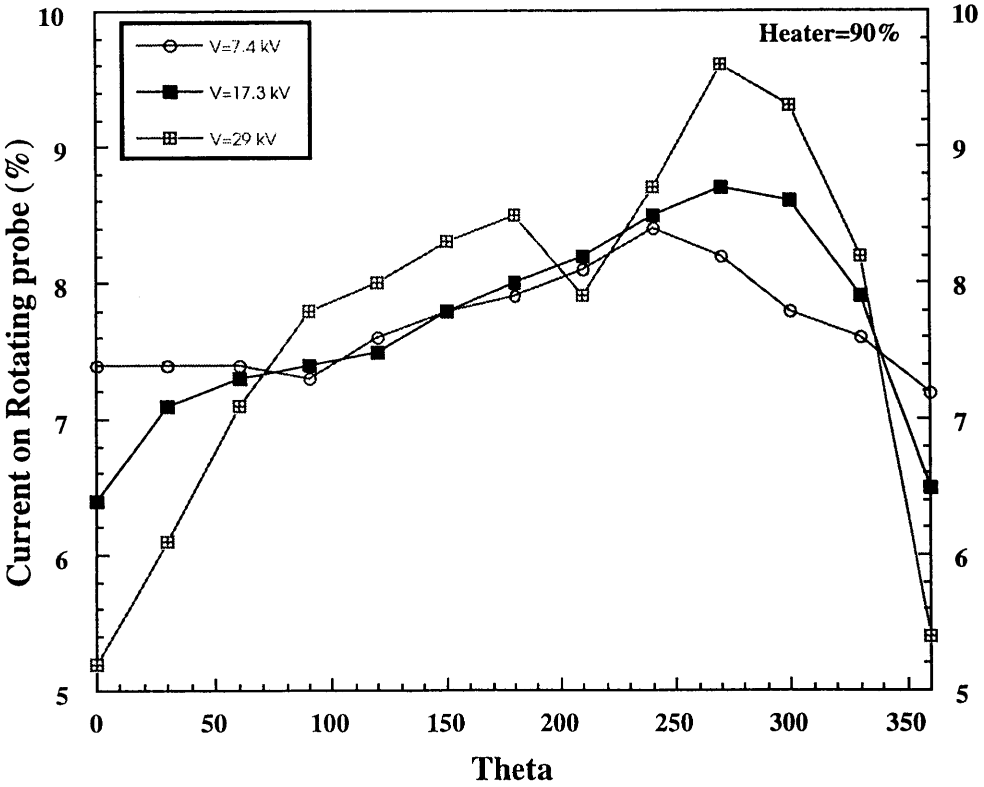

Figure 5.19: Normalized current on rotating probe versus azimuthal angle for the second cathode. Data for three different accelerating voltages is shown (cathode 1).

Figure 5.20 shows a plot of current on rotating probe versus theta for four heater levels. The voltage was held constant at 17.3 kV because we did not want to excite oscillations inside the tube, which would have impeded the measurement.

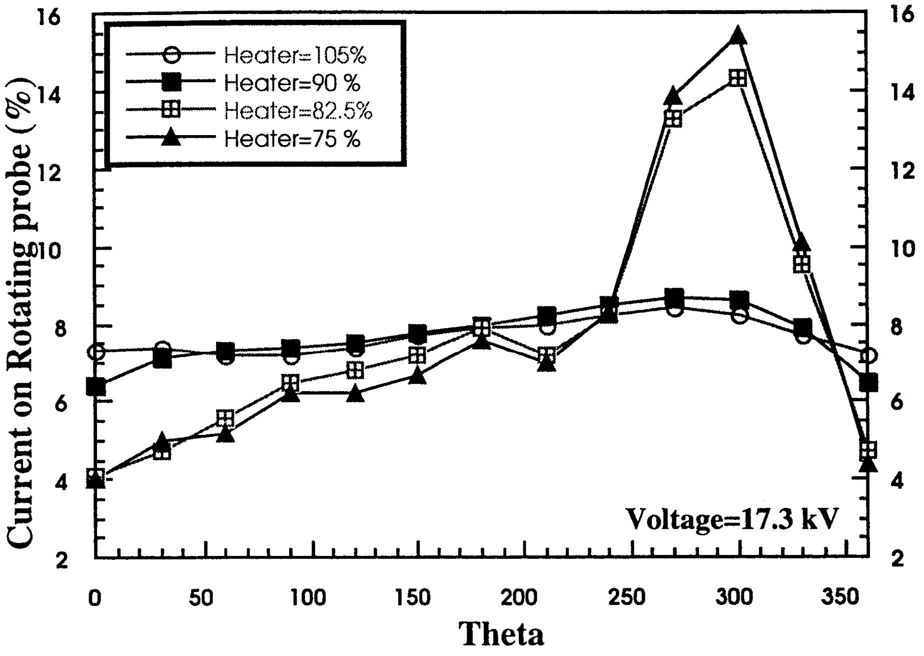

Figure 5.20: Normalized current on rotating probe versus azimuthal angle for the second cathode. Data for four different heater levels is shown (cathode 2).

Finally, figure 5.21 shows a plot of the variation levels versus voltage for four heater levels. The variation is defined as the (maximum current – minimum current) and is normalized to the average current level of any set of data. Thus, this variation was calculated for all the sets of data taken and was plotted in figure 5.21. One can see from the plot that the lower the heater (temperature limited regime) the larger are the variations; and at higher heater levels (more space-charge limited) the variations become smaller. Also, higher voltages lead to greater variation, again due to the emission mode moving away from the space charge limited regime. Hence, at 95 kV, we probably always have a asymmetric beam. The highest variation observed is quite high at ~ 60%, but is low in comparison to the ~ 150% variation of the first cathode.

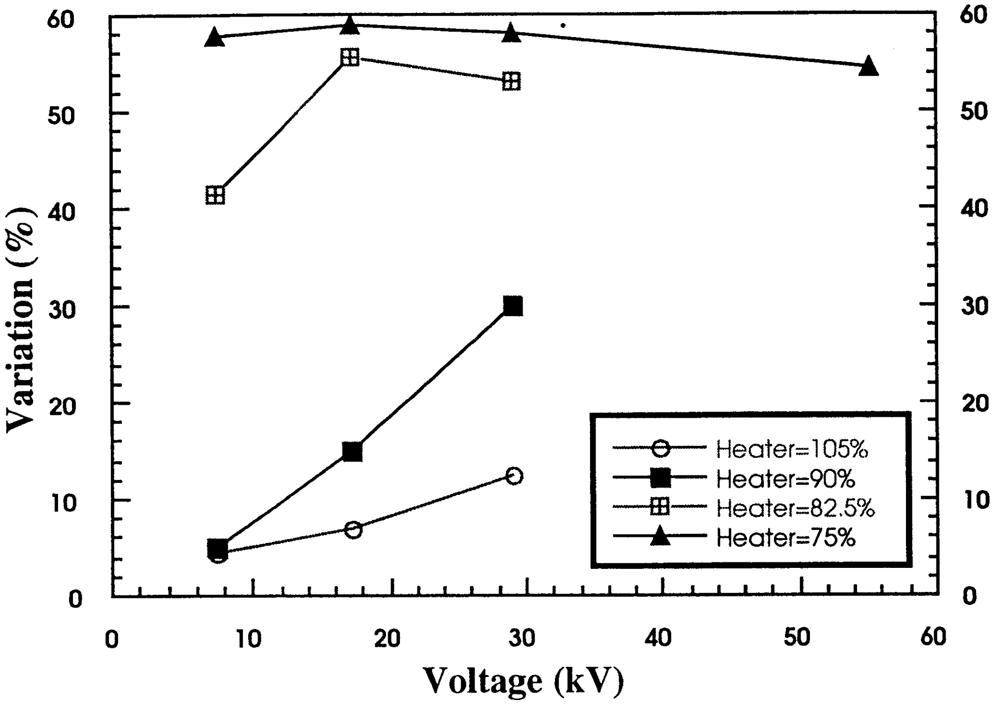

Figure 5.21: Variation of the current density vs. voltage for four heater levels (cathode 2).

Thus, one may conclude that although the second cathode too has reasonable beam asymmetries (~60% variance as compared to the ~150% for the first cathode), it is yet quite a bit better than the first cathode. This fact is borne out also in the fact that the second cathode had substantially better power output than the first one. The maximum power output from the first was 0.47 MW and the second cathode was 1.03 MW in the empty cavity mode. In the mode with a coaxial insert we were hopeful that the second cathode would provide more output power and that we would have good results from it. Unfortunately, there was a catastrophic failure of the window at the output end due to movement of the inner conductor, which shattered the window. This happened as the second cathode had been energized and thus completely oxidized and thus ruined the cathode. We tried to revive the cathode by flowing 3 % hydrogen gas over this cathode in order to reduce the oxidization of the cathode but were unable to obtain any current from it. Hence, we once again had to reopen the entire gun and put back the first cathode. This time though we ran in the axial output mode and investigated the mode structure of the tube in this mode. The breakage of the window in the earlier case was caused due an unexpected effect of the slight magnetization of 304 stainless steel due to machining stresses. This caused the magnetic rod to move when the main magnetic field was raised. The largest section of the coaxial conductor that had been slightly magnetized due to machining has been replaced with a copper section, which is non-magnetic and held securely. We tried to de-magnetize the coaxial conductor by heating the rod to 1200°F and then quickly quenching it – but failed to remove the magnetization. Hence, one of the sections of the coaxial conductor was re-machined using copper.

5.5 Coaxial conductor with axial power output mode

The final set of experiments that we performed with the coaxial gyrotron was with the coaxial conductor inserted and the power extracted axially as shown in the schematic in figure 5.22. We performed these runs in order to investigate the power, the modes, and the alpha. We wanted to find the basic mode competition characteristics of the coaxial gyrotron. The cathode used in the electron gun was the first one whose azimuthal current characteristics are shown in figure 5.16. Hence, we were using the cathode with poor azimuthal symmetry but were hoping to understand enough of the mode competition issues in the coaxial gyrotron to be able to make future plans for this tube. The support shown in figure 5.22 is made from an insulator (Macor) and is very marginally absorbent of microwave power.

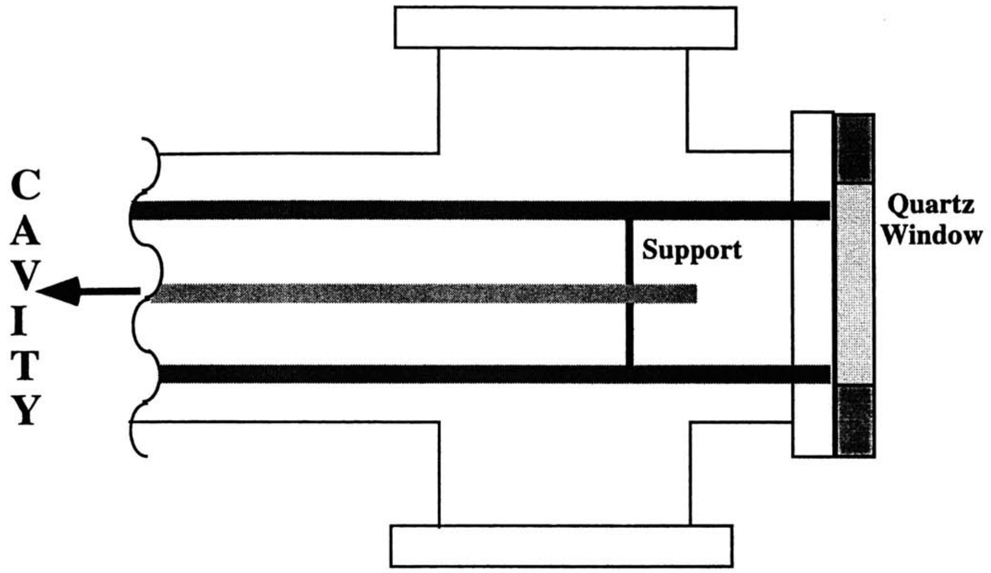

Figure 5.22: Schematic of runs with the coaxial conductor inserted and axial power extraction from the quartz window.

In this mode the gyrotron was usually operated at reduced current of 45 Amps at 90-95 kV, because we were unable to get to the full current even after a two weeks of continuos heating at full heater power. In spite of the low current, we were able to transport the beam from the gun to the collector without interception, and microwaves were generated in the 135 – 145 GHz range. During the operation, we found that when we raised alpha above $\alpha \approx 1.2\text{-}1.3$ we started getting reflected electrons. Nevertheless, Figure 5.23 shows the result of the power obtained versus the main magnetic field. The plot also shows the dominant modes that were observed at each of the points of operation. The solid line shows the power while the dots show the frequencies (and thus modes) observed. The solid dots show the dominant modes while the hollow dots show the weak ones. Experimentally, we saw mode competition and that the design mode was observed over a substantial part of the magnetic field scanned.

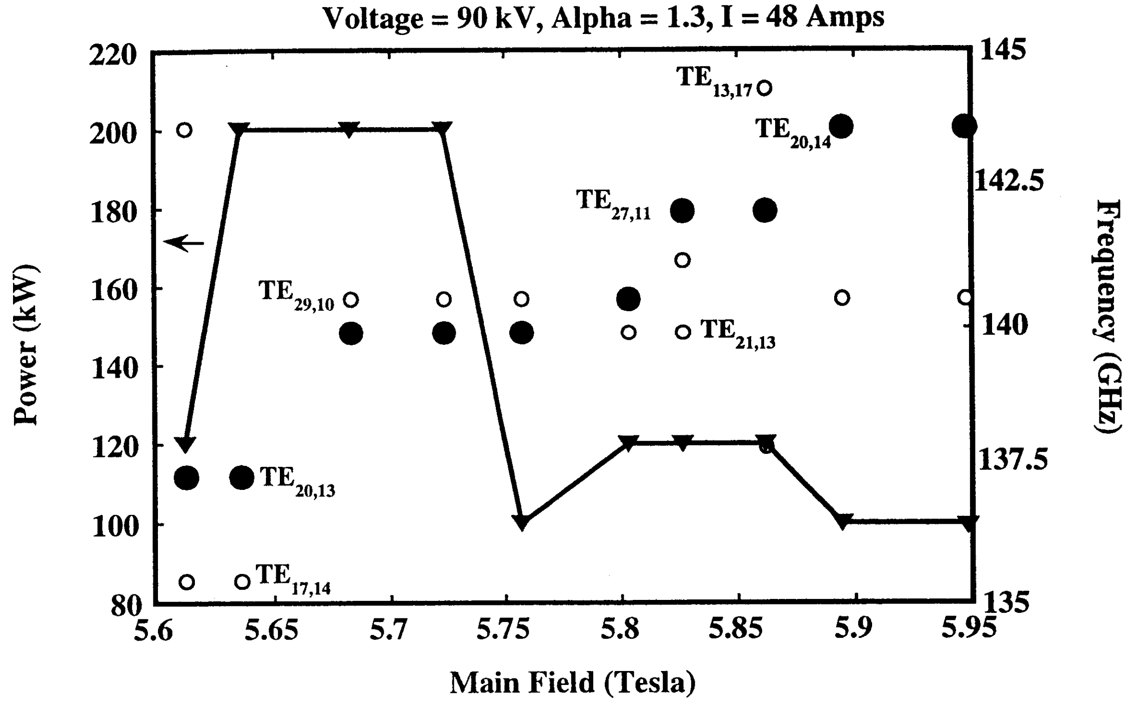

Figure 5.23: Output power (curve) and frequency/modes (points) versus the main magnetic field in the axial output mode with coaxial conductor (cathode 1).

In the magnetic field scan above, we see that although the modes observed are ones that one can expect, there is significant mode competition. We also see that the total power obtained is fairly low and is lower than the 300 kW that one had obtained earlier with this cathode in the same mode for the current level of 45-50 Amps (as seen in Figure 5.3). One can note that this scan was taken at an alpha of 1.3 with the beam voltage maintained at 90 kV.

Another result that was obtained was the scan versus voltage, which are shown in Figure 5.24 and 5.25. Figure 5.24 shows the entire scan and the various modes obtained. The current that we operated at was 47 Amps, alpha ~ 1.2. Again we observe significant mode competition. The dark dots represent dominant modes while the hollow ones represent weak modes.

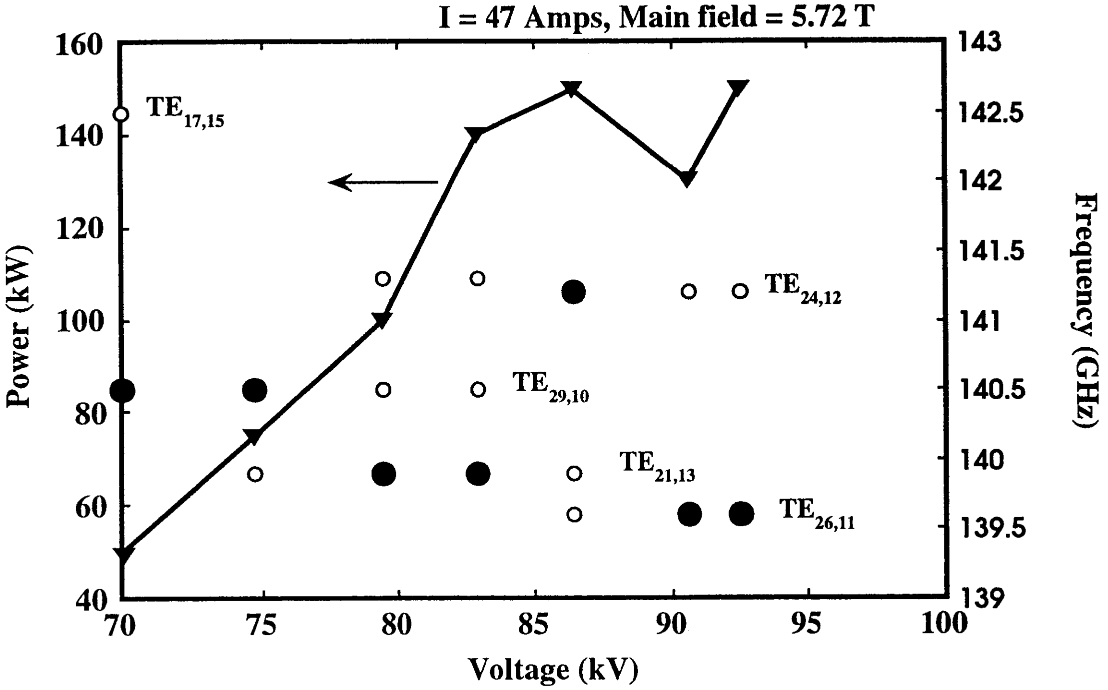

Figure 5.24: Output power and modes versus beam voltage in the axial mode of operation with the coaxial conductor (cathode 1).

In Figure 5.25, we plot the most dominant modes along with the current and the theoretical starting current curves for the modes. We see that there is agreement between theory and experiment in terms of the voltage ranges where one expects the dominant modes. The final scan that we performed was to investigate power and modes versus changes in alpha, shown in Figure 5.26. This was done by keeping the beam voltage, beam current, and main magnetic field constant, while changing the current in the *absolute gun coil* in order to change the field at the cathode and thus the alpha.

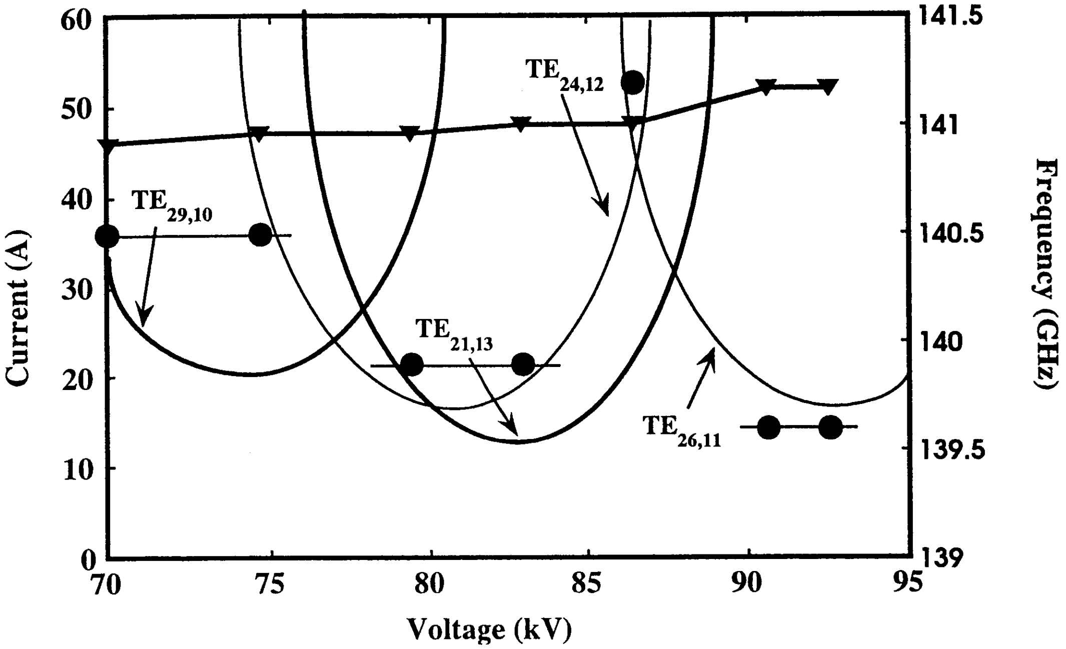

Figure 5.25: Dominant modes, their theoretical starting currents, and beam current vs. voltage (cathode 1).

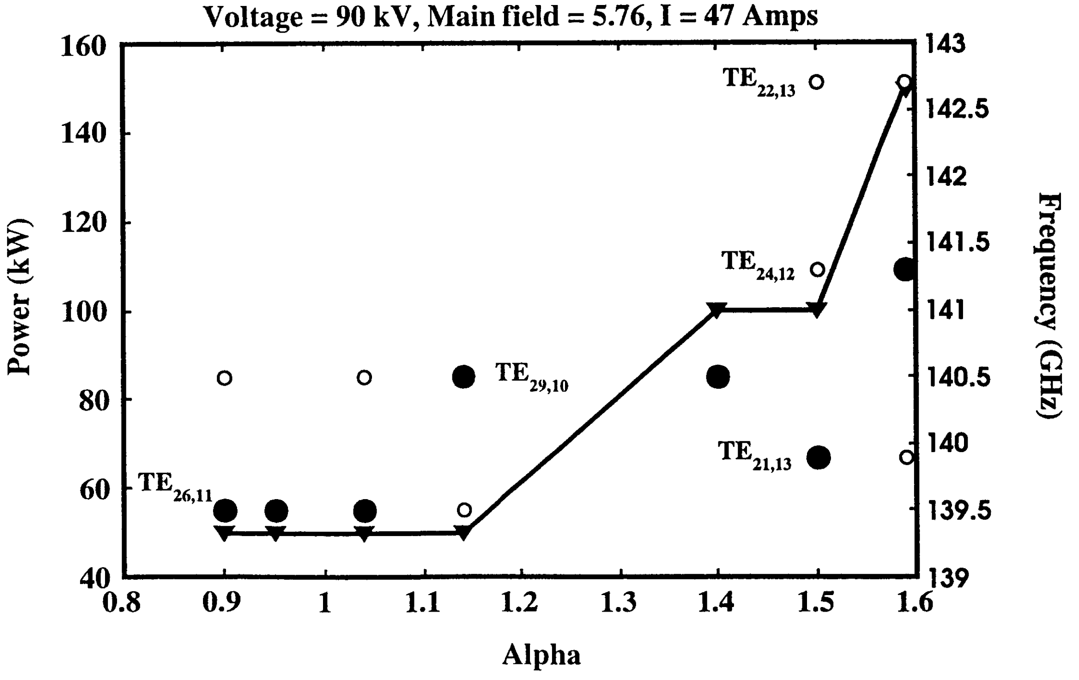

Figure 5.26: Scan of power and frequencies/modes vs. alpha -axial output with coax conductor (cathode 1).

The final set of data that we took was to investigate the modes and frequencies in this coaxial gyrotron with a mode map. This map basically has the main magnetic field on one axis and alpha on the other. One can then take any mode and map out exactly where it starts and ends in this 2-D space. Changing the cathode magnetic field varied the alpha. Varying the cavity field also allows one to change the cyclotron frequency of the electron beam, hence optimizing the detuning parameter. Each of these modes therefore occupies a certain area on the map as shown below in Figure 5.27. If there is little or no multi-moding then the area enclosed by one mode is not overlapped with the area enclosed by another mode. We did not get such operation, and actually observed significant multi-mode operation. The modes to the left of the graph appear to be single-mode, but they are not, since other modes in that area have not been plotted.

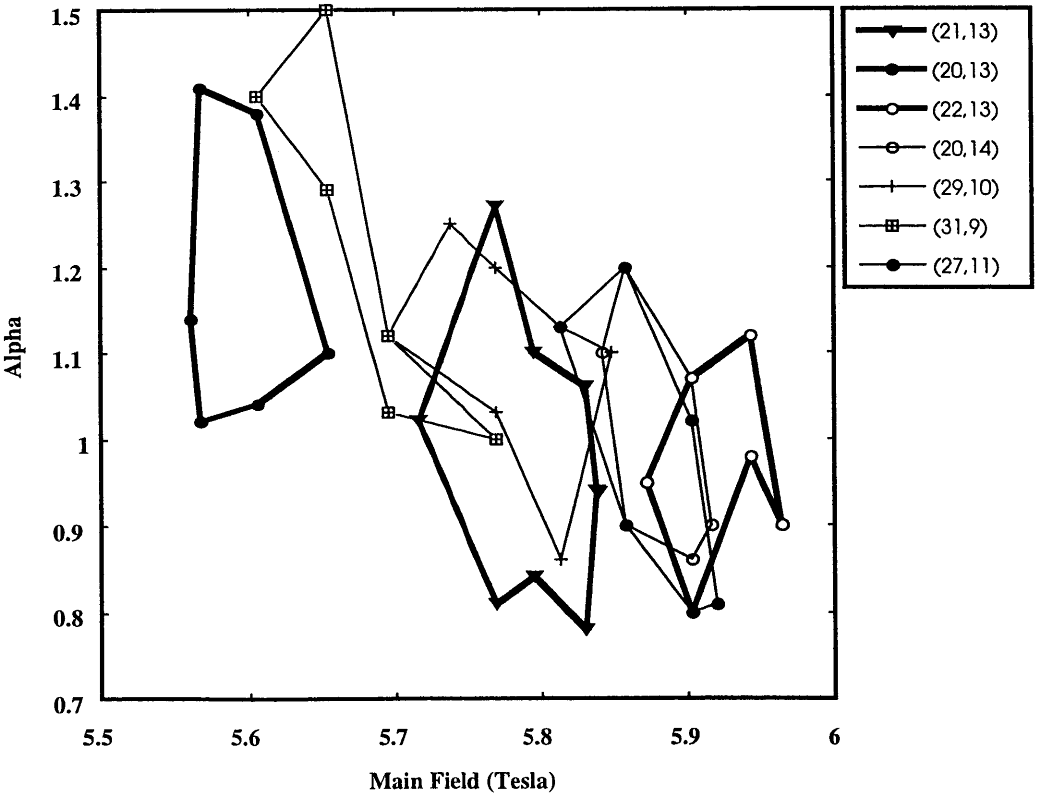

Figure 5.27: Mode map of the various modes obtained during operation in the axial output configuration with the coaxial conductor inserted (cathode 1).

Experimentally, it was observed that if we increased alpha above 1.2-1.3 we saw reflection of the electrons, interception of some of the beam current, and even some beam disruptions. Another noteworthy feature of these runs was that the maximum power obtained was quite low at 0.24 MW at an efficiency of 6.2 %.

5.5.1 Effects of beam asymmetry on tube performance

To understand these result we did some theoretical studies using EGUN to investigate the alpha and the velocity spread and alpha of the beam versus beam current density. In these studies we were trying to understand the implications of 2-3 times the current density (which can be expected at the hot spots with high current density as seen in Figure 5.15) on the operation of the tube. One can also argue that these hot spots actually carry most of the current in the gyrotron and hence dominate the behavior of the tube. With this in mind, we investigated regimes in EGUN, which would be similar to having 2-3 times the operating current for a two-dimensional code. We also investigated the effect of velocity spread on efficiency with the single mode code, which would help us explain the low efficiencies that we were getting from the tube.

Velocity Spread: Figure 5.28 shows a plot of the velocity spread versus operating current. The alpha was maintained at a low value in these runs (below $\alpha\sim0.8$) in order to keep the beam from reflecting. One sees that even at a low alpha of 0.8, once one gets above 2.5 times the operating current (or operating current density), the velocity spread starts to increase rather rapidly. Thus, at high current densities (over 2.5 times operating current) and high alphas (above $\alpha\sim1$) the perpendicular velocity spread increases to above 25 % and parallel velocity spread increases above 10%.

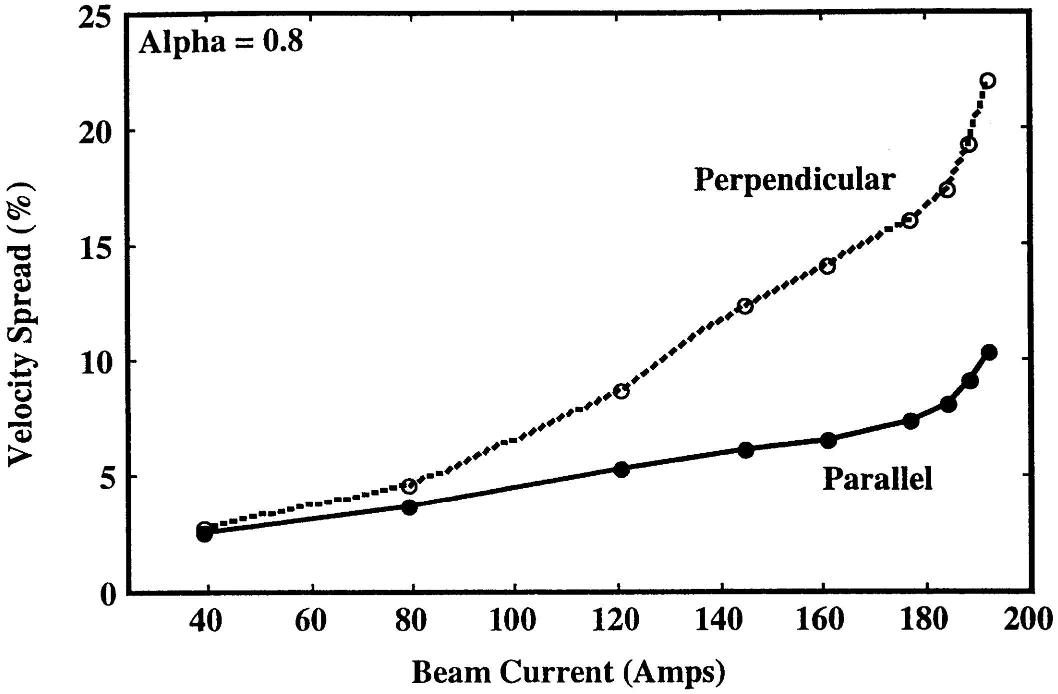

Figure 5.28: Simulated values (EGUN) of perpendicular and parallel velocity spread versus beam current.

Reflection alpha: A plot of the maximum alpha versus operating current, maximum being defined as the point after which we saw reflection of the electrons, is shown in Figure 5.29. One observes that in order to see reflection at an alpha of 1.2–1.3, one would need the hot spots to have a current density equivalent to ~180 Amps, which for a 50 Amp beam current gives us a factor of 3.6 times the operating current density. This is clearly not far from the 3.2 times operating current density measured at the hot spot by the rotating probe test for this cathode (in Figure 5.15). The agreement is even better once one recognizes the fact that the 3.2 factor measured by the rotating probe is almost certain to be worse for a 50 Amp level than the 29 Amp level that it was measured for.

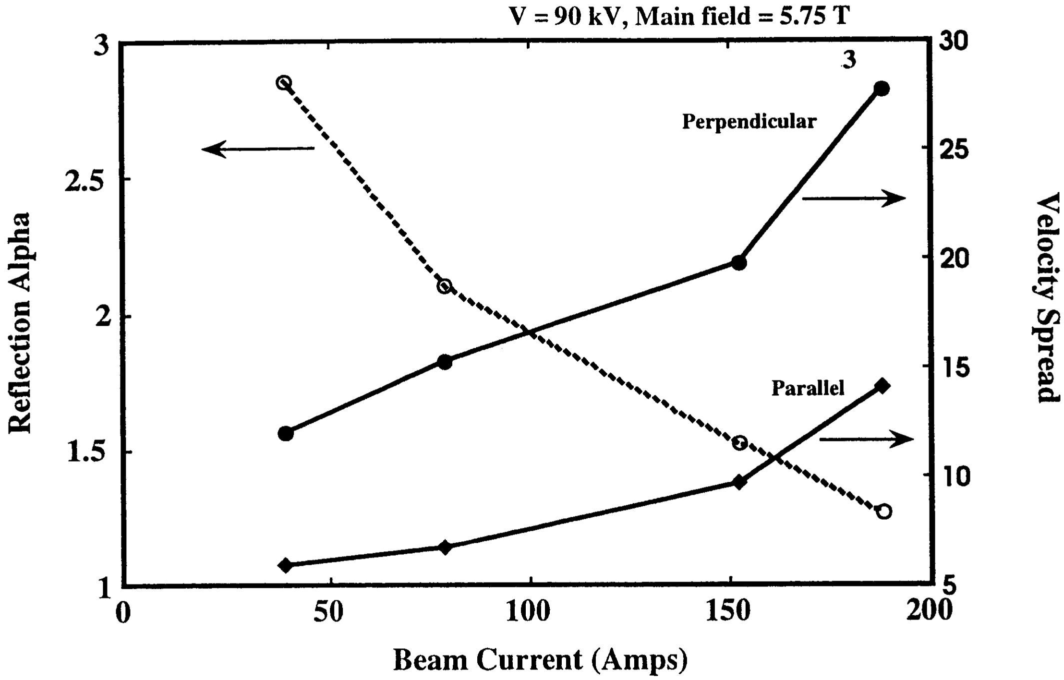

Figure 5.29: Simulated values (EGUN) maximum reflection alpha versus beam current.

Efficiency degradation: One can conclude that enhanced current density due to asymmetries leads to high levels of velocity spread. It is a well-known fact that velocity and energy spread lead to a decrease in efficiency, and this has been demonstrated theoretically and experimentally [34,85,88]. High velocity spread as well as energy spreads have recently also been analyzed theoretically [88] and have been shown to substantially decrease efficiency. Hence, a calculation for this tube was made using the results of Ref. 88, and it was found that one can expect efficiency to decreases to half its initial value with a perpendicular velocity spread of only 20% (which is lower than our estimate, using EGUN, of above 25% velocity spread for a 50 Amp beam). Energy spread has been shown to have an even more dramatic effect on the efficiency where one can expect a decrease by a factor of 1.28 for an energy spread of 1% [88]. Note that, energy spread can be expected with this asymmetric beam due to the higher voltage depressions on the higher current density side of the beam as compared to the lower current density side. Thus, the higher current density side of the beam experiences higher voltage depression and has lower energy.

The severe mode competition in this tube is evident from the mode map shown in Figure 5.27. Azimuthal mode competition can be seen here in the switching of modes between the $TE_{20,13}$, the design mode $TE_{21,13}$, and the $TE_{22,13}$ mode. It is likely that this azimuthal mode competition further decreases the efficiency [also seen in Refs 34,85,89].

Another effect that has been observed in this tube is that as the current is increased, the efficiency increases initially and then saturates or even decreases. This is an effect that has been previously observed in a tube with a similar asymmetric beam [34,85] and is consistent with the velocity spread increasing rapidly as the total beam current is increased. This causes the current density and velocity spread to reach high values at the high emission density parts of the cathode.

Single mode code: Finally, the single mode code was used again in order to quantitatively determine the effect of velocity spread on predicted efficiency. Upon running this code at several different alphas and velocity spreads for the $TE_{21,13}$ mode, we found that indeed the efficiency predicted did decrease by a factor of ~2.2 for a alpha of 1.1 and 24% perpendicular velocity spread, as compared to a case with a 4 % velocity spread (beam current of 45 Amps, and voltage of 90 kV). The 4% spread is the most relevant reference since it is the design value of spread. It is also noteworthy that at 24% spread we find the efficiency has dropped to 12.35% due to nhanced velocity spread alone. Figure 5.30 shows a plot of the expected efficiency versus velocity spread from the single mode code.

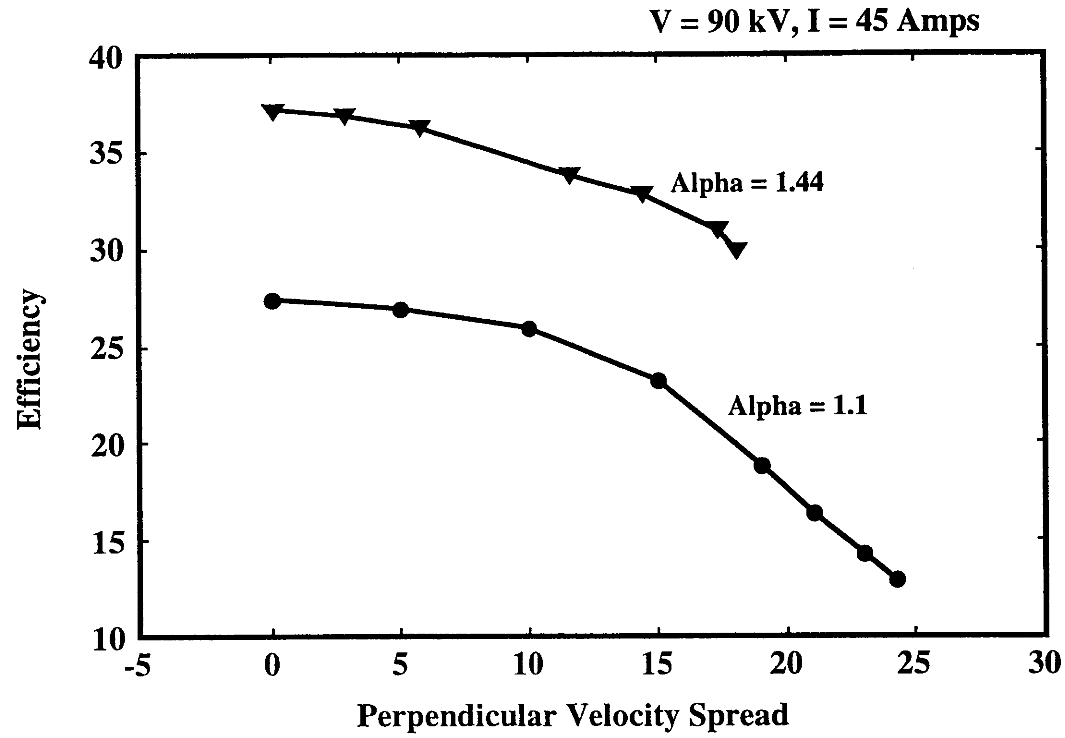

Figure 5.30: Simulated values of efficiency (in $TE_{21,13}$ mode) of microwave generation vs. perpendicular velocity spread for two value of alpha – 1.1, 1.44 (design alpha = 1.44).

Summary: Hence, we have been able to prove by several different methods and techniques that the beam quality is poor. This causes the alpha to be limited to lower values and the velocity spread to increase, especially as one increases the total beam current (EGUN). This increased velocity spread can then be shown to decrease efficiency (single mode code) and create azimuthal mode competition [85], which further decreases efficiency. The efficiency reduction predicted by theory taking into account the low alpha (1.1) and perpendicular velocity spread (24%) is ~12% while the experimentally observed reduction in efficiency is 6.2%. This lower efficiency of 6.2% could be explained by other factor such as: mode competition, a higher velocity spread than estimated, and energy spread.

Chapter 6

Discussion and Conclusions

6.1 Introduction

The work reported in this thesis on electron beams could lead to several important conclusions as well as meaningful follow-on projects. In this chapter, we first discuss the conclusions and suggestions for ferroelectric cathode electron beams and then the thermionic electron beams used in coaxial gyrotrons.

6.2 Ferroelectric cathodes

Two different gun geometries using large ferroelectric cathodes have been tested successfully. The two results can be summarized as a planar cathode (IAP) producing a 1.2 kA, 150 ns beam for accelerator applications, and an annular cathode (MIT) producing a 10 A, 5 μs beam for microwave generation. These results successfully demonstrate the use of ferroelectric cathodes in high total operating current, as well as long pulse (multi microsecond) regimes.

Along with these results of scalability, one should note that previous results [22] have demonstrated a normalized emittance of 5 mm-mrad, and a beam brightness of

1.2×10^{11} A/m^{2}rad^2. Also, no evidence of aging of the cathode was observed after tens of thousands of shots [22,24,25]. The present results have now demonstrated that the cathode size can be scaled up and that this promising new class of cathodes warrants greater investigation.

The emission theory is based upon (i) initial energy of the emitted electrons and (ii) surface plasma on the ferroelectric surface. These effects provide a quantitative basis for further investigation of ferroelectric electron emission. The theoretical curves show good agreement with experimental data for average energies in the range of 1.42 - 2.25 keV (which is within the range of experimentally measured energies)[25,30,31], and surface plasma densities of ~ 10^{12} cm^{-3} [21]. One has to recognize that these estimates will vary during a pulse and across different ferroelectric materials because of dynamic domain switching and plasma evolution. Nevertheless, broadly speaking, the initial energy and the surface plasma effects are able to explain:

1. Exceeding the Child-Langmuir limit of current density.
2. Non-zero emission current at zero accelerating voltage, and an approximately linear V-I relationship (as compared to the distinct $V^{3/2}$ dependence of the traditional Child-Langmuir [41]).
3. Emittance and brightness comparable to thermionic cathodes, due to the directionality of the electrons born on the cathode surface.
4. Emitted charge, which can exceed bound surface charge, due to the surface plasma.
5. Shot-to-shot inconsistencies as well as evidence of conditioning of the cathode - both of, which would be typical for a plasma effect on the surface.
6. Experimentally observed energetic electrons with a distribution functions which is consistent with theoretical analysis [31], and plasma densities of order ~10^{12} cm^{-3}.

7. Delay characteristics being dependent on the risetime of the pulse across the ferroelectric and the radius of the emitter being used, due to the plasma effect.

The dependence of emitted current on delay (Fig.4) can be partly explained by the expansion of a plasma across the surface. The plasma is first created at small microplasma points [21] or 'triple' points [29] (where the vacuum, metal, and the dielectric meet) on the cathode surface. It can then propagate across the ferroelectric cathode surface with a finite velocity leading to an optimum point of time (and thus delay) when the plasma is well established across the surface (the plasma emitting area is maximal) and the maximum current can be extracted from the cathode surface. The exact manner in which this plasma would propagate is dependent on several geometrical factors such as the mechanical arrangement of the diode, the ratio of the size of the cathode to the anode-cathode gap distance, and whether the configuration being used is a solid or annular beam. If one assumes that the microplasma point is at the center of the cathode then spreads towards the edge, the lower bound of the plasma expansion velocity can be estimated as the radius divided by the optimum delay which is ~1 cm/μs. This is in agreement with the experimentally observed values of 1-4 cm/μs [57,58,86,87]. This optimum delay effect has also been observed in experiments by Sampayan *et al* [25], and Flechtner *et al* [87] where the plasma expansion velocity can be calculated to be ~2 cm/μs. Other observations such as shot-to-shot inconsistency, are also characteristic of a surface plasma spreading across a cathode. Thus, a useful follow-on project would be to make detailed spatial and temporal measurements in order to further verify this explanation.

The difference in current density from the two experiments is partly due to the lower anode-cathode voltage used in the annular beam experiment and is in spite of the lower gap distance for the annular experiment. The slower risetime of the pulse across the ferroelectric also decreases current density [27] in the MIT experiment. These two effects make the annular beam current density an order of magnitude lower than the planar beam one. Thus, one can assume that the lower risetime of a pulse across a ferroelectric leads to lower plasma density on the cathode surface and lower emitted current, which has been observed by Gundel *et al* [27].

Among the drawbacks regarding this cathode which need to be addressed before widespread application in practical settings is the shot-to-shot reproducibility of the emitted current, as well as lower capacitance of the ferroelectric material to reduce the requirements on the pulse generator (for the pulse across the ferroelectric). Also, optimization of the material composition of the ferroelectrics, and a better understanding of the exact emission process of ferroelectric electron emission need to be investigated. Further work also needs to be done to establish the exact material science and the phase dependence of the ferroelectric emission in diodes of different geometries. Investigation is required on the exact dependence of the initial energies and surface plasmas on:

(i) polarities and modes of ferroelectric pulse voltage, (ii) beam pulse lengths, (iii) phase of the ferroelectric operation (ferroelectric, anti-ferroelectric, paraelectric), (iv) effects of the piezoelectricity of the crystal, (v) gun geometrical considerations, (vi) lifetime of ferroelectric cathodes, and (vii) the basic limits of ferroelectric cathodes in pulsed experiments with high repetition rates.

6.3 Coaxial gyrotrons

There have been several successes with the coaxial gyrotron experiment too regarding the performance of the tube and the electron gun. A better understanding has also been obtained regarding the design, fabrication, and operation of coaxial gyrotrons. Some of the accomplishments of the coaxial gyrotron experiments are:

1. The operation of the electron gun up to ~ 10 MW (105 kV, 93 A), which is the highest ever achieved in gyrotron tubes of this class
2. Operation of two large cathodes. This includes the installation, heating, and activation of the cathodes as well as arc-free operation of the gun to the full parameters of 95 kV, 76 Amps
3. Operation of the tube with the coaxial conductor and generation of ~ 1 MW RF power output
4. Good understanding of the modes, frequency, alpha, and power characteristics of the tube both with and without (empty cavity mode) the coaxial conductor
5. Generation of over 1 MW in the empty cavity mode of operation
6. Successful operation and the experimental measurement of the alpha with the alpha probe
7. Good agreement between the theoretically and experimentally measured velocity ratio's (alpha) for the tube (the theoretical value were obtained from EGUN simulations)
8. Operation of the tube in three different configurations – the first was in the radial output mode with a mode converter and single mirror, the second was with an axial output, and the third was with the coaxial conductor removed and axial output

9. General understanding of the difficulties involved in the alignment and the operation of coaxial gyrotrons
10. Better understanding of the limitations of cathodes with large emitter strips

Hence, one can see that there were several successful aspects of the coaxial gyrotron experiment although it failed to achieve the 3 MW output power that it was designed for. One may argue that we might have been able to get the 3 MW that this experiment was designed for if we had a well performing, azimuthally symmetric electron beam from the cathode. The shortcomings have been documented in several different ways for this cathode. The analysis shown in section 5.5.1 indicates that the poor quality electron beam is a major factor in low efficiency and low power output from the tube. Nevertheless, a deep understanding has been gained regarding the major issues that need to be addressed before the design and construction of a coaxial gyrotron.

One of the most important lessons that one learned from the experiments was the difficulty in making an azimuthally symmetric beam from a large cathode of diameter as large as 10 cm. In retrospect, one can imagine having a smaller cathode whose azimuthal symmetry can be better controlled. This would also reduce the beam compression, which would be an added benefit. Another lesson learnt was the difficulty of trying to align the three independent parts of the coaxial gyrotron – the electron beam, the cavity, and the coax conductor to within 0.25 mm. A good lesson to learn from this experiment is that all these tubes should be checked for electron beam symmetry and performance before spending significant time trying to optimize the power and the modes. Another lesson has been to think through all the alignment knobs required and not to build too many controls for the alignment, which actually sometimes adds to the complexity of the tube.

Hence a rigid connection of the coaxial conductor to the gun-anode with one set of controls on the gun side is probably the preferred arrangement. The cavity can first be aligned with the magnetic field and then the coax+gun-anode can be aligned to the cavity.

Some of the short term follow on projects based on the experiments described in this thesis for the near future can be:

1. Replacement of the existing cathode with a new cathode, testing of the cathode to verify better cathode performance, and operating the tube again in order to obtain higher power
2. Further improvement of the geometry of the tube in order to simplify the alignment process (may include fixing the coaxial conductor rigidly to the anode in the gun)

The longer term suggestions for these experiments are:

1. Using a smaller cathode with better azimuthal symmetry. This would improve the performance of the cathode and make its manufacturing easier and cheaper.
2. Perhaps the use of a vertical arrangement of the tube with the coaxial conductor rigidly attached to the gun anode. All alignment then would be made from the from gun end alone, making it an easier process.
3. Careful comparison of the merits and demerits of a coaxial gyrotron to the new multi megawatt regular gyrotrons (no coaxial conductor) being discussed.

6.4 Conclusions

In conclusion, several advances have been made by the research presented in this thesis. We have made significant contributions in the experimental parameters and theoretical understanding of ferroelectrics, as well as built and operated a coaxial gyrotron and understood the challenges that lie ahead in their further advancement. Some of the contributions and major successes are:

1. Tested the coaxial gyrotron in high power operation
2. Tested the Inverted Magnetron Injection Gun (IMIG) up to full power, 10 MW
3. Tested the coaxial gyrotron in three different configurations – empty cavity, axial output, and the radial output
4. Obtained over 1 MW of output power in two different modes of operation: with the coaxial conductor and in the empty cavity configuration
5. Observed regimes of dominant single mode and multi-mode operation
6. Identified cathode emission asymmetries and alignment of the tube as major factors in designing coaxial gyrotrons
7. Identified unexpected B field errors due to the magnetization of the stainless steel parts, which should be investigated for other gyrotron tubes
8. Suggested techniques for improving future coaxial gyrotrons including specifications on beam symmetry, alignment, and magnetization of parts
9. Built and tested the first ferroelectric cathode based Magnetron Injection Gun (MIG)
10. Demonstrated the first microwaves generated from a ferroelectric based microwave device in a collaboration experiment at Tel Aviv University
11. Developed a theory to explain the emission process from ferroelectric cathodes

Bibliography

1 K. Felch, M.Blank, P. Borchard, T.S. Chu, and J. Feinstein, Long Pulse and CW tests of a 110 GHz Gyrotron with an internal, quasi-optical converter, *IEEE Trans. Plasma Sci.*, 24(3):558, 1996.

2. Sato M., T. Shimozuma, Y. Takita, S. Kubo, H. Idei, Ohkubo K., T. Kuroda, T. Watari, M. Loring, Chu S., K. Felch, and H. Huey, *Proceedings of the 20th Int. Conf. Infrared and Millimeter Waves*, pp. 195, 1995.

3. G.G. Denisov, A.N. Kuftin, V.I. Malygin, N.P. Venediktov, and V.E. Zapevalov, *Int. Journal Electronics*, 72(1079):1091, 1992.

4. S. Alberti, O. Braz, P. Garin, Giguet E., M. Pain, P. Thouvenin, M. Thumm, C.Tran, and M.Q. Tran, *Proceedings of the 21st Int. Conf. Infrared and Millimeter Waves*, pp. AF1, 1996.

5. G. Dammertz, O. Braz, C.T. Iatrou, M. Kuntze, A. Mobius, B. Piosczyk, and M. Thumm, Long Pulse operation of a 0.5 MW $TE_{10,4}$ gyrotron at 140 GHz, *IEEE Trans. Plasma Sci.*, 24(3):570, 1996.

6. K. Felch, B. Danly, H. Jory, K. Kreischer, W. Lawson, B. Levush, R. Temkin, Characteristics and Applications of Fast-Wave Gyrodevices, *Proceedings of the IEEE*, Vol. 87, No.5, 1999.

7. Thumm M., Advanced electron cyclotron heating systems for the next step fusion experiments, *Proc. 12th Topical Conf. On Radio Frequency Power in Plasmas*, Savannah, Georgia, AIP Conf. Proceedings 403, pp. 183-190.

8. Thumm M., *Personal communications*, 1999.

9. Bogdanov S.D., Gyrotron Team, Solujanava E.A., Industrial gyrotrons from GYCOM, *Conf. Digest 19th Int. conf, on Infrared and Millimeter Waves*, Sendai, JSAP catalog No.: AP 941228, pp. 351-352, 1994.

10. Goldenberg A.L., Litvak A.G., Recent progress of high-power millimeter wavelength gyrodevices, *Phys. Plasmas*, 2, pp. 2562-2572, 1995.

11. M.E. Read, G.S. Nusinovich, O. Dumbrajs, G. Bird, J.P. Hogge, M. Blank, K. Kreischer, Design of a 3 MW, 140 GHz gyrotron with a coaxial cavity, *IEEE Trans. Plasma Sci.*, Vol 24, no.3, pp. 586-595, 1996.

12. C.T. Iatrou, S. Kern, and A.B. Pavelyev, Coaxial cavities with corrugated inner conductor for gyrotrons, *IEEE Trans. Microwave Theory Tech.*, Vol. 41, pp. 56-64, 1996.

13. B. Piosczyk, O. Braz, G. Dammertz, C.T. Iatrou, S. Kern, M. Kuntze, A. Mobius, and M. Thumm, A 1.5 MW, 140 GHz, $TE_{28,16}$ Coaxial Cavity Gyrotron, *IEEE Trans. Plasma Sci.*, 25(3):460, 1997.

14. Susan Spira Hakkarainen, Submillimeter Wave Harmonic Gyrotron, PhD Thesis, MIT, 1989.

15. J. Lohr, Personal communication, 1999.

16. Verhoeven, A G A, Bongers, W A, Bratman, V L, Caplan, M, Denisov, G G, Geer, C A J van der, Manintveld, P, Poelman, A J, Pluygers, J, Shmelyov, M Yu, Smeets, P H M; Sterk, A B; Urbanus, W H, First microwave generation in the

FOM free-electron maser, *Plasma physics and controlled fusion*, Vol. 40, Number 8//Supp A, pp. A139, 1998.

17. W.B. Herrmannsfeldt, "EGUN-An electron optics and gun design program," SLAC-Report-331, October 1988.

18. M. Blank, K.E. Kreischer, R.J. Temkin, Study of rotating modes in high frequency whispering gallery mode gyrotrons, *IEEE Trans. Plasma Sci.*, Vol. 22, No. 5, pp. 883-888, 1994.

19. R. Advani, J.P. Hogge, K.E. Kreischer, R. Temkin, Operation of a 3 MW, 140 GHz gyrotron with a coaxial cavity, *39th annual meeting of the division of plasma physics of the American Physical Society*, Vol. 42, No. 10, pp. 2071, 1997.

20. R. Advani, M. Pedrozzi, K.E. Kreischer, R. Temkin, Operation of a 3 MW, 140 GHz gyrotron with a coaxial cavity, *Proceedings of the 23rd Int. Conf. Infrared and Millimeter Waves*, pp. 195, 1998.

21. D. Shur, G. Rosenman, Ya. E. Krasik, V.D. Kugel, Plasma assisted electron emission from $PaLaZrTiO^3$ ceramic cathodes, *J. Appl Phys.* **79** (7), 3669 (1996).

22. G. Kirkman, B. Jiang, and N. Rhinehart, High brightness electron beam produced by a ferroelectric cathode, *Appl. Phys. Lett.* **66**(10), 1196 (1995).

23. H. Riege, Electron emission from ferroelectrics - a Review, *Nucl. Instrum. Methods*, A **340** (1994) 80-89.

24. J.D. Ivers, L. Schachter, J.A. Nation, G.S. Kerslick, and R.N. Advani, Electron beam diodes using ferroelectric cathodes, *J. Appl. Phys.* **79**, 2667 (1993).

25. S. Sampayan, G. Caporaso, C.Holmes, E. Lauer, D. Prosnitz, D. Trimble, and G. Westenskow, Emission from ferroelectric cathodes, *Nucl. Instrum. Methods*, A **340**, 90 (1994).

26. H. Gundel, H. Riege, E. Wilson, J. Handerek, K. Zioutas, Copious electron emission from PLZT ceramics with a high Zirconium concentration, *Ferroelectrics* **100**, 1 (1989).

27. H. Gundel, Meineke, First simultaneous observation of electron emission from a switching current transient in PZT ferroelectric ceramic, *Ferroelectrics* **146**, 29 (1993).

28. S. P. Bugaev, F. Ya. Zagulov, B. M. Koval'chuk, G. A. Mesyats, *Izv. Vyssh. Ucheben. Zaved. SSSR*, Fiz. **1**, 145 (1968).

29. G.A. Mesyats, Electron emission from a ferroelectric ceramic, *Sov. Phys. - Tech. Phys. Lett.*, vol. **20**, 8 (1994).

30. R. Advani, J.P. Hogge, K.E. Kreischer, W. Mulligan, R. Temkin, G. Kirkman, B. Jiang, and N. Rhinehart, Kiloampere and Microsecond electron beams from ferroelectric cathodes, *IEEE Trans. Plasma Sci.*, Vol.26, No.4, PP. 1347, 1998.

31. D. Shur, G. Rosenman, Ya E. Krasik, and R, Advani, A high-perveance ferroelectric cathode with a narrowed electron energy spectrum, *Journal Physics D: Applied Physics* 31, pp. 1375, 1998.

32. Spectra-Mat Inc., Data sheet, 1240 Highway 1, Watsonville, California 95076.

33. Takuji Kimura, Experimental study of a 1 MW, 170 GHz gyrotron oscillator, PhD Thesis, MIT, 1997.

34. Terry L Grimm, Experimental study of a 200-300 GHz megawatt gyrotron oscillator, PhD Thesis, MIT, 1992.

35. J.M. Baird, W. Lawson, Magnetron injection gun design for gyrotron applications, *Int. J. Electronics*, 61:953-967, 1986.

36. J.L. Cronin, Mordern dispenser cathodes, *IEEE proceedings*, pp. 19-32, 1981.

37. A.S. Gilmour Jr., *Microwave tubes*, chapter. 15, Artech House, 1986.

38. Sh. E. Tsimring, Limiting current of helical electron beams in gyrotrons, Int. J. of Infrared and Millimeter Waves, 14(4):817-840, 1993.

39. S.Y. Cai, T.M. Antonsen, G. Saraph, and B. Levush, Multifrequency theory of high power gyrotron oscillators, *Int. J. of Electronics*, 72(5-6):759-777, 1992.

40. T.M. Tran, G. Jost, K. Appert, S. Alberti, and M. Pedrozzi, Particle-in-cell simulations of beam instabilities in gyrotrons, *Physics of Plasmas*, Vol.4, No.8, pp. 3043, 1997.

41. R. Drori, M. Einat, D. Shur, E. Jerby, G. Rosenman, R. Advani, R. Temkin, C. Pralong, Demonstration of microwave generation by a ferroelectric cathode tube, *Applied Phys. Lett.*, Vol. 74, No.3, pp. 335, 1999.

42. L. Schachter, J.D. Ivers, J.A. Nation, G.S. Kerslick, Analysis of a diode with a ferroelectric cathode, *J. Appl. Phys.* **73**, 8097 (1993).

43. G. Benedek, I. Boscolo, J. Handerek, H. Riege, Electron emission from ferroelectric cathodes excited by short high-voltage pulses, *J. Appl. Phys.* **81** (3), 1396 (1997).

44. C. B. Fleddermann, J.A. Nation, Ferroelectric Sources and Their Application to Pulsed Power: A Review, *IEEE Trans. on Plasma Science*, 25 (2), 212 (1997).

45. G. Rosenman, E. V. Okhapkin, Yu. Chepelev, and V.Shur, Exoemission of Pyroelectrics, *Sov. Phys. - JETP Letts.*, **39**, 397 (1984).

46. G. Rosenman, D. Shur, Kh. Garb, R. Cohen, Ya. E. Krasik, Polarization switching in ferroelectric cathode, *J. Appl. Phys.* **82** (2), 772 (1997).

47. Transducer Products, Data Sheet, 211 North St., Goshen, Connecticut - 06756.

48. Langmuir, Child, Discharge from Hot CaO, *Physics Review*, 32, 492 (1911).

49. American Piezo Ceramics, Data Sheet, P.O.Box-180, Mackeyville, PA-17750.

50. I. Langmuir, Phys. Rev. **21**, pp.419-435, (1939).

51. Shengyi. Liu, PhD Thesis, Univ. of South Carolina, (1995).

52. G. Rosenman, Ferroelectrics **126**, 305 (1992).

53. H. Riege, Applied Surface Physics, Vol. 111, pp. 318, (1997)

54. J. Wang, W. Dawson, M. Chinkhota, T. Chen, Nucl. Instrum. and Methods A 387, pp 315, (1997).

55. H. Gundel, Thesis, Univ. Nurnberg (Shaker Verlag, Aachen, 1996).

56. W. Warren, D. Dimos, R. Waser, MRS Bulletin, pp. 40, July (1996).

57. D. Shur, G. Rosenman, Ya. E. Krasik, Surface discharge plasma induced by spontaneous polorization switching, *Appl. Phys. Lett.* **70**, 574 (1997).

58. G. Westenskow et. al., Double pulse experiment with a velvet cathode on the ATA Injector, *Proc. IEEE Part. Accl. Conf.,* May 1-5, 1995.

59. R. Anderson, J. Brainard, *Jour. Appl. Phys.*, **51**(3), pp.1414, March (1980).

60. E.Garate, R.McWilliams, D.Voss, A.Lovesee, K.Hendricks, T.Spencer, M.Collins Clark, A.Fisher, *Rev. Sci. Instrum.,* **Vol.66**, 3, (1995).

61. H. Miller, *IEEE Trans. on Elect. Insul.,* Vol.24, No.5, pp. 765, (1989).

62. D. Shannon, P. Smith, P. Dobson, M. Shaw, *Appl. Phys. Lett.,* **70** (12), 1625, (1997).

63. K.E. Kreischer and R.J. Temkin, A 120-240 GHz Step Tunable Megawatt Gyrotron, *IEEE 12th International Conference Digest*, pp. 192-193, December 1987.

64. M.E. Read, G.S. Nusinovich, O. Dumbrajs, K. Kreischer, B. Levush and G. Bird, Design of a 3 Megawatt, 140 GHz Gyrotron with a Coaxial Cavity, *Conf. Digest, 17th Int. Conf. on IR and mm Waves*, pp. 192-193 (1992).

65. A.V. Gapanov and M.I. Petelin, High Power High Frequency Classical Electronics: Status, Trends and Problems, *International Workshop on Strong Microwaves in Plasmas*, Suzdal, USSR (1990).

66. K.E. Kreischer, B.G. Danly, J.B. Schutkeker and R.J. Temkin, Design of Megawatt Gyrotrons, IEEE Trans. on Plasma Science, PS-13 (6) p. 364 (1985).

67. S.N. Vlasov, L.I. Zagryadskaya, I.M. Orlova, *Radio Eng. And Electron Phys.*, Vol. 21, No. 7, pp. 96-102, 1976.

68. V.A. Flyagin, N.S. Nusinovich, Gyrotron oscillators, *Proc. of the IEEE*, Vol. 76, pp. 646, (1988).

69. A.W. Fliflet and M.E. Read, *Int. Journal Electronics*, 51, p. 475 (1981).

70. G.S. Nusinovich, M.E. Read, O. Dumbrajs, K.E. Kreischer, Theory of gyrotrons with coaxial resonators, *IEEE Trans. of Plasma Sci.*, Vol. 41, No.3, pp. 433-438, (1994).

71. O. Dumbrajs and G.S. Nusinovich, *IEEE Trans. on Plasma Science*, **PS-20** pp. 454-457 (1992).

72. R.T. Longo, A study of thermionic emitters in the regime of practical operation, Technical Digest, *1980 Int. Electron Devices Meeting*, pp. 467-470, 1980.

73. J.M. Baird and W. Lawson, Magnetron Injection Gun (MIG) Design for Gyrotron Applications, *Int. J. Electron.*, **61**(6), p. 953-968 (1986).

74. J. Billen, L. Young, Poisson Superfish, Los Alamos National Laboratory.

75. Takuji Kimura, *Experimental Study of a 1 MW, 170 GHz Gyrotron Oscillator*, PhD Thesis, MIT, 1997.

76. A. Staprans, Electron Gun Breakdown, *High Voltage Workshop*, Monterey, CA, February 26, 1985.

77. G.G. Denisov, 110 GHz gyrotron with built-in high-efficiency converter, *Int. J. Electronics*, Vol. **72,** nos. 5 and 6, pp. 1079-1091, May and June 1992.

78. A. Mobius and J. Pretterebner, Conditions to achieve stable propagation of a Gaussian-like mode mixture in a deformed waveguide, *17th International Conference on Infrared and Millimeter Waves*, Conference Digest, pp. 34-35, December 1992.

79. M. Blank, K.E. Kreischer, R.J. Temkin, Quasi-optical mode converters for high order mode gyrotrons, *15th IEEE/NPSS Symposium on Fusion Engineering, Conference Digest*, October 1993.

80. J. A. Kong, *Electromagnetic Wave Theory*, John Wiley Sons, Inc., New York, pp. 376-385, 1986.

81. C.T. Iatrou, O. Braz, G. Dammertz, S. Kern, M. Kuntze, B. Piosczyk, and M. Thumm, Design and experimental operation of a 165 GHz, 1.5 MW, Coaxial Cavity Gyrotron with axial RF output, *IEEE Trans. Plasma Sci.*, 25(3):470, 1997.

82. M.Yu. Glyavin, A. N. Kuftin, N. P. Venediktov, A. S. Potnikova, M. V. Yulpatova, V. E. Zapevalov, Experimental investigations of emission inhomogeneity of gyrotron cathodes based on current-voltage characteristics, *Int. journal of Inf. and Mil. Waves*, vol.18, No.11, pp. 2137 (1997).

83. T. Idehara, K. Shibutani, H. Nojima, M. Pereyaslavets, K. Yoshida, I. Ogawa, T. Tatsukawa, Study of electron beam misalignment in a submillimter wave gyrotron, *Int. journal of Inf. and Mil. Waves*, vol.19, No.10, pp. 1303 (1998).

84. Kip Bishofberger, Analysis of Azimuthal asymmetries in an annular gyrotron electron beam, Thesis, Massachusetts Institute of Technology (1996).

85. Terry Grimm, Experimental study of a 200-300 GHz Megawatt Gyrotron Oscillator, Thesis, Massachusetts Institute of Technology (1992).

86. Mark Visosky, Thesis, Massachusetts Institute of Technology (1996).

87. D. Flechtner, C. Golkowski, G.S. Kerslick, J.A. Nation, Electron emission from lead-zirconate-titanate ceramics, *J. Appl. Phys.* **83 (2)**, 955 (1998).

88. O. Dumbrajs, J.P.T. Koponen, Generalized gyrotron theory with inclusion of electron velocity and energy spreads, *Physics of Plasmas*, Vol.6, No.6, pp. 2618, June 1999.

89. E. Borie, B. Jodicke, Self-consistent theory of mode competition for gyrotrons, *Int. J. Electronics*, Vol.72, No.5, 1992.

90. E. Borie, G. Gantenbein, B. Jodicke, G. Dammertz, O. Dumbrajs, T. Geist, G. Hochschild, M. Kuntze, H. U. Nickel, B. Piosczyk, M. Thumm, Mode competition in gyrotron cavities, *Int. J. Electronics*, Vol.72, No.5, 1992.